EFDA–JET–PR(12)57

F. Koechl, B. Pégourié, A. Matsuyama, H. Nehme, V. Waller, D. Frigione,
L. Garzotti, G. Kamelander, V. Parail and JET EFDA contributors

Modelling of Pellet Particle Ablation and Deposition: The Hydrogen Pellet Injection code HPI2

Modelling of Pellet Particle Ablation and Deposition: The Hydrogen Pellet Injection code HPI2

F. Koechl[1], B. Pégourié[2], A. Matsuyama[3,4], H. Nehme[2], V. Waller[2], D. Frigione[5], L. Garzotti[6], G. Kamelander[1], V. Parail[6] and JET EFDA contributors*

JET-EFDA, Culham Science Centre, OX14 3DB, Abingdon, UK

[1]Association EURATOM-ÖAW/ATI, Atominstitut, TU Wien, 1020 Vienna, Austria
[2]CEA/IRFM, 13108 Saint-Paul-lez-Durance, France
[3]National Institute for Fusion Science, Toki 509-5292, Japan
[4]Japan Atomic Energy Agency, Rokkasho-mura, Aomori 039-3212, Japan
[5]Association EURATOM-ENEA sulla Fusione, CP 65, Frascati, Rome, Italy
[6]EURATOM-CCFE Fusion Association, Culham Science Centre, OX14 3DB, Abingdon, OXON, UK
** See annex of F. Romanelli et al, "Overview of JET Results", (23rd IAEA Fusion Energy Conference, Daejon, Republic of Korea (2010)).*
** See annex of F. Romanelli et al, "Overview of JET Results", (24th IAEA Fusion Energy Conference, San Diego, USA (2012)).*

Preprint of Paper to be submitted for publication in
Nuclear Fusion

ABSTRACT.
The processes of pellet particle ablation and deposition considering the ∇B-induced E×B drift of the ionised ablated pellet particle cloudlets, i.e. the plasmoids, are reviewed and summarised in a first-principles based model for the determination of the pellet deposition profile. Motivated by clear experimental evidence for a significant ExB drift displacement of the pellet particles in tokamak plasmas as for instance at JET, particular emphasis is placed on the characterisation and model representation of physical phenomena that can influence the plasmoid drift and homogenisation dynamics, such as Alfvén wave propagation, external and internal short-circuit currents. Numerous related aspects that are currently under discussion are analytically and numerically examined, and the model equations are modified and complemented accordingly. The model has been implemented in a new simulation program called HPI2 for the calculation of hydrogen pellet material deposition in magnetically confined plasmas, e.g. in tokamaks, stellarators and reversed field pinch machines (RFPs). The program can consider various second-order effects like e.g. plasma pre-cooling, enhanced ExB drift damping in proximity of rational flux surfaces, or the rocket-like acceleration of the pellet due to inhomogeneous ablation. Results of a first validation are presented, and exemplary simulation cases for ITER-relevant plasmas are shown and interpreted. According to the model predictions, the ExB drift will play a crucial role in ITER to achieve a level of pellet particle penetration that is sufficient for fuelling purposes.

1. INTRODUCTION

Since pellet injection has become one of the most promising techniques for plasma fuelling, with many other applications, as e.g. for plasma control and diagnostic purposes, considerable efforts have been devoted in the past thirty years to comprehend the dissolution process of a small solid body drifting in a plasma. Due to the inherent intricacy of the problem, which is mainly caused by the many different involved physical mechanisms and scales, a whole science of pellet physics has been developed with an extensive literature reviewed in [1,2]. Among its primary objectives are the theoretical understanding of pellet ablation, and more recently that of the ∇B-induced E×B particle drift after ablation, which are particularly relevant to ITER for the prediction of the pellet fuelling efficiency.

An exhaustive description for the modelling of the process of hydrogenic pellet ablation and deposition with special emphasis on the E×B drift and drift damping mechanisms of the ablated and ionised pellet particle cloudlets, i.e. the plasmoids, is presented in this paper. Methods to calculate the pellet particle ablation rate based on a neutral gas and plasma shielding model including the influence of fast ions and electrons, and to estimate the rocket-like acceleration of the pellet in the case of inhomogeneous ablation are briefly summarised. Experimental results from the JET tokamak have been statistically analysed, highlighting the importance of the E×B drift on the particle deposition behaviour, and giving quantitative estimates for the drift displacement and the particle fuelling efficiency depending on the injection direction: As a rule of thumb, the pellet particle penetration

at JET can be expected to be reduced by ~15cm in terms of minor radius flux surface coordinates in the case of low field side (LFS) injections of fuelling pellets in L-mode plasmas, whereas it is slightly enhanced, if the plasma is fuelled by pellets from the inboard side. As an attempt to explain such observations by first principles, a plasmoid drift acceleration balance equation is set up, with the main drift driving term being derived from fundamental fluid continuity and plasma drift relations, considering additional drift-driving effects caused by the parallel plasmoid expansion as proposed in [3]. The Alfvén wave-induced drift damping effect is introduced on basis of a current wave equation in ideal magnetohydrodynamic (MHD) conditions, showing with the help of numeric simulations, that the influence of resistive effects on the propagation of parallel Alfvénic currents can be neglected, provided that stronger damping mechanisms take place in the later phase of the drift process. According to an assessment of the drift equation under simplified assumptions, the Alfvén wave dissipation mechanism is too weak to explain the strong drift deceleration observed in the experiment. It is very likely that the drift is further reduced by external and/or internal parallel short-circuit currents as suggested by B. Pégourié [4] and V.A. Rozhansky [5], whose models are reviewed in detail, putting special emphasis on the derivation of the external short-circuit current formation, and tackling related open questions. For example, the poloidal dependence of the strength of such external currents is examined, and a model is set up for the numerical approximation of inductive counter-currents. First simulation results for the characteristic inductive retardation time τ_L indicate that the plasma inductance was overestimated in first rough analytic approximations. From an elaborate description of the external short-circuit currents, it is concluded that the related drift damping can be underestimated in typical situations, if it is expressed in a simplified manner in order to obtain a drift equation that can be explicitly solved. Analytic expressions are formulated for the time τ_{con} when the short-circuit currents build up. Unipolar external electric potential reconnections and the momentum transfer to the affected plasma regions are accounted for. It is explained and illustrated by simulation results how the strength of the external short-circuit current induced drift damping effect is modified by rational magnetic flux surfaces, and how this relation can be exploited to give direct experimental evidence for the existence of the short-circuit currents and their possible importance as the main drift reducing actuator. An integrated plasmoid homogenisation model, in which the drift equation is closed giving a description of the dynamic evolution of the plasmoid in a four-fluids Lagrangian approach as developed in [4], and that now also treats the influence of fast ions during the homogenisation process, is further refined and reformulated as a set of 29 coupled ordinary differential equations.

The complete model for pellet ablation and deposition has been implemented in a simulation code called HPI2, in which the above-mentioned equation set is solved in order to determine the pellet particle deposition profile with the plasmoid drift calculated locally for a number of representative plasmoids taken into account. HPI2 can deal with arbitrary pellet injection configurations in realistic plasma equilibrium geometry, considering the pre-cooling of the plasma by pellet particles that have already been deposited. Various code validation efforts have been made. For a number of selected

pellet injection cases from different tokamaks and stellarators, good overall agreement with the experimentally measured drift displacement is reached, however, it should be noted that the error of the measurement is often considerable. The main parametric dependencies for the average plasmoid drift of a pellet particle have been determined. They mainly reflect the increase in the E×B drift for higher initial plasmoid pressures, which is related to the ablation rate and thus the background plasma pressure. Furthermore, it has been found out that the geometric dependencies of the considered drift damping effects and their reaction to a variation in the magnetic field strength are distinguishably conveyed by the drift scaling law, thus providing a simple means for determining their relative strength in the experiment. The influence of the pellet rocket acceleration effect, which is also implemented in HPI2, is assessed. Whereas it appears to be insignificant in high pressure plasma conditions, the pellet particle displacement due to the pellet rocket acceleration can become comparable to that attributed to the E×B drift in dedicated pellet fuelling experiments, which are often carried out in ohmic L-mode conditions to avoid measurement artefacts from MHD instabilities. HPI2 is also applied as stand-alone code to determine the influence of the E×B drift displacement on the pellet deposition profile in comparable stellarator, RFP, and tokamak configurations as well as for pellet-fuelled ITER plasmas. For the expected typical ITER fuel pellet injection and target plasma configurations, the pellets are predicted to be completely ablated close to the plasma edge. Only with the plasmoid drift, which is in the order of a few decimetres according to the simulation results and inwards directed in the case of high field side (HFS) injections as foreseen for ITER fuelling sized pellets, a significant fraction of the pellet mass can cross the edge pedestal and penetrate interior plasma regions. It is inferred that it seems impossible to fuel ITER from the outboard side, even if the injection velocity for LFS pellets can be considerably increased up to a few km/s with the help of new straight pellet injector technologies.

This paper is organised as follows. Pellet ablation and rocket acceleration are described in Section 2. Section 3 is dedicated to a statistical assessment of the plasmoid drift in JET discharges. An extensive derivation of the particle drift equation is given in Section 4, which is divided in subsections for each drift driving or damping term. The complete set of equations governing the plasmoid cloud dynamics is detailed in Section 5 and reformulated in a concise manner for numerical implementation in Section 6. Section 7 gives an overview of the HPI2 pellet code, showing exemplary simulation results, and including references to applications, extensions and improvements of the HPI2 code that have already been published elsewhere. Finally, predictions for pellet injections in ITER plasmas are presented in Section 8, and a summary is provided in Section 9.

2. PELLET ABLATION

Even though some particular questions remain to be answered more in detail, as e.g. concerning ablation anisotropy, the transversal expansion of ablated neutral particles, the local electrostatic shielding efficiency for incident particles, the accuracy of several steady-state assumptions in a highly transient pellet environment [1], and the importance of the magnetic field [6], it seems that the main

processes governing the particle ablation behaviour have already been identified. A satisfactory level of agreement is reached between ablation model predictions and measurement data for the pellet penetration length as shown in [7] for tokamaks and more recently [8] also for stellarators.

In this section, the main parameter dependencies for the determination of the ablation rate are derived. An enhanced model for the ablation of hydrogenic pellets based on [7,9,10], which has been integrated into the HPI2 pellet code, is summarised. Specific features in the numeric treatment of the ablation process in HPI2 are elucidated. Finally, the pellet rocket acceleration effect, which results from inhomogeneous pellet ablation and influences the initial deposition of ablated pellet material along the pellet trajectory path, is introduced.

2.1. THE NEUTRAL GAS SHIELDING (NGS) MODEL

The first ablation model for which reasonable accordance is obtained with experimental results is based on the concept of self-protection of the pellet by neutral gas shielding of the ablated particles [11]. Supposing a radius R_n of the neutral cloud that is proportional to the pellet radius r_p and dimensioned such that the energy of incident particles is almost completely absorbed by the neutral cloud, approximating the modified Bethe-Bloch formula for the collisional energy loss per distance dE ds of electrons passing through a non-ionised material [12] at initial energies E_∞ typical for ohmic plasmas as $dE/ds \propto n_n E^{-2\,3}$, with n_n for the density of the neutral cloud, and assuming quasisteady state conditions with zero local radial momentum on the pellet surface and equilibrated heat exchange between the neutral cloud and the plasma, the following relation is obtained for the pellet radius regression speed d_{rp}/dt, n_p being the atomic pellet density, T_n, T_∞ the temperatures in the neutral cloud and the background plasma, and s the electron path length inside the cloud:

$$
\begin{aligned}
& n_p \frac{dr_p}{dt} \sim n_n \sqrt{T_n}\,, \quad n_\infty \sqrt{E_\infty^3} \sim n_n \sqrt{T_n^3} \;\rightarrow\; \frac{dr_p}{dt} \sim \frac{1}{n_p} \sqrt[3]{n_n^2 n_\infty E_\infty^{3/2}} \\
& \frac{dE}{ds} \propto n_n E^{-2/3} \;\rightarrow\; E(s) \propto n_n^{3/5} s^{3/5} \;\rightarrow\; r_p \propto R_n \propto \frac{1}{n_n} E_\infty^{5/3}, \qquad (2.1) \\
& \frac{dr_p}{dt} \sim C \cdot \frac{1}{n_p} \sqrt[3]{\frac{n_\infty}{r_p^2} E_\infty^{29/6}} \sim C' \cdot r_p^{-2/3} n_\infty^{1/3} T_\infty^{5/3}.
\end{aligned}
$$

This scaling is the basic property of the NGS model. Even though it is an oversimplification of the real ablation process, its predictions have proven to be remarkably close to experimental results for the pellet penetration length [13,14], as more accurate descriptions of several phenomena accidentally compensate each other for pellet and plasma conditions of present day tokamaks. For extrapolations to pellet-fuelled ITER plasmas, and for the purpose of determining the distribution of pellet particle deposition, more advanced ablation models are required though, as the influence of fast particles on the ablation process is not considered in the NGS scaling, and since it does not consider the region of partly ionised ablated particles surrounding the pellet, whose properties are required to estimate the amount of particle drift due to the magnetic field gradient, as explained in Section 4. A more elaborated ablation model that is applied in HPI2 is presented below.

2.2. DESCRIPTION OF AN ENHANCED NEUTRAL GAS AND PLASMA SHIELDING MODEL

Most of the presently used pellet ablation models [15-20] are of the NGPS type (neutral gas and plasma shielding), considering an augmented protection of the pellet provided by an additional layer of ablated particles that become gradually ionised. Trapped by the magnetic field, their transversal mean free path is limited, and the ionised particle cloud, the so-called plasmoid, expands towards the parallel direction of the magnetic field, thus effectively increasing the shielding capability against incident electrons. Contrary to the NGS model, which considers a monoergetic electron beam, a Maxwellian energy distribution for thermal plasma electrons is usually assumed, leading to an acceleration in pellet ablation, as the energy absorption $\propto dE\ ds$ of the neutral and ionised clouds is much less effective for the energy tail of fast particles.

Following the ablation process from the exterior enfolding layers surrounding the pellet to the pellet surface, an enhanced NGPS model similar to that in [7] is described below. It incorporates the modification of the heat fluxes from the plasma due to the formation of an electrostatic double-layer sheath [16] and pre-sheath, which are particularly important in high pressure target plasmas. Their pellet shielding efficiency can even overweigh that of the plasmoid in these conditions [21], which is more transparent to particles with higher energy. The increase in ablation induced by fast ions, alpha particles, and electrons due to their high energy and geometric effects related to their finite Larmor radius is also considered. As to supra-thermal electrons, non-stationary processes caused by the direct volume heating of the pellet as described in [7,22] are taken into account. A detailed derivation of the enhanced NGPS model is given in [7,21,22]. Details on its implementation in the HPI2 code are specified in Subsection 2.3. and [21].

2.2.1. The electrostatic sheath.

As the mobility of the thermal plasma ions is considerably reduced compared to the electrons because of their higher inertia, their role in the ablation process is limited to an additional heat deposition in the outer region of the plasmoid, but also to the formation of an electrostatic sheath, which is structured such that the principles of quasi-neutrality and current continuity are preserved in the plasma and the plasmoid. It follows that a weak long-range pre-sheath potential Φ_{PS} builds up attracting the plasma ions towards the ablation cloud, and a stronger negative potential Φ_{DL} inside the plasmoid, with a sharp peak Φ_{SL} at the plasmoid-plasma interface. Only electrons with an energy exceeding the threshold $|q_e\Phi_{SL}|$ are then able to penetrate the plasmoid, the others are backscattered to the plasma. The level of Φ_{DL} is determined by the outflow of cold plasmoid electrons required to compensate for the imbalance between the ion and electron flows from the plasma; the higher Φ_{PS}-Φ_{DL}, the more plasmoid electrons are repelled towards the plasma. As the potential step Φ_{PS}-Φ_{SL} increases with the plasma temperature, the shielding capability of the electrostatic sheath is also important in the case of high energy thermal plasma heat fluxes. Expressions for the three potentials Φ_{PS}, Φ_{SL}, and Φ_{DL} have been derived in [23,24]. Due to the electrostatic sheath,

the electron heat flux into the plasmoid is attenuated, and the energy distribution of incident ions is modified. In practice, the following asymptotic approximations are always applicable in the case of pellet ablation: $|\Phi_{DL}|/|\Phi_{SL}| \approx T_{e0}/T_{e\infty} \rightarrow |\Phi_{DL}| << |\Phi_{SL}|$, $|\Phi_{SL}| = -1.8 q_e T_{e\infty}$.

2.2.2. The plasmoid.

The formation and evolution of the partly ionised cloudlet, in which the neutral cloud is immersed until it is released by the pellet and a new plasmoid builds up, can be modelled by a set of differential equations [25] for the mass M_0, the magnetic and internal energies E_{0mag} and E_{0int}, the speed of the transversal radius Rp and the elongation parallel to the magnetic field Z_0 of the plasmoid:

$$\begin{aligned}
\frac{dM_0}{dt} &= m_p \frac{dN_p}{dt}\Theta(t_{rel}-t),\\
\frac{dE_{0mag}}{dt} &= Q_{mag} - \pi R_p^2 Z_0\left(\frac{2}{R_p}\frac{dR_p}{dt} - \frac{1}{Z_0}\frac{dZ_0}{dt}\right)p_{0mag},\\
\frac{dE_{0int}}{dt} &= Q_{tot} - Q_i - \pi R_p^2 Z_0\left(\frac{2}{R_p}\frac{dR_p}{dt} + \frac{1}{Z_0}\frac{dZ_0}{dt}\right)p_0 + \frac{1}{2}\frac{dM_0}{dt}\left(\left(\frac{dR_p}{dt}\right)^2 + \left(\frac{dZ_0}{dt}\right)^2\right)\\
\frac{d^2R_p}{dt^2} &= \frac{1}{M_0}\left(2\pi R_p Z_0\left(p_0 + p_{0mag} - p_\infty - p_{\infty mag}\right) - \frac{dM_0}{dt}\frac{dR_p}{dt}\right),\\
\frac{d^2Z_0}{dt^2} &= \frac{1}{M_0}\left(\pi R_p^2\left(p_0 - p_\infty\right) - \frac{dM_0}{dt}\frac{dZ_0}{dt}\right)
\end{aligned} \tag{2.2}$$

Θ stands for the Heaviside function, t_{rel} for the time when the pellet and the plasmoid separate, m_p for the pellet atom mass, and dN_p/dt for the ablation rate. p_{0mag}, p_0 are the magnetic and kinetic pressure terms for the plasmoid, and $p_{\infty mag}$, p_∞ those for the plasma. Q_{mag} is the source of magnetic energy from magnetic diffusion, Q_{tot} reflects the energy transfer from the plasma to the plasmoid caused by incident particles (contributions from heat conduction are neglected), and Q_i the energy spent on particle ionisation. These energy source and sink terms are defined as follows:

$$\begin{aligned}
Q_{mag} &= \frac{2\pi R\ Z_0 \chi_{mag}\left(p_{\infty mag} - p_{0mag}\right)}{\sqrt{\pi\int \chi_{mag}\,dt}},\\
Q_{tot} &= R_0^2 \pi q_{0tot}\\
Q_i &= \frac{2\left(dM_0/dt \cdot f_i + M_0\, df_i/dt\right)\lambda_i}{2m_p},
\end{aligned} \tag{2.3}$$

with χ_{mag} representing the magnetic diffusivity, f_i the fraction of ionised particles (following Saha's equation), and λ_i the average dissociation and ionisation energy per atom, being in the order of 20eV. The total heat flux from incident particles q_{0tot} consists of contributions attributed to thermal electrons, thermal ions, and fast particles (related quantities are denoted by e, i, and f resp.):

$$q_{0e} = n_{\infty e} \exp\left(-\frac{q_e \Phi_{PS}}{T_{\infty e}}\right) \int_0^1 \sqrt{1-\tilde{\omega}^2} \left\{ \int_{q_e \Phi_{SL}}^{\infty} \tilde{\Pi}_e(\tilde{\omega}, E, B, R_0, 2Z_0) \cdot f_{\infty e}^{MB}(E, T_{\infty e}) \sqrt{\frac{2E}{m_e}} [E - q_e(\Phi_{SL} - \Phi_{DL}) - E_E(n_0, \tilde{\omega}, E, B, R_0, 2Z_0)] dE \right\} d\tilde{\omega}, \tag{2.4}$$

$$q_{0i} = \frac{2\int_0^1 \tilde{\omega} \int_0^{\infty} f_{\infty i}^{MB}(E, T_{\infty i}) \tilde{\Pi}_i(\tilde{\omega}\ E, B, R_0, 2Z_0) dE d\tilde{\omega}}{\int_0^{\infty} f_{\infty i}^{MB}(E, T_{\infty i}) dE} n_{\infty i} \beta \sqrt{\frac{T_{\infty i}}{2\pi m_i}} (2\mu T_{\infty i} + q_i(\Phi_{DL} \quad \Phi_{SL})), \tag{2.5}$$

$$q_{0f} = n_{\infty f} \int_0^1 \sqrt{1-\tilde{\omega}^2} \cdot \left\{ \int_0^{\infty} \tilde{\Pi}_f(\tilde{\omega}, E, B, R_0, 2Z_0) f_{\infty f}(E) \sqrt{\frac{2E}{m_f}} [E - E_E(n_0, \tilde{\omega}, E, B, R_0, 2Z_0)] dE \right\} d\tilde{\omega} \tag{2.6}$$

$f_{\infty e/i}^{MB}(T_{\infty e/i}, E)$ are Maxwell-Boltzmann distributions for the thermal particles, and $f_{\infty f}(E)$ arbitrary distributions for fast particles. β and γ are correction factors given in [26]. $\tilde{\omega}$ is defined by the particle pitch angle θ as $\tilde{\omega} = \sin\theta$. $\Pi_{e/i/f}$ is a geometric amplification factor, yielding by multiplication with the cross-section of the target (i.e. the plasmoid in this case) the effective particle collection area for incident particles characterised by $\tilde{\omega}$ and the kinetic energy E, for a magnetic field B, and for the cylinder radius R and length L of the target:

$$\tilde{\Pi}_{e/i/f}(\tilde{\omega}\ E\ B\ R\ L) = 2\int_0^{1+\tilde{\omega} x_{e/i/f}} \min\left(\frac{\alpha'}{\pi} + \frac{L}{2\pi x_{e/i/f} R\sqrt{1-\tilde{\omega}^2}}\ 1\right) z dz,$$
$$x_{e/i/f}(E, B, R) = \frac{\sqrt{2Em_{e/i/f}}}{q_i BR}, \quad \alpha'(\tilde{\omega}, x_{e/i/f}, z) = \cos^{-1}\left(\max\left(\frac{(\tilde{\omega} x_{e/i/f})^2 + z^2 - 1}{2\tilde{\omega} x_{e/i/f}\ z}, -1\right)\right) \Theta(z - x_{e/i/f}\ \tilde{\omega} + 1). \tag{2.7}$$

If an incident particle is able to leave the target, its remaining energy $E_E(n, \tilde{\omega}, E, B, R, L)$ can be determined from the following relation:

$$\frac{2nL}{(1+\tilde{\omega} x_{e/i/f})^2} \int_0^{1+\tilde{\omega} x_{e/i/f}} \frac{\alpha'}{\pi\sqrt{1-\tilde{\omega}^2}} z dz = \int_{E_E}^{E} \frac{dE'}{\sigma(E')}. \tag{2.8}$$

$\sigma(E)$ is the stopping cross-section. If all the energy of a particle is deposited inside the plasmoid, $E_E = 0$ in (2.4) and (2.6).

The ionised cloud can be supposed to become independent from the pellet either when it is stopped by the magnetic field and the pellet has drifted outwards, when it leaves the pellet due to an E×B drift caused by the gradient of the magnetic field and pressure inhomogeneity, or when it has reached a prescribed ionisation degree of typically 95 – 99% (since the decoupling of the plasmoid depends in any case on the strength of ionisation). The particles then freely homogenise in the plasma. This process is dominated by the E×B effect and detailed in Sections 3-5. The plasmoid parameters

at the time of release from the pellet are taken as input for the homogenisation model. Although the plasmoid density can surpass the background plasma density by a few orders of magnitude at that stage, the particle content of the plasmoid remains relatively small. For instance, the largest plasmoids predicted for the case of a large fuelling pellet injection into a JET L-mode plasma (Pulse No: 76411, see figure 23a) contain ~$2.5\times10_{19}$ D, i.e. ~3-4% of the pellet and plasma D content. The E×B drift experienced by the particles during ablation is calculated by a simplified drift equation and added to that during homogenisation. Its contribution is usually small and in the order of R_p. Since the development of the plasmoid is modelled as a continuous process, the time when it is considered to start being homogenised is not very influential to the drift behaviour.

Interestingly, the consideration of the plasmoid in the ablation model leads to a reduction of the ablation rate that is much weaker than expected. This behaviour can be explained by the spectral dependence of the incoming heat flux on the energy absorption rate. Having traversed the plasmoid, the energy distribution of incident electrons arriving at the neutral cloud is distorted, with a higher contribution of more energetic electrons. [16] Compared to a Maxwellian spectrum with the same temperature, the shielding of the neutral cloud is less effective for the same line-integrated pathaveraged neutral cloud density S_n, thus increasing the heat flux on the pellet surface $q_{p\,tot}$ and the pellet particle ablation rate dN_p/dt , whose definition is given below.

2.2.3. The neutral cloud.

Close to the pellet surface, the temperature is just in the order of a small fraction of an electron volt, and the ablated particles are still non-ionised and combined to molecules. This region is the most efficient shield against the plasma heat flux. It is also considered in NGS models. Depending on the heat flux qntot that reaches the neutral cloud, and the neutral cloud parameters R_N and n_n, the pellet radius regression speed and the ablation rate can be inferred from mass and energy conservation principles as [9,10]

$$\frac{dr_p}{dt} = -\frac{n_n^{2/3}}{n_p}\left(\frac{R_N}{r_p}\right)^2 \sqrt[3]{\frac{q_{ntot}}{m_p\left(1/\left(\gamma_n - 1\right) + /2\right)}}, \quad \frac{dN_p}{1\ dt} = 4\pi r_p^2 \left|\frac{dr_p}{dt}\right| n_{p.}. \tag{2.9}$$

γ_n is the ratio of specific heats at constant pressure and volume for the molecular gas in the neutral cloud. Whereas the ratio R_N/r_p is kept constant in HPI2 following the constraint that the NGPS model description must converge asymptotically with the NGS model when progressively switching to NGS model assumptions [10] (i.e. omitting shielding effects, applying monoergetic incident particles etc.), nn is adjusted such that the residual heat flux reaching the pellet surface, $q_{p\,tot}$, is used entirely for particle ablation:

$$q_{p\,tot} = -\frac{dr_p}{dt}\frac{\lambda_p n_p}{2}, \tag{2.10}$$

with the sublimation energy of a pellet molecule λ_p. $q_{n\,tot}$ can be expressed as the heat flux from

electrons and fast particles reaching the neutral cloud surface:

$$q_{n\,tot} = n_{\infty e} \exp\left(-\frac{q_e \Phi_{PS}}{T_{\infty e}}\right) \int_0^1 \sqrt{1-\tilde{\omega}^2} \left\{ \int_{q_e \Phi_{SL}}^{\infty} \tilde{\Pi}_e \left(\tilde{\omega}, E, B, \sqrt{4/3} \cdot r_p, r_p\right) \right.$$
$$\left. \cdot f_{\infty e}^{MB}(E, T_{\infty e}) \sqrt{\frac{2E}{m_e}} \left[E_E(n_0, \tilde{\omega}, E, B, R_0, Z_0) - q_e(\Phi_{SL} - \Phi_{DL})\right] dE \right\} d\tilde{\omega} \quad (2.11)$$
$$+ n_{\infty f} \int_0^1 \sqrt{1-\tilde{\omega}^2} \left\{ \int_0^{\infty} \tilde{\Pi}_f \left(\tilde{\omega}, E, B, \sqrt{4/3} \cdot r_p, r_p\right) f_{\infty f}(E) \sqrt{\frac{2E}{m_f}} E_E(n_0, \tilde{\omega}, E, B, R_0, Z_0) dE \right\} d\tilde{\omega}.$$

If S_n is added to the left-hand side of (2.8), formula (2.11) yields $q_{p\,tot}$.

If supra-thermal electrons are present, the pellet ablation process is non-stationary, i.e. drp dt is dependent on the time since the first interaction with the fast electrons, whose energy is neither fully absorbed in the plasmoid or neutral cloud, nor on the pellet surface, but mainly inside the pellet. The heat deposited in inner layers of the pellet ice enhances the ablation at a later time when these layers appear at the surface of the pellet. The non-stationary pellet ablation process can be treated by calculation of a function G for the energy density inside the pellet [7]:

$$G(\vec{r}, t) = \int_{t'=0}^{t} \nabla \cdot \vec{q}_p(\vec{r}) dt', \quad (2.12)$$

with $\vec{q}_p$ for the local heat flux flowing inside the pellet at a location $\vec{r}$, which can be determined from the heat fluxes arriving at the pellet surface and their attenuation inside the pellet ice considering an energy loss per unit path length $dE/ds = -n_p \sigma(E)/2$. In case of supra-thermal electrons, the stopping cross-section $\sigma(E)$ can be described by the Bethe-Heitler approximation for a hydrogenic environment. In principle, G needs to be calculated taking into account the heat flux from all thermal and non-thermal incident particles (mainly electrons). (2.10) can then be replaced by the expression

$$\frac{dr_p}{dt} = \frac{\partial}{\partial t} \sqrt[3]{\frac{3}{4\pi} \int \Theta\left(\lambda_p n_p - 2G(\vec{r}, t)\right) dV}, \quad (2.13)$$

since the energy density is always equal to the pellet molecule sublimation energy density at the interface between the pellet and the neutral cloud. As the thermal particles deposit all their energy in a very narrow layer close to the pellet surface, G diverges in the region $|\vec{r}| \approx r_p$ and becomes thus difficult to handle numerically. Practically, it has proven convenient to distinguish formally between thermal and supra-thermal incident electrons: The two pellet radius regression speeds for thermal and supra-thermal electrons, r_{pe}/dt, r_{pf}/dt can be calculated separately, r_{pe}/dt being determined by (2.10), whereas (2.13) is applied to obtain an estimate for the ablation enhancement caused by the deeply penetrating fast electrons, r_{pf}/dt. The total pellet radius regression speed can then be evaluated as $r_p/dt = \sqrt[3]{(r_{pe}/dt)^3 + (r_{pf}/dt)^3}$, the cubic average being the natural choice in accordance with the NGS scaling (2.1). r_p/dt is insensitive to the averaging method though due to a selfadaptation of r_{pe}/dt, r_{pf}/dt in case of a deviation from the natural average.

2.3. NUMERIC TREATMENT OF THE ABLATION MODEL IN HPI2 AND EXEMPLARY SIMULATION RESULTS

For the ablation model, it is required to obtain time-averaged plasmoid quantities for the calculation of the average plasmoid shielding capability against incoming particles, which is accounted for by addition of the line-integrated path-averaged density for the plasmoid, S_0, to that for the neutral cloud, S_n. Special care has been taken in the implementation of the enhanced NGPS model in HPI2 in order to assure best performance of the code in terms of reliability and precision. The numerically most delicate part of the ablation algorithm is the coupling between the plasmoid and the neutral cloud. In a first step, a rough guess for the ablation rate, dN_{pNGS}/dt, is made by application of the NGS scaling. The plasmoid evolution is then simulated by integration of the differential equation set (2.2), with dN_{pNGS}/dt inserted in the equation for the plasmoid mass, and followed until $t = t_{rel}$. Time averages for all plasmoid quantities are used to get average estimates for $q_{n\,tot}$ and $q_{p\,tot}$ according to (2.11), and a first guess for the ablation rate applying equations (2.9) can be obtained. The new value is then reinserted in the plasmoid mass equation, and the plasmoid and neutral cloud properties are recalculated iteratively until a stable solution for dNp/dt and $q_{n\,tot}$ has been found. The spectral distribution for the incident plasma particles is numerically treated by discretization into bunches of monoenergetic beams. Each beam is individually followed through all layers surrounding the pellet, where it progressively loses its energy until full absorption is reached. Because of the strong energy dependence of the stopping cross-section σ (E), the ablation rate is usually increased by up to ~400% without the effect of plasmoid protection and electrostatic sheath taken into account, if the incident particles are represented by a Maxwellian energy distribution instead of a monoenergetic beam (cf. figure 1). Still, the deviation between the NGPS and NGS model predictions for the ablation rate is much smaller, because particle shielding effects are not taken into account in the latter. It becomes more important for very high plasma pressure environments as they are expected e.g. in ITER, and at very low plasma energy levels like in the vicinity of the separatrix in mid-size tokamak discharges, which can affect penetration depth calculations for small pellets like those used for edge localised mode (ELM)-pacing purposes ($r_p < \sim$1mm or < ~5% of the particle content in the case of JET ILW H-mode plasmas; cf. the ablation profiles calculated with HPI2 using the NGS and NGPS models in figure 2).

2.4. THE PELLET ROCKET ACCELERATION EFFECT

As observed in the experiment (see e.g. [27]), it happens that the pellet trajectory is bent towards the outward horizontal direction. Due to inhomogeneous ablation on the pellet surface, the ablation rate being enhanced on the pellet side where the magnetic field is higher, which is caused by a slightly anisotropic shielding of the ablated particles engendered by the plasmoid drift effect as explained in Section 4, the pellet experiences an acceleration towards the negative direction of the magnetic field gradient. The kinetics is comparable to that of a rocket: The total momentum of the ablated particles is non-zero and compensated by an inversely directed drift of the pellet.

Purely theoretical and semi-empirical methodologies have been applied to analyse the rocket effect. In [28], a formula is proposed for the pellet acceleration ap , which reads in a simplified version for hydrogenic pellets and present day tokamak target plasmas, using scaling approximations for plasmoid pressure and geometry terms given in [22,29]:

$$a_p \approx 2.3\cdot 10^{-7}\sqrt[16]{m_p^9 R_0^8 r_p^{-22} n_\infty^{18} T_\infty^{23}}\cdot \exp\left(-3.4\cdot 10^{-6}\sqrt[12]{R_0^3 r_p^2 n_\infty^5 T_\infty^{-10}} - 9/4\right). \tag{2.14}$$

R_0 is the major radius of the tokamak. A heuristic model based on the NGS scaling is proposed in [30]:

$$a_p \approx 1.037\,\varepsilon\, m_p^{-1} n_p^{-1} r_p^{-4/3}\left(\frac{n_\infty}{10^{19}}\right)^{2/3} T_\infty^{1.54}\,. \tag{2.15}$$

The asymmetry parameter ε has to be derived from experimental data. According to pellet trajectory measurements at ASDEX Upgrade [30], $\varepsilon \sim 0.05$. As can be seen, the scalings for r_p and T_∞ in (2.14) and (2.15) are very similar, however, the n_∞ dependence is ~2/3 stronger in (2.14). Different predictions are also made for possible isotopic effects. Simulation results considering the pellet rocket acceleration effect are shown in Subsubsection 7.2.3..

3. STATISTICAL ASSESSMENT OF THE PLASMOID DRIFT

A statistical analysis of pellet experiments at the JET tokamak has been carried out to verify if the E×B drift displacement during plasmoid homogenisation can be observed systematically, to give a quantitative estimate for the typical displacement length depending on the injection direction, and to study the influence of other transport processes like diffusion on the measured pellet deposition profile. For this purpose, a database of pellet injection measurement data from JET experiments has been set up and analysed; furthermore, one well diagnosed shot featuring pellets from three different injection locations has been statistically processed and interpreted in detail [31]. It will be shown that there is clear evidence for a significant deviation between the positions of ablation and deposition of the pellet particles. As the E×B drift is always directed into the opposite direction of the gradient of the magnetic field strength, whose orientation is approximately the same in the whole poloidal plane for a typical magnetic field configuration in a tokamak, the existence of the plasmoid drift can also be verified indirectly by comparison of the pellet fuelling efficiency in dependence of the pellet injection angle. The experimental findings put forward in this section justify an in-depth study of the plasmoid evolution in the homogenisation phase as presented further below.

3.1. STATISTICAL ANALYSIS OF PELLET-FUELLED JET DISCHARGES

For the first time a set as wide as possible of pellet injection experiments at JET since 1999 has been studied systematically [31]. First, a pellet injection data consistency and reliability check was performed. The exact pellet entry times were derived and verified by the temperature drop measured

by electron cyclotron emission spectroscopy diagnostics for the plasma edge. The profiles for the pellet ablation (i.e. the pellet-induced density increase before the drift effect takes place) have been reconstructed from Ha spectrometry data. The deposition profiles (i.e. the distribution of the drifted pellet material) were obtained by Light Detection and Ranging (LIDAR) Thomson scattering density measurements. To distinguish between the rapid process of plasmoid drift displacement and other particle transport effects occurring on a longer time scale, the profile data have been divided according to the time delay between the moments of pellet injection and LIDAR measurement. The profile barycentres were then calculated and compared to quantify the drift displacement. The results for injections from the low and high B-field side (denoted as LFS resp. HFS, injection angles: $\alpha = 180^{\circ}$ resp. $\alpha = -40.6^{\circ}$) of the tokamak are shown in figure 1. For all undisturbed pellet events, a clear systematic outward displacement of the deposition profile has been measured. For LFS injections, it is in the order of ~15cm, whereas the average drift in HFS injections amounts to only ~5cm. This difference can be explained by the inclination of the pellet injection line with respect to the normal of the flux surfaces. In addition, the fact that pressure homogenisation and thus the reduction of the plasmoid drift driving force take place at a later time in low plasma pressure conditions close to the plasma boundary, which is reached by the plasmoid in case of LFS injection, can play a role. Furthermore, the pre-cooling of the target plasma by precedent plasmoids in the case of HFS injection can cause a poloidal asymmetry in the drift behaviour. If the plasma pressure in regions where subsequent plasmoids are deposited is reduced by the pre-cooling effect, the same is true for the plasmoid pressure and the driving force for the drift motion, as explained in the next section. Because of particle transport effects not related to the plasmoid displacement, the measured particle drift increases further with time for injections from the HFS, whereas it decreases for pellets from the LFS direction. Within ~100ms, the deposited pellet material is transported to regions with lower density in the plasma core, until it is completely mixed with the background plasma (Figure 3b).

3.2. DEPENDENCE OF THE PELLET INJECTION DIRECTION ON THE FUELLING PERFORMANCE

The fuelling efficiency in the JET Pulse No: 58337 was compared by quantification of the averaged density increase at the beginning of a pellet injection series, by estimate of the steady state density level, at which the particle loss equals the averaged pellet particle fuelling rate, and by calculation of the average relaxation time of the particle content. To this purpose, a high time resolution interferometer signal has been analysed. The results are displayed in table 1 and illustrated in figure 4. As can be seen, the fuelling efficiency is improved for HFS injections, being in accordance with the pellet particle drift behaviour observed in previous experiments [32,33]: If the pellet is inserted from the inner side of the tokamak, the particle drift is directed towards the plasma core, whereas it reduces the penetration in the case of outboard injections. The typical particle relaxation times are greater than 250 ms for inboard injections compared to pellets from the LFS.

4. DERIVATION OF THE PARTICLE DRIFT ACCELERATION

The dynamics of the detached plasmoid is mainly determined by pressure relaxation with the background plasma. It can be basically described by application of a four fluids Lagrangian drift model [34,4], considering simple mass and energy conservation laws (Sections 5,6). The difference in pressure is also the driving term for an E×B drift of the plasmoid particles, which can be directly observed in the experiment (Section 3), and which is therefore the most noticeable and traceable effect that results from the plasmoid homogenisation process; its determination is essential to obtain correct predictions of the pellet particle deposition. Therefore, from a practical point of view, the pellet drift dynamics is the crucial part in the physics describing the homogenisation of the ablated pellet material. In the homogenisation model presented in this paper, it is expressed via an equation for the average acceleration of a plasmoid particle. Once the acceleration function has been determined, the total average particle drift can be obtained by simple twofold integration.

Whereas the principle for the E×B drift acceleration has already been established many years ago, the physical description for the drift damping mechanism could be ascertained only recently by drift model validation against dedicated experiments in tokamaks [35] and stellarators [36]. Accordingto this description, the plasmoid-internal transversal currents that are caused by the curvature drift and that are responsible for the drift acceleration become short-circuited by the formation of Pfirsch-Schlüter like parallel currents. These currents can either flow inside or outside the plasmoid. In addition, the propagation of Alfvén waves may also be responsible for a slight attenuation of the drift in the early phase of plasmoid homogenisation. A combination of these drift damping mechanisms, which work on different time scales, is applied in the model presented below. After a derivation of the driving term, the damping mechanisms of charge cancellation via plasmoid-internal parallel currents (referred to herein as the "Rozhansky effect"), of Alfvén wave propagation, and of charge cancellation via plasmoid-external currents (called henceforth the "Pégourié effect") are described and evaluated.

4.1. THE DRIFT DRIVING TERMS

Departing from the fluid continuity equations for electrons and ions and Laplace's equation, making some reasonable approximations under the assumption of a cylindrical plasmoid shape with constant pressure inside and outside the plasmoid, the following simple expression is found,

$$-\frac{m_i n_i}{B_{\|}}\frac{\partial \vec{E}}{\partial t}\cdot \hat{e}_r = \frac{2\left(p_i + p_e - p_{i\infty} - p_{e\infty}\right)}{R}\sin\theta \,, \tag{4.1}$$

which is, written in other terms and neglecting $p_{i\infty}$, $p_{e\infty}$, the basic plasmoid particle drift acceleration equation including only the main drift acceleration term:

$$m_i \frac{du_D}{dt} = \frac{2k_B\left(T_i + T_e\right)}{R} \,, \tag{4.2}$$

with u_D for the drift velocity. A new exhaustive derivation of (4.1-2) is given in Appendix A.

In [3], the proposal was made to consider the change of the particle velocity distribution due to the longitudinal expansion of the plasmoid in the driving term of the drift equation. At the beginning of the plasmoid homogenisation, when the plasmoid temperature is still very low and dZ_0/dt approaches its maximum, one can expect a considerable enhancement of the E×B drift acceleration due to an increase in curvature drift. Given the local parallel plasmoid expansion speed $u^{\parallel}(z)$, the Maxwell-Boltzmann velocity distribution $f^{\parallel}_{MBi}$ for the parallel ion velocities $v_i^{\parallel}$ (the influence of electrons can be ignored due to their small inertia) is transformed to

$$f'^{\parallel}_{MBi}\left(v^{\parallel},z\right)=f^{\parallel}_{MBi}\left(v^{\parallel}-u^{\parallel}(z)\right)=\sqrt{\frac{m_i}{2\pi k_B T_i}}\exp\left(-\frac{m_i\ v^{\parallel}-u^{\parallel}(z)^2}{2k_B T_i}\right). \tag{4.3}$$

The average square of the particle velocity is then

$$\begin{aligned}\frac{1}{Z_0}\cdot\int_0^{Z_0}\int_{-\infty}^{\infty}\left(v^{\parallel}\right)^2\cdot f'^{\parallel}_{MBi}\left(v^{\parallel},z\right)dv^{\parallel}dz&=\frac{1}{Z_0}\cdot\int_0^{Z_0}\int_{-\infty}^{\infty}\left[\left(v^{\parallel}\right)^2+\left(u^{\parallel}(z)\right)^2\right]\cdot f^{\parallel}_{MBi}\left(v^{\parallel}\right)dv^{\parallel}dz\\&=\frac{1}{Z_0}\cdot\int_0^{Z_0}v_{Ti}^2+\left(u^{\parallel}(z)\right)^2dz=\frac{k_B T_i}{m_i}+\frac{1}{\xi}\left(\frac{dZ_0}{dt}\right)^2,\end{aligned} \tag{4.4}$$

with $\xi \sim 3$ for a linear expansion velocity distribution with respect to z. By analogy to the treatment of the ion temperature contribution to the curvature drift in the derivation of the drift driving term, the accelerative impact of dZ_0/dt on the E×B drift is translated in (4.15) as

$$m_i\frac{du_D}{dt}=\frac{1}{R}\left(2k_B\left(T_i+T_e\right)+\frac{m_i}{\xi}\left(\frac{dZ_0}{dt}\right)^2\right). \tag{4.5}$$

For reasons of conciseness, it is not taken into account in the following subsections, but reintroduced at a later stage.

4.2. DERIVATION OF THE ROZHANSKY EFFECT

Similar to the torsion of the magnetic flux around the magnetic axis of a tokamak, the magnetic field lines also rotate around the plasmoid centre. For instance, for a longitudinal distance $\Delta z = Z_0$, the poloidal angular rotation in a tokamak plasma is $\Delta\theta \sim Z_0/R_0 q$. Therefore, the charge accumulation on the plasmoid surface varies or even changes sign along a magnetic field line. It becomes equilibrated by a plasmoid-internal short-circuit current. For very long plasmoids or short magnetic reconnection lengths, charges of opposite sign at opposite locations start to cancel each other. A simplified model for the consideration of this effect in toroidally symmetric plasma geometries is given in Subsubsection 4.2.1, whereas a more general model that is used in HPI2 mainly for nonaxisymmetric magnetic configurations, is summarised in Subsubsection 4.2.2.

4.2.1. Simplified description for toroidally symmetric plasmas.

If $Z_0 > \pi R_0 q/2$, all magnetic field lines on the surface of a plasmoid inside a toroidally symmetric

plasma contain both positively and negatively charged sections of the same size and charge density. The electric field inside the plasmoid is zeroed and the driving term in the plasmoid drift equation vanishes [5,37] (cf. (4.1-2)):

$$-\frac{m_i n_i}{B_\parallel}\frac{\partial \vec{E}}{\partial t}\cdot \hat{e}_r = \frac{2\left(p_i + p_e - p_{i\infty} - p_{e\infty}\right)}{R}\sin\theta\,, \tag{4.6}$$

(4.6) is a rather imprecise description of the Rozhansky effect, as it also plays a role at smaller Z_0. A simple continuous weight function for the driving term can be obtained, if the relative rate of charge accumulation is expressed in cylindrical plasmoid coordinates as $\sin(\theta) = \sin(\theta_{z=0} + z/R_0 q)$. Taking the average value for the extremities of the plasmoid, and integrating for all magnetic field lines on the plasmoid surface, one has

$$m_i \frac{du_D}{dt} = \frac{2k_B\left(T_i + T_e\right)}{R}\,, \tag{4.7}$$

The weight function (4.7) normalised to 1 for Z0 = 0 gives the drift equation

$$f^{\prime\parallel}_{\mathrm{MBi}}\left(v^\parallel, z\right) = f^{\parallel}_{\mathrm{MBi}}\left(v^\parallel - u^\parallel(z)\right) = \sqrt{\frac{m_i}{2\pi k_B T_i}}\exp\left(-\frac{m_i\left(v^\parallel - u^\parallel(z)\right)^2}{2k_B T_i}\right). \tag{4.8}$$

f_{Rozh} as given in (4.7) should also just be considered as a rough guess for the Rozhansky effect. The magnitude of incertitude can be illustrated, if one calculates the weight function by integration of the average charge accumulation rate. This would lead to a complete suppression of the drift driving term at double elongation compared to (4.8). In the simulation results related to tokamaks presented in this paper, (4.8) is applied, being in conformance with [5,37]. A scheme for the exact implicit determination of f_{Rozh} is summarised in the next subsubsection.

Regardless of the precision in the calculation of f_{Rozh}, for typical plasmoid homogenisation conditions, the Rozhansky effect seems to play a minor role in tokamaks, since it becomes sizeable at a very late phase in the homogenisation process. As an example, for $T_i \sim T_e \sim 100\mathrm{eV}$, $R_0 \sim 3\mathrm{m}$, $q \sim 3$, and the longitudinal plasmoid expansion velocity being limited to the sound speed, it takes more than 150μs until (4.7) becomes zero. At this time, the homogenisation is usually finalised and the plasmoid particles have already reached their final position. In ITER-like situations, the characteristic time for the Rozhansky effect is even twice as much due to the size of the tokamak. As will be shown later on, the Pégourié effect dominates the drift damping process in a tokamak, whereas the Rozhansky effect becomes crucial in the calculation of the drift displacement in a nonaxisymmetric magnetic confinement with a small magnetic reconnection length, for instance in a stellarator. Still, the Rozhansky effect should be taken into account also in the first case, as it might be relevant in special situations (hot plasmas in a small tokamak, plasmoids with low density and large poloidal cross section). Numerically, it provides an upper limit in case of tokamaks when the solution of the differential equation set for the homogenisation process can be stopped.

Apart from the reduction of the drift acceleration, there is another possible consequence of the Rozhansky effect on the drift behaviour through its influence on the direction of the electric field. With the simplified description (4.8), the assumption is made that $E_\perp$ is always vertically aligned, as the curvature drift and the local charge separation take place in the vertical direction. The local drift displacement is then always taken to be horizontal as illustrated in figure 22 in Subsection 5.2. If the plasmoid-internal Rozhansky currents are efficient enough to cancel out all variations in the charge distribution along a magnetic field line, the direction of $E_\perp$ rotates though with increasing parallel distance to the plasmoid centre, following exactly the rotation of the magnetic field lines around the plasmoid (the direction of the electric field is then always vertical at the centre of the plasmoid and horizontal at its end positions with a distance $\pm\pi q R_0/2$ to the plasmoid centre in a tokamak plasma). In that case, the drift displacement is composed of a horizontal translation (the real drift) and a poloidal rotation, as visualised in figure 5. As a second order effect, one might observe a vertical asymmetry of the drift, a reduction thereof for vertical injections (which could partly compensate for the poloidal dependence of P_{con} mentioned in Subsubsection 4.3.5), and a modification thereof, if the magnetic field is inversed. Whereas the rotation of $E_\perp$ was found to play a major role in stellarators, it can be disregarded in tokamaks, as it only matters in the latter for plasmoids with a large extension in the parallel direction which typically appear at the end of the homogenisation process when the drift velocity is already very small. The change in direction of the electric field due to internal short-circuit currents is implicitly considered in the more general model of the Rozhansky effect that is described in the next subsubsection.

4.2.2. General description for arbitrary non-axisymmetric plasmas.

In [8,36], a general expression for the drift damping due to the Rozhansky effect has been derived that is also implemented in the HPI2 code. In contrast to the simplified expression given in the previous subsubsection, it can be used for arbitrary magnetic field configurations, provided that the toroidal component of the magnetic field gradient is negligible. Its usage is mandatory for simulations of the plasmoid drift displacement in magnetic configurations with a small magnetic reconnection length, e.g. in stellarators, where regions of opposite charge accumulation and a strong drift damping due to internal Rozhansky currents can already be reached at plasmoid locations with a distance of $\pm\pi R_0/m$ to the plasmoid centre, with m for the toroidal periodicity. For toroidally symmetric plasmas, the general description of the Rozhansky effect can be used to replace expression (4.8), although it was confirmed in a validation exercise that the latter is a convenient approximation for typical plasma and plasmoid properties in a tokamak. In the general expression, the drift damping due to the Rozhansky effect is implicitly included in the drift equation, i.e. it cannot be described by a factor fRozh for the drift acceleration term. In the following, only a brief description of this expression is given. A detailed derivation and discussion can be found in [8,36].

In the general case, the local ∇B and polarisation currents inside the plasmoid can be formulated as

$$\vec{j}_{\nabla B} = \frac{2(p_i + p_e - p_{i\infty} - p_{e\infty})\vec{B}\times\nabla|\vec{B}|}{|\vec{B}|^3}, \vec{j}_p = \frac{n_0 m_i}{|B|^2}\frac{d\vec{E}}{dt}. \tag{4.9}$$

Assuming ideal internal current short-circuit conditions, and applying Kirchhoff's law, a general drift vector equation can be obtained by averaging over all local current contributions inside the plasmoid along its parallel extension. Taking advantage of the fact that the rotation of $E_\perp$ is in line with the torsion of the magnetic field lines inside the plasmoid (cf. the previous subsubsection for a discussion of this behaviour), the radial and poloidal components of the drift can be treated independently. Presuming in addition that the toroidal components of the magnetic field gradient and thus of the drift as well are negligible, the general drift vector equation can be expressed in a simplified way via two decoupled scalar differential equations:

$$\begin{aligned}
\frac{du_D^{rad}}{dt} &= -\frac{2(p_i + p_e - p_{i\infty} - p_{e\infty})}{n_0 m_i \langle|\vec{B}|\rangle\langle 1/|\vec{B}|^2\rangle}\left\langle\frac{\nabla|\vec{B}|}{|\vec{B}|^2}\cdot\frac{\nabla\rho}{|\nabla\rho|}\right\rangle, \\
\frac{du_D^{pol}}{dt} &= -\frac{2(p_i + p_e - p_{i\infty} - p_{e\infty})}{n_0 m_i \langle|\vec{B}|\rangle\langle 1/|\vec{B}|^2\rangle}\left\langle\frac{\nabla\rho}{|\nabla\rho|^2}\times\frac{\nabla|\vec{B}|\times\nabla\rho}{|\vec{B}|^2}\right\rangle,
\end{aligned} \tag{4.10}$$

with $\langle ... \rangle$ for the average taken along the parallel extension of the plasmoid. For the consideration of a term $\propto\vec{u}_D$ representing the drift damping caused by Alfvénic and Pégourié currents that is derived in the next subsections, the general drift equations (4.10) just need to be modified in analogy with (4.8) (split into radial and poloidal components).

4.3. DERIVATION OF THE ALFVÉN WAVE-INDUCED DRIFT DAMPING EFFECT

Supposing conditions close to an ideal MHD regime, Alfvén wave pulses propagating from the ends of the plasmoid in the parallel direction to the magnetic field can lead to losses of the accumulated charges via parallel currents. As shown in Appendix B, the following wave equation is obtained, departing from Maxwell's equations and ideal MHD considerations and considering a source s(x,y,z,t) of electric charges in the plasmoid region that are accumulated by the curvature drift,

$$\Delta_\parallel \vec{j}_\parallel - \frac{1}{v_A^2}\frac{\partial^2 \vec{j}_\parallel}{\partial t^2} = \nabla_\parallel s, \tag{4.11}$$

which has the following solution for || jr (assuming (0) 0 || = = t j r),

$$\vec{j}_\parallel \sim \int_0^z s\,dz' - \frac{1}{2}\int_0^{z-v_A t} s\,dz' - \frac{1}{2}\int_0^{z+v_A t} s\,dz', \tag{4.12}$$

meaning that two wave fronts are propagating with Alfvén speed into both parallel directions, introducing a parallel current of the same strength as that observed at both ends of the plasmoid.

Repeating the calculation made in Appendix B under the assumption of resistive MHD behaviour ($E_{\|} = 1/\sigma \cdot j_{\|} \neq 0$), one finds

$$\begin{aligned} \nabla_{\|} \cdot \vec{j}_{\|} - s + \nabla_{\perp} \cdot \left(\varepsilon_0 \frac{c^2}{v_A^2} \frac{\partial E_{\perp}}{\partial t} \right) + \nabla_{\|} \cdot \left(\varepsilon_0 \frac{c^2}{v_A^2} \frac{\partial E_{\|}}{\partial t} \right) = 0, \\ \Delta_{\|} \cdot \vec{j}_{\|} - \varepsilon_0 \frac{c^2}{v_A^2} \Delta_{\perp} \nabla_{\|} \frac{\partial \Phi}{\partial t} + \varepsilon_0 \frac{c^2}{v_A^2} \Delta_{\|} \frac{\partial E_{\|}}{\partial t} = \nabla_{\|} s; \end{aligned} \tag{4.13}$$

$$\begin{aligned} E_{\|} = -\nabla_{\|} \Phi - \frac{\partial A_{\|}}{\partial t} = \frac{1}{\sigma} j_{\|}, \\ \mu_0 \vec{j}_{\|} = \int_0^t \Delta_{\perp} \nabla_{\|} \Phi \, dt' + \int_0^t \frac{1}{\sigma} \Delta_{\perp} \vec{j}_{\|} \, dt', \end{aligned} \tag{4.14}$$

giving an extended differential equation with an additional term owing to resistive current damping,

$$\begin{aligned} \Delta_{\|} \cdot \vec{j}_{\|} - \frac{1}{v_A^2} \frac{\partial^2 \vec{j}_{\|}}{\partial t^2} + \frac{1}{\sigma} \varepsilon_0 \frac{c^2}{v_A^2} \Delta_{\perp} \frac{\partial \vec{j}_{\|}}{\partial t} + \varepsilon_0 \frac{c^2}{v_A^2} \Delta_{\|} \frac{\partial E_{\|}}{\partial t} = \nabla_{\|} s, \\ \rightarrow \Delta_{\|} \cdot \vec{j}_{\|} - \frac{1}{v_A^2} \frac{\partial^2 \vec{j}_{\|}}{\partial t^2} + \frac{1}{\sigma} \varepsilon_0 \frac{c^2}{v_A^2} \Delta \frac{\partial \vec{j}_{\|}}{\partial t} = \nabla_{\|} s. \end{aligned} \tag{4.15}$$

Under the assumption that the gradient of the parallel current distribution in each dimension scalesroughly with the inverse of the extension of the (half-size) plasmoid in that dimension ($\perp: 1/R_{p,\|}: \infty 2/Z_0$), (4.15) can be transformed into an inhomogeneous two-dimensional secondorder partial differential equation with only the longitudinal spatial dimension taken into account. Knowing that $Z_0^2 >> R_p^2$ for typical plasmoids, and introducing the effective longitudinal resistivity $\eta_{eff} := Z_0^{2/} 2\sigma R_p^2$, one obtains

$$\frac{\partial^2 \vec{j}_{\|}}{\partial t^2} - \frac{\eta_{\text{eff}}}{\mu_0} \Delta_{\|} \frac{\partial \vec{j}_{\|}}{\partial t} - v_A^2 \Delta_{\|} \cdot \vec{j}_{\|} = -v_A^2 \nabla_{\|} s. \tag{4.16}$$

(4.16) can easily be solved numerically, interpreting it as a set of partial differential equations of the first order. Figure 6 shows the numeric solution for the time derivative of the parallel current for typical plasma conditions with a Gaussian charge source deposited at the center. The effective resistivity used for the left picture corresponds to the case when a plasmoid has just been released, with $Z_0 \sim 10 \times R_p$, whereas the picture on the right-hand side describes the situation when $Z_0 \sim 100 \times R_p$, which is typically the case after a time of a few microseconds (assuming that the plasmoid initially expands at sound speed in the longitudinal direction, and that the transversal expansion remains small). The dilatation of the Alfvénic current shockwave in the right picture comes from the second (ohmic) term in (4.16). It retards the time evolution of the parallel current caused by the curvature term. In the case with low effective resistivity, the ohmic perturbation is negligible. The size of the shockwave front remains equal to that of the source of electric charges. The solution for (4.16) is indistinguishable from (4.12), meaning that the assumption of ideal MHD conditions is accurate

for the initial time of the plasmoid evolution with low η_{eff}. Later on, the theory of Alfvén wave propagation still can be applied (between both shockwave fronts, the parallel current remains roughly constant as predicted by ideal MHD theory), but ohmic effects increase approximatively with the square of the parallel plasmoid extension. For non-negligible resistivity, $E_{||} \propto j_{||}$, with linearly decreasing electric potential. Models based on ohmic regimes become applicable and should progressively supersede ideal MHD-based assumptions.

To derive the Alfvén wave damping effect, one needs to know the amount of parallel current carried away from the plasmoid. Since this effect is dominant in the initial phase of the plasmoid homogenisation process only, one can keep ideal MHD assumptions and use (4.12) and (B.6) to determine the absolute value of $j_{||}$ between the plasmoid ends and the shockwave front:

$$\begin{aligned}
&\mu_0 j_\parallel = \Delta_\perp \nabla_\parallel \left(\int_0^t \Phi \, dt' \right) \sim \underbrace{\int_0^z s dz'}_{\sim \text{const. for } z>Z_0} + F(z - v_A t) + G(z + v_A t), \\
&\rightarrow \mu_0 j_\parallel (z > Z_0, t) = \mu_0 j_\parallel (z - v_A t) \sim \Delta_\perp \nabla_\parallel \left(\int_0^t \Phi (z - v_A t') dt' \right) \sim \nabla_\perp \nabla_\parallel \int_0^t \vec{E}_\perp (z - v_A t') dt \\
&j_\parallel (v_A t > z > Z_0, t) \sim -\nabla_\parallel \int_z^\xi \frac{\nabla_\perp \cdot \vec{E}_\perp (\xi')}{\mu_0 v_A} d\xi' = \nabla_\parallel \int_z^{z + v_A t} \frac{\nabla_\perp \cdot \vec{E}_\perp (z')}{\mu_0 v_A} dz' \\
&= \nabla_\perp \cdot \frac{\vec{E}_\perp (z,t) - \vec{E}_\perp (z, t=0)}{\mu_0 v_A} = \frac{\nabla_\perp \cdot \vec{E}_\perp}{\mu_0 v_A}.
\end{aligned} \tag{4.17}$$

The transversal diameters of the plasmoid in radial and poloidal direction were designated as La and L_b resp., with $R_p \sim \sqrt{{}_a L_b / \pi}$ (rectangular approximation). Repeating the procedure for the derivation of the basic plasmoid drift acceleration equation as detailed in Appendix A, but considering (4.17) in (A.8) for the consideration of the parallel current, and integrating also along the parallel direction until Z0 +e , one obtains

$$\begin{aligned}
&\left(\frac{Z_0 m_i}{B_\parallel^2} \left(\frac{\partial}{\partial t} + \vec{u}_i^\perp \cdot \nabla \right) \left(n_i \vec{E}(t,r) \right) - \frac{\vec{E}}{\mu_0 v_A} \right)_r \Bigg|_{r=R_p - \varepsilon}^{R_p + \varepsilon} = \frac{2 Z_0 (p_i + p_e - p_{i\infty} - p_{e\infty}) \sin\theta}{B_\parallel R}; \\
&- \frac{Z_0 m_i n_i}{B_\parallel} \frac{\partial \vec{E}}{\partial t} \cdot \hat{e}_r - \frac{2 B_\parallel \vec{E}}{\mu_0 v_A} \cdot \hat{e}_r = \frac{2 Z_0 (p_i + p_e - p_{i\infty} - p_{e\infty})}{R} \sin\theta, \\
&m_i n_i \frac{du_D}{dt} = \frac{2 (p_i + p_e - p_{i\infty} - p_{e\infty})}{R} - u_D \frac{2 B_\parallel^2}{\mu_0 v_A Z_0}.
\end{aligned} \tag{4.18}$$

The factor 2 in the new drift damping term describing the Alfvén wave current losses results from the radial component of the electric field outside the plasmoid, which is just opposite to that inside, given the solution (A.6):

$$\left(\vec{E} \right)_r \Big|_{r=R_p - \varepsilon}^{R_p + \varepsilon} = - \frac{\partial \Phi}{\partial r} \Bigg|_{r=R_p - \varepsilon}^{R_p + \varepsilon} = \frac{\partial}{\partial r} \left(C(t) r \sin\theta \right) \Big|^{R_p - \varepsilon} - \frac{\partial}{\partial r} \left(C(t) \frac{R_p^2}{r} \sin\theta \right) \Bigg|^{R_p + \varepsilon} = 2 \left(\vec{E} \right)_r \Big|^{R_p - \varepsilon}. \tag{4.19}$$

According to (4.18), the Alfvén wave-induced drift damping effect leads to a deceleration that is proportional to the drift velocity. For constant plasmoid and plasma properties, the solution is analytical, with an initial acceleration prescribed by the pressure difference and a saturation level given by the ratio between the driving term and the Alfvén wave damping factor:

$$u_D(t) = u_D(0) \cdot e^{\frac{-2B_\parallel^2}{m_i n_i \mu_0 v_A Z_0} \cdot t} + \frac{\mu_0 v_A Z_0 \left(p_i + p_e - p_{i\infty} - p_{e\infty}\right)}{B_\parallel^2 R} \left(1 - e^{\frac{-2B_\parallel^2}{m_i n_i \mu_0 v_A Z_0} \cdot t}\right) \tag{4.20}$$

For typical values ($v_A \sim 10^7$ m/s, $B_{||} \sim 3$T, $n_i \sim 10^{22}$ m^{-3}, $T_i \sim T_e \sim 100$eV, $Z_0 \sim 1$m, ~ 3m), the initial acceleration can be estimated as $du_D\ (t = \infty)/dt \sim 6\times10^9$ m/s^2; the saturation drift velocity is $u_D\ (t = \infty) \sim 1.5\times10^5$ m/s, the characteristic time for the asymptotic approach to the saturation level is $\tau_{Alfv} \sim 2\times10^{-5}$s. Obviously, the Alfvén wave damping is rather weak. It is not sufficient to predict a noticeable braking of the drift. The drift velocity can only be stabilised at a very high level, which even increases with time, because the temperature goes up during the homogenisation process, whereas the decrease in density is compensated by the proportionality of $u_D\ (t = \infty)$ to the longitudinal plasmoid extension.

Interestingly, the influence from Alfvén wave propagation on the plasmoid drift can also be derived from the magnetic tension arising when the magnetic field lines are supposed to be dragged by the movement of the plasmoid particles, as it is the case in ideal MHD regimes. For the sake of simplicity, u_D is taken to be constant. With $u_D \times t$ for the shift of the magnetic field at the position of the plasmoid centre, and a linear decrease to non-disturbed field lines at the position of the Alfvén wave fronts, i.e. $z = \pm vA \times t$, the magnetic field exerts a force of $B^2_{||}\ \pi\ R_0/\mu m$ Newton; projected to the direction of the plasmoid drift, one obtains

$$\begin{aligned} m_i n_i \pi R_0 Z_0 \frac{du_D}{dt} &= \frac{B_\parallel^2 \pi R_0}{\mu_0} \frac{u_D t}{\sqrt{\left(v_A^2 + u_D^2\right) t^2}}, \\ m_i n_i \frac{du_D}{dt} &\sim \frac{u_D}{v_A} \frac{B_\parallel^2}{\mu_0 Z_0}, \end{aligned} \tag{4.21}$$

which corresponds exactly to the Alfvén wave damping term in (4.18). It should be noted though that such a derivation might not be valid in a plasma whose magnetic field is mainly sustained by external currents.

4.4. DERIVATION OF THE PÉGOURIÉ EFFECT

As pointed out in [4], it may happen during the electric potential expansion process at Alfvénic speed along the magnetic field lines that regions of opposite polarisation of the plasmoid become connected with each other. This process leads to a depletion of accumulated charges via an external short-circuit current, decreasing the electric potential and the drift velocity. It occurs at a time greater than the time of first connection t con , which is in the order of 10 ms. The depletion current can therefore be taken to have ohmic character. In the following, the magnitude of this current and its equivalent in the plasmoid drift equation are formulated via an approximate and a more rigorous approach.

4.4.1. Simple description of the external current.

Depending on the parallel electric field, $E_{||}$, and the external plasma conductivity [38], $\sigma_{||\infty} = \sigma_{||}Sp = 1.96 q_e^2\, n\infty\, \tau_e\infty /m_e$ with $= 3.44\times10^{11}\, t_e^{1.5}/n\, \ln\Lambda$ for the electron collision time ($\ln\Lambda$ is the Coulomb logarithm, (5.1)), me for the electron mass and the index ∞ describing quantities of the background plasma, the total parallel external current related to the Pégourié effect reads

$$I_{\parallel} = \left(1 - e^{-(t-\tau_{con})/\tau_{e\infty}}\right)\sigma_{\parallel\infty} E_{\parallel} P_{con} L_b L_{J\phi}\,. \tag{4.22}$$

$L_{J\phi}$ represents the radial width of the external parallel current conduit, which augments with current diffusion. In [22], it is estimated as

$$L_{J\phi} = \min\left(\frac{L_b}{2}, 2\sqrt{\frac{4\pi}{\mu_0}\int_0^t \sigma_{\parallel\infty} dt'}\right). \tag{4.23}$$

P_{con} describes the fraction of magnetic field lines crossing positively charged plasmoid regions that are externally connected to zones with negative polarisation.

For symmetry reasons, $E_{||}$ can be expressed by the poloidal electric field inside the plasmoid:

$$E_{\parallel}\left(L_\phi - Z_0\right) = E_\perp L_b\,,\; L_\phi = \frac{4\pi^2 R_0 \rho}{L_b}, \tag{4.24}$$

with the average external plasmoid self-connection length L_ϕ and the major and local minor radii R_0, ρ. Assuming $P_{con}(t > \tau_{con}) \sim 1$, we find

$$I_{\parallel} = \Theta(t-\tau_{con})\left(1 - e^{-(t-\tau_{con})/\tau_{e\infty}}\right)\frac{\sigma_{\parallel\infty} E_\perp L_b^2 L_{J\phi}}{L_\phi - Z_0}. \tag{4.25}$$

As L_b varies slowly with time, L_ϕ as defined in (4.20) is almost constant in the time interval of interest, i.e. $L_\phi \times dL_\phi\,(dt > t)^{-1} > \tau_{con}$. Of course, P_{con} and the real average self-connection length are not constant. Yet, (4.20) is in good qualitative agreement with more accurate descriptions, because both quantities are roughly proportional in the initial phase of current formation, which is the most significant for the calculation of the drift velocity, and therefore their time-dependencies cancel in the fractional term.

Replacing the Alfvénic current term in (4.18) by (4.25), normalised by the poloidal cross-section of the charged region (whose effective radial elongation is 2ε), the plasmoid drift equation reads

$$\begin{aligned} -\frac{Z_0 m_i n_i}{B_{\parallel}}\frac{\partial E_\perp}{\partial t} - \Theta(t-\tau_{con})\left(1 - e^{-(t-\tau_{con})/\tau_{e\infty}}\right)\frac{\sigma_{\parallel\infty} B_{\parallel} L_b L_{J\phi} E_\perp}{L_\phi - Z_0} &= \frac{2Z_0\left(p_i + p_e - p_{i\infty} - p_{e\infty}\right)}{R}, \\ m_i n_i \frac{du_D}{dt} = \frac{2\left(p_i + p_e - p_{i\infty} - p_{e\infty}\right)}{R} - u_D \frac{\max\left(0, 1 - e^{-(t-\tau_{con})/\tau_{e\infty}}\right)\sigma_{\parallel\infty} B_{\parallel}^2 L_b L_{J\phi}}{Z_0\left(L_\phi - Z_0\right)}&. \end{aligned} \tag{4.26}$$

Omitting the retarding effect of τ_e, and τ_{con}, the analytic solution for constant plasmoid and plasma

properties is similar to (4.15). For typical values ($B_{\|} \sim 3T, \sim n_i \sim 10^{22}\ m^{-3}$, $n_{i\infty} \sim 3\times10^{19}\ m^{-3}$, $T_e \sim T_i \sim 100eV$, $T_{e\infty} \sim 1keV$, $\ln\Lambda \sim 17$, $L_b \sim 3\times10^{-2}$ m, $Z_0 \sim 1m$, $R \sim R_0 \sim 3m$, $a_0 \sim 1m$), the saturation drift velocity for (4.26) is $u_D\,(t = \infty) \sim 6\times10^3$m/s , i.e. 25 times less than $u_D\,(t = \infty)$ for (4.20). This demonstrates that the drift damping caused by the Pégourié effect is much stronger than that caused by Alfvén wave dissipation. One can also deduce from the analytic solution to (4.26) that it is essential to keep $p_{e\infty}$, $p_{i\infty}$ in the plasmoid drift equation to properly describe the late phase of the homogenisation process, as the drift displacement cannot be completely stopped by the Pégourié effect otherwise. Initially, like in (4.20), a decrease in plasmoid density caused by the longitudinal plasmoid expansion is compensated by an increase in Z_0 in the nominator of the term for the saturation drift velocity. Later on, when the difference in pressure becomes comparable to the pressure of the background plasma, its relative reduction is much stronger than the relative growth of Z_0. As a consequence, the driving term completely vanishes after a time $\Delta t \sim \ln(p/\Delta p)/\ln(1+ \dot{Z}_0/Z0$ and the plasmoid drift is stopped. It is easy to verify that for $p_{e\infty} \sim p_{i\infty} \rightarrow 0$, this final homogenisation phase can never be reached.

4.4.2. Analytical description of τ_{con}, P_{con}, and L_{con}.

Due to the discrete nature of flux tube reconnections, the derivation of an analytical function for the quick calculation of the time of first connection τ_{con} between regions of opposite charge, i.e. the characteristic time for the start of the Pégourié drift damping effect, is quite tedious. Following a step-by-step approach, for a virtual, uniformly charged plasmoid with $L_a = Z_0 = 0$ and a poloidal extension of $L_b = 2R_p^{pol}$, the plasmoid reconnection length L_{con} at a location r_0 in terms of minor radius flux surface coordinates with a rational safety factor $q(r_0) = m/n$, $m,n \in N$, and the corresponding time until the connection is established, are

$$L_{con} \approx 2\pi R_0 m, \quad \tau_{con} \approx \frac{\pi R_0 m}{v_A}. \tag{4.27}$$

As the polarisation propagates along field lines from both ends of the plasmoid, the net propagation speed is $2v_A$. Caused by the poloidal extension of the plasmoid, the same values for τ_{con} and L_{con} are obtained in an interval $I_0 = [(r_0 - \delta r_0), (r_0 + \delta r_0)]$, such that

$$\delta\theta = m\delta\left(\frac{2\pi}{q}\right) = \frac{2R_p^{pol}}{r_0}, \text{ i.e. } \pi r_0 m\left|\frac{\partial q}{\partial r}\right|_{r_0}\frac{\delta r_0}{q(r_0)^2} = R_p^{pol}, \text{ or } \delta r_0 = \frac{m}{n^2}\frac{R_p^{pol}}{\pi r_0\left|\frac{\partial q}{\partial r}\right|_{r_0}}, \tag{4.28}$$

Introducing a radial plasmoid extension $L_a = 2R_p^{rad}$, δr_0 is increased accordingly:

$$\delta r_0 = \frac{m}{n^2}\frac{R_p^{pol}}{\pi r_0\left|\frac{\partial q}{\partial r}\right|_{r_0}} + R_p^{rad}. \tag{4.29}$$

Considering as a next step a parallel elongation of $Z_0 \neq 0$, the width of the interval I_0 is unaffected,

as the plasmoid is distorted by the magnetic shear in such a way that all field lines leave the cloudlet at $\pm Z_0$. The only modification that one might consider is that resulting from the shortening of L_{con},

$$L_{con} \approx 2(\pi R_0 m - Z_0),\ \tau_{con} \approx \frac{\pi R_0 m - Z_0}{v_A}, \tag{4.30}$$

but the relative change between (4.27) and (4.30) is usually very small. Only at the very end of the homogenisation process, when Z_0 approaches $\pi R_{0q}/2$ (see Subsection 4.2 for an explanation) and L_ϕ is reduced by the effect of poloidal diffusion, it may be significant. As we are looking for τ_{con} whose ratio compared to the total homogenisation time is just $\sim C_s/v_A$ (C_s… sound speed), the Z_0 corrections in (4.25) can be ignored.

If one considers now a dipolar charge distribution with positive charges in a poloidal distance y from the plasmoid axis given as $\Delta^{pol} < y < \Delta^{pol} + 2R_p^{pol}$ and with negative charges situated at $-\Delta^{pol} > y > -\Delta^{pol} - 2R_p^{pol}$, one simply has to consider a double poloidal extension in the definition of δ_0 for $\Delta^{pol} = 0$:

$$\delta r_0 = \frac{m}{n^2} \frac{2R_p^{pol}}{\pi r_0 \left|\frac{\partial q}{\partial r}\right|_{r_0}} + R_p^{rad}. \tag{4.31}$$

For $\Delta^{pol} > 0$, and only allowing for reconnections of oppositely charged regions, one can define

$$\delta r_0^{tot} = \frac{m}{n^2} \frac{2R_p^{pol} + \Delta^{pol}}{\pi r_0 \left|\frac{\partial q}{\partial r}\right|_{r_0}} + R_p^{rad},\ \delta r_0^{\pm} = \frac{m}{n^2} \frac{R_p^{pol}}{\pi r_0 \left|\frac{\partial q}{\partial r}\right|_{r_0}} + R_p^{rad}. \tag{4.32}$$

The radial interval of interest around q = m/n , and inside which L_{con} and τ_{con} are constant, is then

$$I_0 = \underbrace{\left[\left(r_0 - \delta r_0^{tot}\right), \left(r_0 - \delta r_0^{tot} + 2\delta r_0^{\pm}\right)\right]}_{:=I^{\inf}} \cup \underbrace{\left[\left(r_0 + \delta r_0^{tot} - 2\delta r_0^{\pm}\right), \left(r_0 + \delta r_0^{tot}\right)\right]}_{:=I^{\sup}}. \tag{4.33}$$

For a plasmoid located at rc in minor radius flux surface coordinates, t con can now be obtained by application of the following procedure:

1. Selection of the range of toroidal $m-$numbers of interest $m_i \in \left[1, m^{\max}\right]$.
2. Calculation of the corresponding poloidal $n-$numbers: $n_i^{\inf} = \mathrm{Int}\left(\frac{m_i}{q(r_c)}\right)$, $n_i^{\sup} = n_i^{\inf} + 1$.
3. Calculation of the corresponding q values $q_i^{\inf} = \frac{m_i}{n_i^{\inf}}$, $q_i^{\sup} = \frac{m_i}{n_i^{\sup}}$, their locations $r_i^{\inf}$, $r_i^{\sup}$: $r_i^{\inf/\sup} \approx r_c - \frac{q(r_c) - q_i^{\inf/\sup}}{\left|\partial q/\partial r\right|_{r_c}}$ and the radial intervals $I_i^{\inf}$, $I_i^{\sup}$.
4. Selection of the value m_{con} to be considered by taking the minimum of all m_i values featuring a reconnection of opposite charges:
$$m_{con} = \min\left(m_i \in \left[1, m^{\max}\right] \middle| \left(I_i^{\inf} \cap r_c\right) \cup \left(I_i^{\sup} \cap r_c\right) \neq \{\}\right).$$
5. Estimation of L_{con} and τ_{con}: $L_{con} = 2\pi R_0 m_{con}$ and $\tau_{con} = \frac{\pi R_0 m_{con}}{v_A}$.

To avoid regions where L_{con} and τ_{con} are not defined, one must choose m^{max} such that the distance between r_{imax}^{inf} and r_{imax}^{sup} is smaller than $\sim 2R_p^{rad}$. In terms of $\mu = 1/q$, this distance is

$$\mu_i^{\inf} - \mu_i^{\sup} = \frac{1}{q_i^{\inf}} - \frac{1}{q_i^{\sup}} = \frac{n_i + 1}{m_i} - \frac{n_i}{m_i} = \frac{1}{m_i}. \tag{4.34}$$

The condition to be fulfilled can then be reformulated as

$$\left|\frac{d\mu}{dr}\right| 2R_p^{rad} > \frac{1}{m^{\max}} \rightarrow m_{\max} > \left(2\left|\frac{d\mu}{dr}\right| R_p^{rad}\right)^{-1}, \tag{4.35}$$

Using $|d\mu/dr| = |1/q^2 \times dq/dr|$, one obtains:

$$m^{\max} \sim \frac{q(r_c)^2}{2R_p^{rad}} \left|\frac{dq}{dr}\right|_{r_c}^{-1}. \tag{4.36}$$

Insertion of typical values, $q(r_c) \sim 2$, $dq/dr|_{r_c} \sim 4$ and $R_p^{rad} \sim 10^{-2}$ leads to $m^{max} \sim 50$.

With the bivalent function $f : r, r_0, r_1, r_2 \in |R|\ r_1 < r_2 \rightarrow \{0, 1\}$ define as

$$\begin{aligned} f(r, r_0, r_1, r_2) = {} & \Theta(r - r_0 + r_2) + \Theta(r_0 + 2r_1 - r_2 - r) + \Theta(r - r_0 + 2r_1 - r_2) + \Theta(r_0 + r_2 - r) - 2 \\ & + \Theta(2r_1 - r_2)(\Theta(r - r_0 - 2r_1 + r_2) + \Theta(r_0 - 2r_1 + r_2 - r) - 1) \end{aligned} \tag{4.37}$$

($\Theta(...)$ for the Heaviside function), an analytic expression for τ_{con} can be given:

$$\tau_{con} = \frac{\pi R_0}{v_A}\left[\max_{m_i \in [1, m_{\max}]}\left(\frac{1}{m_i}\int \max\left(f\left(r_i^{\sup}, \delta r_i^{\pm \sup}, \delta r_i^{tot\,\sup}\right), f\left(r_i^{\inf}, \delta r_i^{\pm \inf}, \delta r_i^{tot\,\inf}\right)\right)\delta(r - r_c)dr\right)\right]^{-1} \tag{4.38}$$

A simplified explicit analytical expression, which is continuous and differentiable in r, can also be formulated:

$$\begin{gathered} \Theta'(x) = \frac{1}{1 + \exp(-4x/\Delta_{\text{res}})},\ \Delta_{\text{res}} \rightarrow 0, \\ \Gamma_i = \Theta'\left(\cos\left(i \cdot \frac{2\pi}{q(r_c)}\right) - \cos\left(i \cdot 2\pi\left(\frac{2R_p^{pol} + \Delta}{i \cdot \pi r_c} + \frac{R_p^{rad}}{q(r_c)^2} \cdot \left|\frac{dq}{dr}\right|_{r_c}\right)\right)\right), \\ \tau_{con}(r_c, R_p^{pol}, R_p^{rad}, \Delta, v_A, R_0) = \frac{\pi R_0}{v_A} \cdot \sum_{m=1}^{m^{\max}} \Theta'\left(1 - m - \ln\left(\sum_{i=1}^{m^{\max}} \exp(-i \cdot \Gamma_i) + \exp(-m^{\max} - 1) + \Gamma_i - 1\right)\right). \end{gathered} \tag{4.39}$$

Unlike (4.38), with (4.39), the splitting of very low τ_{con} values close to flux surfaces with integer or half integer q in case of very large Δ^{pol} cannot be reproduced. For consideration of this effect, one needs to replace Γ^i in (4.39) by

$$\Gamma_i' = \Gamma_i \cdot \left(1 - \Theta'\left(\cos\left(i \cdot \frac{2\pi}{q(r_c)}\right) - \cos\left(i \cdot 2\pi\left(\frac{\Delta}{i \cdot \pi r_c} - \frac{R_p^{rad}}{q(r_c)^2} \cdot \left|\frac{dq}{dr}\right|_{r_c}\right) \cdot \Theta'\left(\frac{\Delta}{i \cdot \pi r_c} - \frac{R_p^{rad}}{q(r_c)^2} \cdot \left|\frac{dq}{dr}\right|_{r_c}\right)\right)\right)\right). \tag{4.40}$$

The agreement of (4.39) for typical plasma and plasmoid parameters with a numerical calculation following a representative set of magnetic field lines crossing the plasmoid, is illustrated in figure 7.

For P_{con}, it is also possible to derive an analytical formulation. The problem can be simplified by calculation of the fraction of field-lines departing from a charged plasmoid region that lead to an external connection of oppositely charged potentials for poloidal stripes with zero radial extension of the poloidal plasmoid cross-section and integration in the radial direction. For a given m-number m_i, the distance of the position r_c' of a plasmoid stripe with respect to the next flux surfaces with exact magnetic field line reconnection can be specified in terms of μ as $\Delta\mu = \mu(r_c') - n_i^{inf/sup}/m_i$. From figure 8, one can then infer which points in the positively charged plasmoid region $\Delta^{pol} < y < \Delta^{pol} + 2R_p^{pol}$ are externally reconnected with negative charges for a given plasmoid stripe position $\Delta\mu$. Integrating over the poloidal plasmoid extension and the number of toroidal turns covered at a given time t, one obtains

$$\Gamma_i'' = \Theta'\left(\cos\left(i\cdot\frac{2\pi}{q(r_c')}\right)-\cos\left(\frac{2R_p^{pol}+2\Delta+r_\theta}{r_c'}\right)\right)\cdot\left(1-\Theta'\left(\cos\left(i\cdot\frac{2\pi}{q(r_c')}\right)-\cos\left(\frac{2\Delta+r_\theta}{r_c'}\right)\right)\right),$$

$$P_{con}\left(r_c,R_p^{pol},R_p^{rad},\Delta,v_A,R_0,t\right)=\frac{1}{4R_p^{pol}R_p^{rad}}\cdot\int_{r_\theta=0}^{2R_p^{pol}}\int_{r_c'=r_c-R_p^{rad}}^{r_c+R_p^{rad}}\Theta'\left(\int_{m=0}^{t\cdot v_A/\pi R_0}\sum_{i=1}^{m^{\max}}\delta(m-i)\cdot\Gamma_i''dm\right)dr_c'dr_\theta. \quad (4.41)$$

Here, m^{max} is an integer bigger than $t_{max}\times v_A/\pi R_0$, with t_{max} being the maximum time of interest comparable to the maximum duration of the plasmoid homogenisation process that can be conceived for the simulation conditions under investigation. The computation time for P_{con} can be reduced by an order of magnitude, if the pointwise check of external reconnections in the poloidal direction is replaced by a sectionwise calculation:

$$\Gamma_i'''\left(\mu,R_p^{pol},\Delta,\Delta',r_c'\right)=\Theta'\left(\cos(2\pi i\mu)-\cos\left(\frac{2\left(R_p^{pol}+\Delta+\Delta'\right)}{r_c'}\right)\right)\cdot\left(1-\Theta'\left(\cos(2\pi i\mu)-\cos\left(\frac{2(\Delta+\Delta')}{r_c'}\right)\right)\right),$$

$$\Xi_i\left(R_p^{pol},\Delta,\Delta'',r_c'\right)=\Gamma_i'''\left(\frac{1}{q(r_c')},R_p^{pol},\Delta,\Delta'',r_c'\right)\int_{\mu'=-\infty}^{\infty}\Gamma_i'''\left(\mu',R_p^{pol},\Delta,\Delta''+\frac{R_p^{pol}}{2},r_c'\right)\cdot\Theta\left(\frac{R_p^{pol}}{i^2\pi r_c'}-\left|\mu'-\frac{1}{q(r_c')}\right|\right)d\mu',$$

$$P_{con}\left(r_c,R_p^{pol},R_p^{rad},\Delta,v_A,R_0,t\right)=\frac{1}{2R_p^{rad}}\cdot\int_{r_c'=r_c-R_p^{rad}}^{r_c+R_p^{rad}}\int_{\xi=0}^{1}\prod_{i=1}^{m^{\max}}\int_{m=0}^{t\cdot v_A/\pi R_0}\delta(m-i)\cdot\Theta'\left(\xi-\Xi_i\left(R_p^{pol},\Delta,0,r_c'\right)\right)$$

$$\cdot\Theta'\left(1-\Gamma_i'''\left(\frac{1}{q(r_c')},R_p^{pol},\Delta,R_p^{pol},r_c'\right)+\Xi_i\left(R_p^{pol},\Delta,R_p^{pol},r_c'\right)-\xi\right)dm\,d\xi\,dr_c'. \quad (4.42)$$

With (4.42), L_{con} can be specified as

$$L_{con}\left(r_c,R_p^{pol},R_p^{rad},\Delta,v_A,R_0,t\right)=$$

$$\frac{\displaystyle\int_{m=0}^{t\cdot v_A/\pi R_0}\sum_{i=1}^{m^{\max}}\delta(m-i)\cdot i\cdot 2\pi R_0\left(P_{con}\left(t'=\frac{(i+1/2)\pi R_0}{v_A}\right)-P_{con}\left(t'=\frac{(i-1/2)\pi R_0}{v_A}\right)\right)dm}{\displaystyle\int_{m=0}^{t\cdot v_A/\pi R_0}\sum_{i=1}^{m^{\max}}\delta(m-i)\left(P_{con}\left(t'=\frac{(i+1/2)\pi R_0}{v_A}\right)-P_{con}\left(t'=\frac{(i-1/2)\pi R_0}{v_A}\right)\right)dm}. \quad (4.43)$$

To obtain an estimate for the fraction of a charged plasmoid region with external reconnection to charged regions of the same sign and the associated average reconnection lengths (described as P_{con2}, L_{con2} further below), the central areas shown in figure 8 have to be considered in (4.41) resp. (4.42) instead of the exterior ones. If self-reconnected areas are taken into account, it has to be made sure that field lines do net get attributed to different types of reconnection for different m_i.

4.4.3. Evaluation of the importance of τ_L.

The retardation in the external parallel current formation characterised by a constant electron collision time τ_e as given in (4.22) can be derived by the longitudinal force balance equation for electrons in an ohmic regime:

$$\begin{gathered} m_e \frac{dv_{e\parallel}}{dt} = q_e E_\parallel - \frac{v_{e\parallel} m_e}{\tau_e} \rightarrow v_{e\parallel} = C \cdot e^{-t/\tau_e} + \frac{q_e E_\parallel \tau_e}{m_e}, \\ v_{e\parallel}(0) = 0,\ j_{e\parallel} = n_e q_e v_{e\parallel} \rightarrow j_{e\parallel} = \frac{n_e q_e^2 \tau_e}{m_e} E_\parallel \left(1 - e^{-t/\tau_e}\right) \rightarrow I_\parallel \propto \left(1 - e^{-t/\tau_e}\right). \end{gathered} \tag{4.44}$$

Taking into account the current retardation effect caused by the inductive response of the plasma particles inside and outside the parallel external current circuit, one has, with $\Delta\Phi$ for the difference in electric potential, the total inductance L, the total current $I_{||}$, the effective cross-sectional area A, and the longitudinal extension Z,

$$\begin{gathered} \Delta\Phi = -L \frac{dI}{dt}, \\ E_\parallel^{ind.} = -\frac{LAn_e q_e}{Z} \frac{dv_{e\parallel}}{dt}, \end{gathered} \tag{4.45}$$

which, inserted into (4.44), yields

$$\begin{gathered} \frac{m_e}{q_e} \frac{dv_{e\parallel}}{dt} = E_\parallel - \frac{LAn_e q_e}{Z} \frac{dv_{e\parallel}}{dt} - \frac{v_{e\parallel} m_e}{q_e \tau_e}, \\ \frac{dv_{e\parallel}}{dt} = \frac{E_\parallel}{m_e/q_e + LAn_e q_e/Z} - \frac{v_{e\parallel}}{\tau_e} \frac{1}{1 + LAn_e q_e^2/Zm_e}, \\ j_{e\parallel}(0) = 0, \rightarrow j_{e\parallel} = \frac{n_e q_e^2 \tau_e}{m_e} E_\parallel \left(1 - e^{-t/\tau_e \cdot \left(1 + LAn_e q_e^2/Zm_e\right)}\right) \rightarrow I_\parallel \propto \left(1 - e^{-t/\tau_e + \tau_L}\right), \end{gathered} \tag{4.46}$$

with the characteristic inductive retardation time t L being the ratio between the inductance and the resistance $R = m_e Z/n_e q_e^2 \tau_e A$ of the circuit formed by the connecting flux tubes.

Approximating L by the self-inductance similar to that for a coaxial cable at high frequency [39], $L \approx \mu_0 L_\phi \ln\wp/\pi$, $\ln\wp \sim 1$, and R by 2 , $L_\phi/\sigma_{||\infty} R_p^2 \pi$, τ_L for the Pégourié current formation can be estimated as

$$\tau_L \sim \sigma_{\parallel\infty} R_p^2 \mu_0 . \tag{4.47}$$

For typical values, $\sigma_{\parallel\infty} \sim 10^7\ \Omega^{-1}m^{-1}$, $R_p \sim 1cm$, τ_L is in the order of a millisecond. With such a long retardation time, the Pégourié current would remain negligibly small during the whole homogenisation process. (4.47) must be considered as an upper limit though, as the cross-sectional area of the externally reconnected charged region is smaller than that of the plasmoid. At $t \gtrsim \tau_{con}$, when the deceleration due to the Pégourié effect is at its maximum, the fraction of reconnected flux tubes increases from zero to a few percent. τ_L is then comparable to τ_e.

To analyse the importance of τ_L more in detail, a numeric simulation scheme has been set up. In cylindrical geometry (see figure 9), Faraday's law and the Ampère-Maxwell equation in plasma conditions read with the simplifications $E_r = Eq = 0$, $\partial E_z\, \partial_z = 0$, $B_z = B_r = 0$, and the assumption of rotational symmetry:

$$\begin{aligned} \frac{\partial B_\theta}{\partial t} &= \frac{\partial E_z}{\partial r}, \\ \frac{\partial E_z}{\partial t} &= \frac{1}{\varepsilon_0 \varepsilon}\left(\frac{1}{\mu_0}\frac{1}{r}\frac{\partial}{\partial r}(rB_\theta) - j_z\right), \varepsilon \sim \frac{c^2}{v_A^2}. \end{aligned} \tag{4.48}$$

Neglecting the current, this equation system yields the propagation of electromagnetic field perturbations at Alfvénic speed as illustrated in figure 10.

With j_z taken into account, a third equation is needed which can be obtained from Ohm's law as given in (4.44):

$$\frac{\partial j_z}{\partial t} = \frac{1}{\tau_e}\sigma_{z\infty}E_z e^{\frac{-t}{\tau_e}} = \frac{1}{\tau_e}(\sigma_{z\infty}E_z - j_z). \tag{4.49}$$

By prescription of a Pégourié current profile j_{zS} for $\tau_L = 0$ as calculated by (4.49) for a timeinvariant E_z profile as shown in figure 10a at $t = 0$, thus approximating the external parallel current for a plasmoid by a cylindrical, unidirectional surface distribution (see figure 9), one can determine the strength of the counter-current induced by the plasma. Comparing the maximum of the total current as given by (4.48-49) with that of j_{zS} in the initial current rise phase, τ_L can be estimated by the following relation:

$$\frac{j_{zS}(t\sim 0)}{j_{tot}(t\sim 0)} \approx \frac{\partial j_{zS}(t\sim 0)}{\partial t}\cdot\left(\frac{\partial j_{tot}(t\sim 0)}{\partial t}\right)^{-1} = \frac{\tau_e + \tau_L}{\tau_e}. \tag{4.50}$$

Numerical simulations of the inductive current response were done for plasmoids with varying crosssectional area in typical plasma conditions ($B_0 \sim 3T$, $n_\infty \sim 5\times10^{19}m^{-3}$, $T_\infty \sim 2keV$). The result for the relation of the retardation time defined in (4.50) is summarised in table 2 and compared with an analytic assessment following (4.47) for the definition of τ_L.

As can be seen, the quadratic dependence on the plasmoid radius in (4.47) can be reproduced in the simulations. In absolute values, τ_L is reduced by a factor of 10 compared to the analytic estimate. Still, it must be interpreted as an upper limit for the real inductive retardation time, as the numeric

calculation is done for idealised conditions, in which the total inductive counter-current can obtain the same size as the total Pégourié current. In reality, the counter current is damped by effects related to the finiteness of the current carrying flux tubes. Furthermore, the charge accumulation due to the curvature drift is supposed to be mainly located at the plasmoid edge at a time $\tau_e \sim \tau_{con}$, when the drift velocity has reached its maximum; the cross-sectional area with Pégourié currents is then much smaller compared to R_p^2 than in the simulations. In addition, the numerical calculation was performed for a unidirectional Pégourié current, for which the inductive response is expected to be stronger than in reality, where currents flow in both directions. Allowing for these considerations, τ_L and τ_e might be even in the same order of magnitude, at least for smaller plasmoids in the initial phase of the Pégourié current formation.

A simulation case with R_p=10cm is illustrated in figures 11, 12. Only the very initial time is drawn to show the decline of an initial plasma wave, which is the solution of (4.48-49) for negligible B_θ.

4.4.4. Advanced description of the external current.

For time-dependent quantities $E_{||}(t)$ and $\tau_e(t)$,the derivation of $j_{e||}$ in (4.44) changes as follows:

$$
\begin{aligned}
& m_e \frac{dv_{e\|}}{dt} = q_e E_\| - \frac{v_{e\|} m_e}{\tau_e}, \text{ansatz: } v_{e\|} = C(t)\cdot e^{-\int_0^t dt'/\tau_e}, \\
\rightarrow & \frac{dv_{e\|}}{dt} = \frac{dC}{dt}\cdot e^{-\int_0^t dt'/\tau_e} - \frac{v_{e\|}}{\tau_e} = \frac{q_e E_\|}{m_e} - \frac{v_{e\|}}{\tau_e},\ \frac{dC}{dt} = \frac{q_e E_\|}{m_e}\cdot e^{\int_0^t dt'/\tau_e}, \\
& v_{e\|} = \left(\frac{q_e}{m_e}\int_0^t E_\|(t') e^{\int_0^{t'} dt''/\tau_e(t'')} dt' + C' \right)\cdot e^{-\int_0^t dt'/\tau_e(t')}, C' \ldots \text{const.}, \\
& v_{e\|}(0) = 0 \rightarrow j_{e\|} = \frac{n_e q_e^2}{m_e} e^{-\int_0^t dt'/\tau_e(t')} \cdot \int_0^t E_\|(t') e^{\int_0^{t'} dt''/\tau_e(t'')} dt'.
\end{aligned}
\tag{4.51}
$$

The integral containing $E_{||}$ can be expanded to

$$
\begin{aligned}
\int_0^t E_\|(t') e^{\int_0^{t'} dt''/\tau_e(t'')} dt' &= E_\|(t)\int_0^t e^{\int_0^{t'} dt''/\tau_e(t'')} - \int_0^t dE_\|(t')/dt' \cdot \int_0^{t'} e^{\int_0^{t''} dt'''/\tau_e(t''')} dt''dt', \\
&= E_\|(t)\left(\tau_e(t) e^{\int_0^t dt'/\tau_e(t')} - \tau_e(0) - \int_0^t d\tau_e(t')/dt' \cdot e^{\int_0^{t'} dt''/\tau_e(t'')} \right) \\
&- \int_0^t dE_\|(t')/dt' \cdot \left(\tau_e(t') e^{\int_0^{t'} dt''/\tau_e(t'')} - \tau_e(0) - \int_0^{t'} d\tau_e(t'')/dt \cdot e^{\int_0^{t''} dt'''/\tau_e(t''')} dt'' \right) dt'.
\end{aligned}
\tag{4.52}
$$

The electron collision time for the ambient plasma decreases considerably after pellet injection, but it changes slightly during the homogenisation process for one single plasmoid. The error is therefore

small, if its time derivative is disregarded. For the parallel electric field, the opposite is true, since the drift deceleration rate is expected to reach the maximum when the Pégourié current builds up. As the second term in (4.52) is always positive, the strength of the Pégourié effect is underestimated without it. By similarity with the current proportionality in (4.46), it follows for $I_{||}$ from (4.51-52):

$$I_{\|}(t) \propto \left[1 - \frac{1}{\tau(t) X(t)} \left(\tau(0) + \int_0^t d\tau(t')/dt \cdot X(t') dt' \right) \right.$$
$$\left. - \frac{1}{\tau(t) X(t) E_{\|}(t)} \int_0^t dE_{\|}(t')/dt \cdot \left(\tau(t') X(t') - \tau(0) - \int_0^{t'} d\tau(t'')/dt \cdot X(t'') dt'' \right) dt' \right], \qquad (4.53)$$
$$\tau(t) := \tau_e(t) + \tau_L(t), \;\; X(t) := e^{\int_0^t dt'/\tau(t')}.$$

As τ_L may vary significantly during the homogenisation process due to its dependence on the plasmoid geometry, all implicit and explicit dependencies on the time derivative of t (t) have been kept. With (4.53), a more precise expression for the drift equation describing the Pégourié effect reads

$$m_i n_i \frac{du_D}{dt} = \frac{2(p_i + p_e - p_{i\infty} - p_{e\infty})}{R} - u_D \frac{\Theta(t - \tau_{con}) \sigma_{\|\infty} B_{\|}^2 L_b L_{J\phi}}{Z_0 (L_\phi - Z_0)} \left[1 - \frac{1}{\mathrm{X}\tau} \left(\tau(\tau_{con}) + \int_{\tau_{con}}^t d\tau/dt \cdot \mathrm{X} dt' \right) \right]$$
$$- \frac{\Theta(t - \tau_{con}) \sigma_{\|\infty} B_{\|} L_{J\phi}}{Z_0 \mathrm{X} \tau} \int_{\tau_{con}}^t \left[\left(\frac{du_D}{dt} \frac{B_{\|} L_b}{L_\phi - Z_0} + u_D \frac{B_{\|}}{L_\phi - Z_0} \left(\frac{dL_b}{dt} + \left(\frac{dZ_0}{dt} - \frac{dL_\phi}{dt} \right) \frac{L_b}{L_\phi - Z_0} \right) \right) \right. \qquad (4.54)$$
$$\left. \cdot \left(\mathrm{X}\tau - \tau(\tau_{con}) - \int_{\tau_{con}}^{t'} d\tau/dt \cdot \mathrm{X} dt'' \right) \right] dt', \;\; \mathrm{X}(t) := e^{\int_{\tau_{con}}^t dt'/\tau(t')}.$$

This equation can only be expressed implicitly and solved iteratively. If one is interested in a drift equation that only considers an absolute lower limit for the strength of the Pégourié effect in typical plasmoid homogenisation cases, with τ_L replaced by a constant upper limit $\hat{\tau}_L$, (4.54) reduces to

$$m_i n_i \frac{du_D}{dt} = \frac{2(p_i + p_e - p_{i\infty} - p_{e\infty})}{R} - u_D \frac{\Theta(t - \tau_{con}) \sigma_{\|\infty} B_{\|}^2 L_b L_{J\phi}}{Z_0 (L_\phi - Z_0)} \left(1 - \underbrace{\frac{\tau(\tau_{con})}{\tau}}_{\sim 1 \text{ for const. } \hat{\tau}_L} e^{-\int_{\tau_{con}}^t dt'/\tau(t')} \right). \qquad (4.55)$$

For the sake of simplicity, the effect of further amendments to the definition of the external currents on the drift equation will be demonstrated on basis of (4.55).

With the help of numeric calculations, the fraction of externally reconnected charges P_{con} as introduced in (4.22) can be determined. It helps to further refine the description of the Pégourié effect, however, a trade-off has to be made against a significant increase in computation time for the simulation of the plasmoid homogenisation process. In principle, an algorithm that is capable to give an estimate for the time dependence of P_{con} must follow the external propagation of the

electric potential at Alfvénic speed for a representative set of magnetic field lines departing from the charged regions of the plasmoid. If a reconnection occurs with a flux tube carrying a potential of opposite sign after a time trec , the corresponding charged fraction of the plasmoid is attributed to Pcon for $t > t_{rec}$.

One obtains a step-like function with discontinuities at $t \sim m \times \pi R_0/v_A$, $m \in N$. The same is true for the associated average connection length, which was approximated in (4.25) by L_ϕ. One has to distinguish between the harmonic average, labelled henceforward LconH , and the arithmetic average, L_{conA}. The first has to be used, when it is part of the description for the strength of the ohmic resistance like in (4.25), since the flux tubes carrying the Pégourié current are coupled in parallel. The resistance for each flux tube then adds up harmonically. L_{conA} has to be applied in volume descriptions of the background plasma in the flux surface shell carrying the plasmoid. An example for the time evolution of P_{con}, L_{conH}, and L_{conA} for two plasmoids, one deposited on a low order rational surface, the other in close proximity to it, is shown in figure 13.

For a refined treatment of the Pégourié effect, one must also take into account that flux tubes with the same polarization can also reconnect. In this case, there is no external depletion current. The fraction of charge reconnections of the same type, denoted in the following as P_{con2}, evolves similarly to P_{con}, as do the associated average connection lengths L_{conH2}, L_{conA2} with respect to L_{conH}, L_{conA}, but the time when P_{con2} reaches the asymptotic maximum, and the relation P_{con2}/P_{con} vary in dependence of magnetic shear and the vicinity of rational flux surfaces. I Yu Senichenkov has proven that for the one-dimensional wave equation with Alfvénic wave speed, the plasmoid mass deposited punctiformally as periodic boundary condition with the reconnection length L_{conA2} as periodic length, and initial pulses of the transversal electric field $E_{\perp 0}$ at the plasmoid position, an analytic approximation to the solution of the time evolution can be given by Laplace transformation, which asymptotically approaches the constant spatial distribution [40]

$$E_{\perp\infty} = \frac{2E_{\perp 0}}{2 + \dfrac{B_\parallel^2 L_{conA2}}{\mu_0 v_A^2 Z_0 n_0 m_i}} = \frac{E_{\perp 0}}{1 + \dfrac{P_{con2} M_0}{M_{0,Lcon2} - M_0}}, \tag{4.56}$$

with the mass definitions

$$M_0 = L_a L_b Z_0 n_0 m_i, \quad M_{0,Lcon2} = M_0 + \frac{1}{2} P_{con2} L_a L_b L_{conA2} n_\infty m_i. \tag{4.57}$$

If $E_\perp$ is replaced by u_D in (4.56), the equation can be interpreted as a drift momentum conservation law. When the plasma particles in flux tubes belonging to the fraction P_{con2} of charged regions start to drift due to the constant transversal electric field that has built up there, momentum is transferred from the plasmoid to the background plasma. In the drift equation, this behaviour is expressed through an increased inertial mass $M_{0,Lcon2}$ instead of M_0. Since the transversal electric field inside

a flux tube rotates at the same rate as the flux tube rotates around the magnetic axis of the tokamak, its scalar product with the gradient of a flux surface label remains constant. The amount of drift described in flux surface label coordinates for flux tube particles in the inner and outer half of the tokamak is therefore roughly the same and no geometric corrections allowing for the non-local distribution of the flux tube particles are required.

With the Alfvén wave-induced damping effect applied to the fraction of charges that are not externally reconnected, i.e. $1–P_{con}–P_{con2}$, (4.55) transforms with the above-mentioned considerations into

$$M_{0,Lcon2}\frac{du_D}{dt}=\frac{2M_0\left(p_i+p_e-p_{i\infty}-p_{e\infty}\right)}{n_0 m_i R}-u_D\left[\frac{2\left(1-P_{con}-P_{con2}\right)B_{\parallel}^2 L_a L_b}{\mu_0 v_A}\right.$$
$$\left.+\frac{\Theta\left(t-\tau_{con}\right)P_{con}\sigma_{\parallel\infty}B_{\parallel}^2 L_a L_b^2 L_{J\phi}}{\left(L_{conH}-Z_0\right)}\left(1-e^{-\int_{\tau_{con}}^{t}dt'/\tau(t')}\right)\right]. \tag{4.58}$$

4.4.5. Poloidal dependence of external current formation.

In Subsubsection 4.4.2, an analytical description of τ_{con}, P_{con}, and L_{con} has been given for the case of a pellet being injected close to the equatorial plane (pellet injection angle $\alpha \sim 0$ for HFS and $\alpha \sim \pi$ for LFS injections). In this case, the tangent to the flux surfaces is in line with the curvature drift and charges of both signs are equally distributed along a flux surface. The fraction of reconnected charged regions P_{con} can then be described by an expression as given in (4.42). In the case of inclined injections with $\pi > \alpha > 0$ or $-\pi < \alpha < 0$, it may happen though that the distribution of positively and negatively charged regions on a given flux surface within the plasmoid becomes asymmetric, causing a decrease in the probability for an external reconnection of oppositely charged domains. In the most extreme case $\alpha = \pm\pi/2$, the accumulated charges within a plasmoid cannot reconnect at all with those of the opposite sign, i.e. $P_{con} = 0$ at all times. Figure 14 illustrates this behaviour. To take it into account, an a-dependent correction term needs to be introduced in P_{con}.

In the following, attempts will be made to quantify approximately the influence of the poloidal location of the plasmoid on the drift damping via P_{con}. It will be assumed that the charge accumulation takes place in a small layer surrounding the plasmoid (corresponding to the initial phase in the plasmoid expansion process, see figure 15).

The charges accumulated on a magnetic field line per unit of length are taken to be proportional to cos(h). Therefore, the total relative charge deposition along a magnetic field line can be calculated as

$$\delta q\left(\eta, Z_0\right)=\frac{qR_0}{2Z_0}\int_{\eta-Z_0/qR_0}^{\eta+Z_0/qR_0}\cos(\theta)d\theta=\frac{qR_0}{Z_0}\sin\left(Z_0/qR_0\right)\cos(\eta) \tag{4.59}$$

If the plasmoid is deposited on the mid-plane, the magnetic field lines can connect vertically aligned charges of opposite sign, described by the angles η and $\pi-\eta$. If the plasmoid is deposited elsewhere,

the pellet injection angle α, which is equal to the angle between the magnetic field lines projected on the poloidal plane and the vertical direction, needs to be considered. In this situation, charges located at an angular position of η and $\pi - 2\alpha - \eta$ can be reconnected with each other (the poloidal rotation of the magnetic field lines inside the plasmoid with increasing parallel distance to the plasmoid centre does not alter this relation). The scheme of possible reconnections between different charges is shown in figure 16.

With (4.59), the efficiency of parallel currents compared to the case $\alpha = 0$ can be described by a factore, taking the difference δq at the two positions where charges are located on the same flux surface, and integrating over one half of the plasmoid domain in terms of η:

$$\varepsilon'(\alpha, Z_0) = \frac{1}{2\pi} \cdot \int_{-\pi/2}^{\pi/2} \delta q(\theta, Z_0) - \delta q(\pi - 2\alpha - \theta, Z_0) d\theta = \frac{2qR}{\pi Z_0} \sin(Z_0/qR) \cos^2(\alpha),$$
$$\varepsilon(\alpha) := \varepsilon'(\alpha, Z_0) / \varepsilon'(0, Z_0) = \cos^2(\alpha). \tag{4.60}$$

The reduction in δq with increasing plasmoid extension Z_0 is not related to external reconnection properties, as it corresponds to an averaging of charge concentrations along a magnetic field line via plasmoid-internal parallel currents, i.e. the Rozhansky effect. As the latter acts directly on the drift driving term and does not alter the fraction of externally reconnected charged regions, the Z_0 dependence has been removed in the normalisation in (4.60). The modification of the drift driving term in accordance with the Rozhansky effect is addressed in Subsection 4.2. For P_{con}, only the a dependent term is relevant. The reduction in the efficiency of the Pégourié currents for more inclined pellet injection directions is caused by a decrease in P_{con}, whose α-dependence can be expressed in first order approximation as

$$P_{con}(\alpha) \sim P_{con}(\alpha = 0) \cdot \varepsilon(\alpha), \tag{4.61}$$

with the fraction of self-reconnected charges P_{con2} increasing accordingly,

$$P_{con2}(\alpha) \sim P_{con2}(\alpha = 0) + P_{con}(\alpha = 0) \cdot (1 - \varepsilon(\alpha)). \tag{4.62}$$

If one can assume that the proportionality $P_{con}(\alpha,t) \infty P_{con}(\alpha = 0,t)$ holds approximately, the α–dependencies of L_{con} and τ_{con} are very small and can be neglected.

In figure 17, the change of the deposition profile barycentre with respect to the pellet injection angle a is plotted for realistic (JET L-mode) plasma conditions. If the α-dependence of P_{con} is accounted for, the outward drift is increased for vertical injections. Even in the case of an exactly vertical pellet injection with $\alpha = \pm\pi/2$, the drift damping due to Pégourié currents may still be present though. As soon as the plasmoid starts to drift, it will reach a region where a deviates from $\pm\pi/2$ and P_{con} becomes non-zero. In addition, the real structure of the charge distribution in the plasmoid region

may quickly start to diverge from that depicted in figure 15 due to the evolution of the plasmoid shape during the homogenisation process, and more complex patterns can emerge that would allow a reconnection of opposite charges even at $\alpha = \pm\pi/2$. Nevertheless, (4.61) seems to be a quite robust approximation to the actual a-dependence of P_{con}, as it can be shown that the main trend described by the cos2 (a) term is quite independent of the details in the assumptions for the plasmoid charge distribution.

4.4.6. The rational q surface effect.

As shown in figure 7, τ_{con} strongly depends on the structure of the safety factor profile. In the vicinity of rational flux surfaces, τ_{con} is reduced, because the external electric potential reconnection can be established after just a few toroidal turns. A significant reduction can therefore also be observed for the average reconnection length L_{conH} (Figure 13a), and the initial (averaged) time derivative for P_{con} is increased (Figure 13a). From (4.58), it follows that the braking of the plasmoid drift engendered by the Pégourié effect is particularly strong, if the cloudlet is deposited close to flux surfaces with rational q.

At a distance ~ L_a to these surfaces, the opposite tendencies can be observed for τ_{con}, L_{conH}, and dP_{con} ($t \sim \tau_{con}$) dt, the shift in poloidal angle after a toroidal turn being still very small, but already exceeding the size allowing for an immediate reconnection. As a consequence, a particularly high number of further toroidal turns is required until the poloidal shift has summed up to at least one poloidal turn. The reconnection is then delayed, taking place at a time $t \sim 2\pi^2 R_0 r/v_A L_b$, and the Pégourié drift damping is weakened.

In total, the latter effect is clearly overweighed by the first one, as can be seen in figures 7 and 18. The high density of flux surfaces with rational q numbers of higher order, the finite radial extension of the plasmoid, and the fact that lower values receive more weight in the harmonic average LconH are the cause for this asymmetry. One can therefore expect an enhanced drift deceleration in proximity to rational q surfaces, which also affects the shape of the pellet particle deposition profile (figure 18b).

If the plasmoid drift displacement is to be considered as a first order correction to the complete pellet material deposition process, which is already difficult to measure with a satisfying degree of accuracy, the additional drift damping at rational q surfaces is an effect of the second order, whose experimental validation is a particularly demanding challenge. Still, in dedicated experiments at Tore Supra and DIII-D, signs of evidence for a variation of the average particle drift for a whole pellet with respect to integer q surfaces have been observed in a statistical analysis [41,42]. The relation between the positions of maximum particle ablation and deposition seems to be radially discontinuous (figure 19), which is a clear hint for the validity of the Pégourié effect and its importance in relation to other drift damping mechanisms in tokamaks. Recently, it was even possible to demonstrate the existence of a dependence between the local drift displacement and the proximity to rational q surfaces of lower order for individual pellets, measuring the temporary deposition profile during the

ablation process with high resolution reflectometry diagnostics in dedicated Tore Supra discharges ([35], see figure 20), leaving no doubt about the Pégourié effect being the dominant ingredient in the drift deceleration process in axisymmetric magnetic configurations.

4.5. EVALUATION OF THE DRIFT EQUATION TERMS

The plasmoid drift equation (4.8) with the terms proportional to the drift velocity taken from (4.58) has been solved for idealised conditions without consideration of geometric effects affecting the plasmoid evolution with respect to the magnetic flux surface distribution, whose treatment is described in the next section. The target plasma properties correspond to the JET hybrid mode Pulse No: 77864 at the time t = 7.3s, with the plasmoid released at a distance of ~25cm to the scrape-off layer measured along the VHFS injection trajectory. The initial conditions for the plasmoid were derived by solution of (2.2), assuming r_p = 1mm for the calculation of the pellet particle ablation rate. To compare the relative strength of the various drift accelerating or decelerating terms in the drift equation, the drift velocity has been recalculated, omitting either the term describing the Alfvén wave dissipation, the Pégourié effect, the Rozhansky effect, or the enhanced acceleration caused by the longitudinal expansion of the plasmoid proposed by P B Parks et al.. The results are illustrated in figure 21. Whereas the contribution of Alfvén wave dissipation only amounts to a reduction of the drift displacement of ~8%, the latter is enhanced by a factor of six, if the Pégourié effect is neglected. The Rozhansky damping causes a total change of 50% of the drift displacement, however, with geometric effects taken into account, the effect would be much smaller, as it is most important at a time, where the plasmoid has already reached locations with poloidal angles covering a large interval close to p. Without enhanced acceleration caused by dZ_0/dt , the plasmoid drifts at a speed that is ~20% lower. According to these results, the Pégourié effect is by far the most important for the determination of the drift displacement based on (4.53,4.60) for tokamak plasmas. For stellarators, it only seems to play a subordinate role though; here, the drift reduction is mainly determined by the Rozhansky effect, since the magnetic reconnection length is smaller (cf. Subsubsection 7.2.4).

5. PLASMOID CLOUD DYNAMICS

For the solution of the plasmoid drift equation, the properties and geometric extensions of the plasmoid and that of the background plasma in the flux surface shell where the cloudlet is located must be known. In this section, a model for the assessment of the time evolution for these quantities is given. The cloudlet and the surrounding plasma are interpreted as two interacting fluid cells, whose dynamics is governed by energy and particle conservation. The model was derived by B Pégourié [34,4] on basis of [25]. Recent modifications, supplements and simplifications with respect to [4] will be described more in detail.

5.1. DESCRIPTION OF BASIC AND AUXILIARY PHYSICAL QUANTITIES

For the derivation of the main equations of the model, the following definitions of physical quantities

are employed: [22,43]

Coulomb logarithm:

$$\lambda_{0/\infty} = \left(\ln\Lambda\right)_{0/\infty} \sim 24 - \ln\left(\sqrt{\frac{n_{0/\infty}}{10^6}}\frac{1}{T^e_{0/\infty}}\right). \tag{5.1}$$

Gyro-frequencies and collision times for electrons and ions:

$$\Omega^{e/i}_{0/\infty} = 1.76\cdot 10^{11} B_{\|}\frac{m^e}{m^{e/i}_{0/\infty}}, \tag{5.2}$$

$$\tau^e_{0/\infty} = 3.44\cdot 10^{11}\frac{\left(T^e_{0/\infty}\right)^{1.5}}{n_{0/\infty}\lambda_{0/\infty}},\ \tau^i_{0/\infty} = 2.09\cdot 10^{13}\frac{\left(T^i_{0/\infty}\right)^{1.5}\sqrt{A^i}}{n_{0/\infty}\lambda_{0/\infty}}. \tag{5.3}$$

Electron-ion collision frequency:

$$\nu^{ie}_{0/\infty} = 3.2\cdot 10^{-15}\frac{n_{0/\infty}\lambda_{0/\infty}}{\left(T^e_{0/\infty}\right)^{1.5}}. \tag{5.4}$$

Plasma sound velocity:

$$C_{s\,0/\infty} = \sqrt{\frac{\gamma k_B\left(T^e_{0/\infty}+T^i_{0/\infty}\right)}{m^i_{0/\infty}}}. \tag{5.5}$$

Parallel and transversal collisional thermal conductivities $K_{\|}{}^{e/i}{}_{/\perp 0/\infty}$:

$$\begin{gathered}\kappa^e_{\|0/\infty} = 0.032\frac{n_{0/\infty}k_B T^e_{0/\infty}\tau^e_{0/\infty}}{m^e_{0/\infty}},\ \kappa^i_{\|0/\infty} = 0.039\frac{n_{0/\infty}k_B T^i_{0/\infty}\tau^i_{0/\infty}}{m^i_{0/\infty}},\\ \kappa^{e/i}_{\perp 0/\infty} = 0.025\frac{n_{0/\infty}k_B T^{e/i}_{0/\infty}}{m^{e/i}_{0/\infty}\Omega^{e/i}_{0/\infty}}.\end{gathered} \tag{5.6}$$

Braginskii coefficients for viscosity (for essentially parallel velocity shear):

$$\begin{gathered}\eta^e_{00/\infty} = 7.3\, n_{0/\infty}k_B T^e_{0/\infty}\tau^e_{0/\infty},\ \eta^i_{00/\infty} = 9.6\, n_{0/\infty}k_B T^i_{0/\infty}\tau^i_{0/\infty},\\ \eta^e_{20/\infty} = 20\frac{n_{0/\infty}k_B T^e_{0/\infty}}{\left(\Omega^e\right)^2\tau^e_{0/\infty}},\ \eta^i_{20/\infty} = 12\frac{n_{0/\infty}k_B T^i_{0/\infty}}{\left(\Omega^i_{0/\infty}\right)^2\tau^i_{0/\infty}}.\end{gathered} \tag{5.7}$$

A^i is the atomic mass number, g the ratio of the specific heats for constant pressure and volume. For better readability, particle type labels are shown as superscripts in this section.

Further introducing the magnetic shear length and the associated gradient lengths for thermal conductivities and viscosity,

$$\begin{gathered}L_s = \frac{q^2}{dq/d\rho}\frac{R_0}{\rho_M},\\ L^{e/i}_{\|/\perp 0/\infty} = \sqrt{\int_0^t \pi\,\kappa^{e/i}_{\|/\perp 0/\infty}\Big/ n_{0/\infty}\,dt'},\\ L_{\eta\,0/\infty} = \sqrt{\int_0^t \pi\left(\eta^i_{20/\infty}\Big/\left(n_{0/\infty}m^i_{0/\infty}\right)\right)dt'},\end{gathered} \tag{5.8}$$

ρ_M being the plasmoid barycentre in terms of minor radius flux surface coordinates, formulations can be obtained for the relative increase in L_a (and decrease in L_b), averaged in the parallel direction, due to magnetic shear distortion effects,

$$\sigma_s = \frac{1}{Z_0}\int_0^{Z_0}\sqrt{1+(z/L_s)^2}\,dz, \tag{5.9}$$

for the effective thermal conductivities at the interface between the plasma and the plasmoid,

$$\mathrm{K}_{\parallel/\perp}^{e/i} = \frac{\kappa_{\parallel/\perp 0}^{e/i} n_\infty L_{\parallel/\perp\infty}^{e/i}}{n_0 L_{\parallel/\perp 0}^{e/i} + n_\infty L_{\parallel/\perp\infty}^{e/i}} \frac{L_{\parallel/\perp\infty}^{e/i}}{L_{\parallel/\perp 0}^{e/i}}, \tag{5.10}$$

and the volume-integrated internal and shear viscosity energy loss inside and outside the plasmoid,

$$\begin{aligned} W_0^{e/i} &= \frac{4}{3} L_a L_b \eta_{00}^{e/i} \frac{1}{Z_0}\left(\frac{dZ_0}{dt}\right)^2 + \eta_{20}^{e/i}\left(\frac{dZ_0/dt - V_s}{L_{\eta 0}}\right)^2 Z_0 L_a \min\left(L_{\eta 0}, \frac{L_b}{2}\right), \\ W_\infty^{e/i} &= \frac{4}{3} L_a L_b \eta_{0\infty}^{e/i} \frac{1}{L_\phi - Z_0}\left(\frac{dZ_0}{dt}\right)^2 \frac{M_{eff} - N_0 m_0^i}{N_\infty m_\infty^i} + \frac{\eta_{2\infty}^{e/i}}{2}\left(\frac{V_s}{L_{\eta\infty}}\right)^2 Z_0 L_a \min\left(L_{\eta\infty}, \frac{L_b}{2}\right), \end{aligned} \tag{5.11}$$

with the average velocity at the interface between the plasmoid and the plasma

$$V_s = \frac{dZ_0/dt}{2}\left[1 + \frac{(Z_0 + L_{\eta\infty})\eta_{2\infty}^i L_{\eta 0}^2}{(Z_0 + L_{\eta 0})\eta_{20}^i L_{\eta\infty}^2}\right]^{-1}. \tag{5.12}$$

With the upper limit for the free parallel and transversal heat fluxes (assuming a sheath transmission factor of $e^{-1.}$),

$$\begin{aligned} q_\parallel^e &= \frac{k_B\left(T_\infty^e - T_0^e\right)}{2} e^{-1.8} n_\infty \sqrt{\frac{8k_B T_\infty^e}{\pi m_\infty^e}}, \\ q_\parallel^i &= \frac{k_B\left(\left(T_\infty^i - T_0^i\right) + 1.8\left(T_\infty^e - T_0^e\right)\right)}{2} n_\infty \sqrt{\frac{8k_B T_\infty^i}{\pi m_\infty^i}}, \\ q_\perp^{e/i} &= \frac{\mathrm{K}_\perp^{e/i}}{\sigma_s \mathrm{K}_\parallel^{e/i}} q_\parallel^{e/i}, \end{aligned} \tag{5.13}$$

the power transfer from the plasma to the plasmoid can be estimated as

$$Q_{\infty 0}^{e/i} = L_a\left(2Z_0 q_\perp^{e/i} + L_b q_\parallel^{e/i}\right). \tag{5.14}$$

The heat exchange term between electrons and ions can be given as

$$Q_{0/\infty}^{ie} = \frac{N_{0/\infty}\nu_{0/\infty}^{ie} k_B\left(T_{0/\infty}^i - T_{0/\infty}^e\right)}{\gamma - 1}. \tag{5.15}$$

5.2. DERIVATION OF THE MODEL EQUATIONS

For symmetry reasons, it is sufficient to calculate the plasmoid dynamics in "plasmoid geometry", i.e. half of the flux surface shell volume with positive coordinates z > 0 for the dimension along the magnetic field lines only, supposing that the barycentre of the plasmoid is situated at z = 0. Z_0 is then just half of the parallel plasmoid extension, and N0 is half of the initial total plasmoid particle content, i.e. $n0L_aL_bZ_0$.

With the gradient length for collisional diffusion,

$$L_{n_0} = \sqrt{\int_0^t \pi D_0 dt'}, \tag{5.16}$$

(D_0 describing the classical collisional or anomalous diffusivity inside the plasmoid), the transversal plasmoid particle losses to the background plasma of the same flux surface shell can be taken to be equal to the particle flux – i.e. the difference in density divided by L_{n0} and multiplied by D_0 –, integrated over the poloidal and radial plasmoid surfaces. N0 then varies at a rate:

$$\frac{dN_0}{dt} = -2 \cdot \frac{n_0 - n_\infty}{L_{n_0}} D_0 Z_0 \left(L_a + L_b\right). \tag{5.17}$$

(D_0 describing the classical collisional or anomalous diffusivity inside the plasmoid), the transversal plasmoid particle losses to the background plasma of the same flux surface shell can be taken to be equal to the particle flux – i.e. the difference in density divided by L_{n0} and multiplied by D0 –, integrated over the poloidal and radial plasmoid surfaces. N_0 then varies at a rate:

$$\frac{dN_\infty}{dt} = \frac{1}{2} n_\infty(\rho) \left(\frac{dV}{d\rho}\right)_{\rho_M} \cdot \left|\frac{d\rho_M}{dt}\right| + 2 \cdot \frac{n_0 - n_\infty}{L_{n_0}} D_0 Z_0 L_a \,, \tag{5.18}$$

In tokamak plasmas with low elongation, $(dV/d\rho)\,\rho_M \sim 4\pi^2 R_0 \rho_M$. The change in the composition of the background plasma particles can be expressed by the time derivative of the average particle mass:

$$\frac{dm_\infty^i}{dt} = \frac{dN_0}{dt} \frac{1}{N_\infty} \left(m_\infty^i - m_0^i\right). \tag{5.19}$$

According to the dilatation of the considered plasma volume as accounted for in (5.18), assuming an initial poloidal plasmoid cross-section of circular shape, $A = R_p^2\pi$, which is not conserved with increasing radial plasmoid width, the poloidal plasmoid extensions can be defined as

$$\begin{gathered} L_{a\mathrm{ini}} = L_a(t=0) = L_b(t=0) = \sqrt{\pi} R_p \,, \\ L_a = \sigma\left(L_{a\mathrm{ini}} + \left| \int_{t'=0}^{t} d\rho_M / dt' \cdot dt' \right| \right), \quad L_b = \frac{L_{a\mathrm{ini}}}{\sigma}. \end{gathered} \tag{5.20}$$

It follows for the time derivatives:

$$\frac{dL_a}{dt} \approx \frac{d\sigma}{dt} \frac{L_a}{\sigma} + \sigma \left|\frac{d\rho_M}{dt}\right|, \quad \frac{dL_b}{dt} = -\frac{L_b}{\sigma} \frac{d\sigma}{dt}. \tag{5.21}$$

In the following, an approximation similar to that in [4] will be applied,

$$\frac{dL_a}{dt} \approx L_{a\,\mathrm{ini}} \frac{d\sigma_s}{dt} + \left|\frac{d\rho_M}{dt}\right|, \quad \frac{dL_b}{dt} = -L_{a\,\mathrm{ini}} \frac{d\sigma_s}{dt} \frac{L_b}{L_a}, \tag{5.22}$$

presuming a purely radial E×B particle drift. With this assumption, the drift direction is not aligned with the change in pitch angle of the magnetic field lines. This may only be relevant though, if at all, in regions with exceptionally large shear.

For L_ϕ (which is just half of the average external plasmoid self-connection length in plasmoid geometry), one has $L_\phi\,(t=0)\ 2\pi^2 R_0 \rho_M / L_b$. For $t > 0$, L_ϕ has to be defined indirectly by the time evolution of the flux surface shell volume, where the plasmoid is located, $\Delta V\,(t)$, since usually $\sigma \neq 1$, and L_b is not in line with the poloidal direction. Applying (5.22), we get

$$\begin{aligned} \frac{dL_\phi}{dt} &= \frac{1}{L_a L_b}\frac{d\Delta V}{dt} - L_\phi\left(\frac{1}{L_a}\frac{dL_a}{dt} + \frac{1}{L_b}\frac{dL_b}{dt}\right) \\ &= \frac{2\pi^2 R_0}{L_b}\left[\left(1+\frac{\rho_M}{L_a}\right)\left|\frac{d\rho_M}{dt}\right| + \frac{L_{a\mathrm{ini}}\rho_M}{L_a}\frac{d\sigma_s}{dt}\right] - \left|\frac{d\rho_M}{dt}\right|\frac{L_\phi}{L_a} \\ &\sim \left|\frac{d\rho_M}{dt}\right|\left(\frac{2\pi^2 R_0}{L_b}\frac{\rho_M}{L_a} - \frac{L_\phi}{L_a}\right). \end{aligned} \tag{5.23}$$

The internal energy balance equations for the plasmoid particles consist of terms describing the heat losses to the background plasma, the heat exchange between electrons and ions, convective losses, and the dissipation of kinetic energy due to viscosity and the work done in the longitudinal expansion process (contributions from transversal expansion are omitted):

$$\frac{dE_0^e}{dt} = Q_{\infty 0}^e + Q_0^{ie} + \frac{1}{N_0}\frac{dN_0}{dt}E_0^e + W_0^e - p_0^e L_a L_b \frac{dZ_0}{dt}, \tag{5.24}$$

$$\frac{dE_0^i}{dt} = Q_{\infty 0}^i - Q_0^{ie} + \frac{1}{N_0}\frac{dN_0}{dt}E_0^i + W_0^i - p_0^i L_a L_b \frac{dZ_0}{dt}. \tag{5.25}$$

Reciprocally, the change in energy content of the background plasma inside DV is given as

$$\frac{dE_\infty^e}{dt} = -Q_{\infty 0}^e + Q_\infty^{ie} - \frac{1}{N_0}\frac{dN_0}{dt}E_0^e + W_\infty^e + p_\infty^e L_a L_b \frac{dZ_0}{dt} + \frac{1}{2}\frac{n_\infty(\rho_M)k_B T_\infty^e(\rho_M)}{\gamma - 1}\left|\frac{d\rho_M}{dt}\right|\left(\frac{dV}{d\rho}\right)_{\rho_M}, \tag{5.26}$$

$$\frac{dE_\infty^i}{dt} = -Q_{\infty 0}^i - Q_\infty^{ie} - \frac{1}{N_0}\frac{dN_0}{dt}E_0^i + W_\infty^i + p_\infty^i L_a L_b \frac{dZ_0}{dt} + \frac{1}{2}\frac{n_\infty(\rho_M)k_B T_\infty^i(\rho_M)}{\gamma - 1}\left|\frac{d\rho_M}{dt}\right|\left(\frac{dV}{d\rho}\right)_{\rho_M}, \tag{5.27}$$

with a complementary term $\infty\ |d\rho_M/dt|$ accounting for the increase in ΔV. dZ_0/dt can be determined by an equation for the acceleration of the longitudinal plasmoid size,

$$\frac{d^2 Z_0}{dt^2} = \frac{\xi}{M_{eff}}\left[-\frac{1}{2\xi}\frac{dM_{eff}}{dt}\frac{dZ_0}{dt} + L_a L_b\left(p_0^e + p_0^i - p_\infty^e - p_\infty^i\right) - \frac{W_0^e + W_0^i + W_\infty^e + W_\infty^i}{dZ_0/dt}\right], \tag{5.28}$$

which is derived from the total energy balance in local plasmoid geometry for the open system of all particles inside ΔV (neglecting radial particle diffusion):

$$\frac{1}{2}\frac{n_\infty k_B\left(T_\infty^e+T_\infty^i\right)}{\gamma-1}\bigg|_{\rho_M}\left|\frac{d\rho_M}{dt}\right|\left(\frac{dV}{d\rho}\right)_{\rho_M}=\sum E_{0/\infty}^{e/i}+\frac{1}{2}\frac{m_0^iN_0+m_\infty^iN_\infty}{M_{eff}\,\Delta V}\iiint\limits_{\Delta V}m_{0/\infty}^i n_{0/\infty}\left(u^i(\vec{x})-u_D\right)^2dV$$
$$\sim\sum E_{0/\infty}^{e/i}+\frac{M_{eff}}{2Z_0}\int_0^{Z_0}\left(u^i(z)\right)^2dz\sim E_0^e+E_0^i+E_\infty^e+E_\infty^i+M_{eff}\;\frac{1}{2\xi}\left(\frac{dZ_0}{dt}\right)^2,\xi\sim 3. \tag{5.29}$$

M_{eff} is the effective mass in motion, comprising the mass of the plasmoid, $m^i_0N_0$ =, and that from particles of the surrounding background plasma that are pushed or dragged by the expanding plasmoid. Its time derivative can be estimated as

$$\frac{dM_{eff}}{dt}=\frac{m_\infty^iN_\infty}{L_\phi-Z_0}\left[C_{s\infty}+\frac{1}{L_b}\left(Z_0\frac{dL_{\eta\infty}}{dt}+L_{\eta\infty}\frac{dZ_0}{dt}\right)\right]. \tag{5.30}$$

With (5.28), a second derivative is introduced into the model, making its numerical treatment more delicate. Neglecting viscosity and variations in M_{eff}, $T_0^{e}/_{\infty}^{i}$, $N_{0/\infty}$, and L_ϕ, (5.28) can be reduced to a non-linear differential equation of the type $f\times df^2/dt^2 + C_1\,f + C_2 = 0$, with the approximate asymptotic oscillatory solution

$$Z_0\approx\frac{N_0\left(T_0^e+T_0^i\right)L_\phi}{N_\infty\left(T_\infty^e+T_\infty^i\right)}+\lambda_1\cdot\sin\left(\frac{1}{L_\phi}\sqrt{\frac{k_BN_\infty^2\left(T_\infty^e+T_\infty^i\right)^2}{N_0\left(T_0^e+T_0^i\right)M_{eff}}}\cdot t+\lambda_2\right),$$
$$\lambda_1,\lambda_2\in\mathbb{R},\quad\left|\frac{\lambda_1}{L_\phi}\right|<\frac{N_0\left(T_0^e+T_0^i\right)}{N_\infty\left(T_\infty^e+T_\infty^i\right)}. \tag{5.31}$$

Even with a comparably low oscillation frequency of $<10^4$Hz, $dZ_0\,dt$ can become negative during the homogenisation process according to (5.31). In principle, the viscous terms in (5.28) should damp the parallel plasmoid expansion process such that it asymptotically stops, when pressure equilibration is reached. However, as $\delta Z_0\,dt$ is in the denominator of the last term in (5.28), the deceleration caused by viscosity can become very strong for a very short time, and oscillatory artefacts in the evolution of Z_0 can appear due to difficulties in the numerical treatment. With the terms related to viscosity, one also introduces some inaccuracies into the system: At the beginning of the homogenisation process, the condition $\Omega_{0/\infty}^{e/i}\tau_{0/\infty}^{e/i}>>1$is not fulfilled for plasmoid ions. The corresponding viscosity coefficients might then not be correct [43]. According to (5.8), $L_{\eta0/\infty}=0$ at $t=0$. It seems more natural to start the development of the gradient lengths already at the beginning of the plasmoid ionisation process, giving $L_{\eta0/\infty}(t=0)=(t_{ini}\,\pi\eta^i_{20/\infty}/n_{0/\infty}\,m^i_{0/\infty})$, with t_{ini} for the time between the formation and release of the plasmoid cloud, but obviously, this is just a rough estimate. With the question of proper initialisation, an additional incertitude is introduced in the initial homogenisation phase, which diminishes with$\sqrt{\quad t^{-1}}$. (The same is true for L_{n0}, whereas

the problem is less relevant for $L_{\parallel}{}^{e/i}{}_{\perp 0/\infty}$, because the gradient lengths for thermal conductivities are only used in relation to each other.) Also, it is difficult to validate the chosen theoretical description for all viscosity effects. It might therefore be useful to introduce a simpler empirical treatment of the longitudinal plasmoid expansion process. For the beginning of the homogenisation process, the approximation $dZ_0/dt \sim Cs_0$ can be applied, being in conformance with experimental measurements [44]. This helps to avoid possible inaccuracies in the initial homogenisation phase as mentioned before. For the later phase, the decrease in the expansion speed can be derived from the force balance equation

$$M_{eff}\frac{d^2Z_0}{dt^2}+\eta\frac{dZ_0}{dt}=\Delta p L_a L_b\,, \tag{5.32}$$

with a frictional term proportional to dZ_0/dt. If one assumes for a plasmoid with long parallel elongation that the friction becomes dominant, i.e. $M_{eff}\,d^2Z_0/dt^2 < \Delta p L_a L_b - \eta dZ_0/dt$, one obtains, η chosen such that the strongest of all viscous dissipation effects is considered and averaged for the interface region between the plasmoid and the background plasma,

$$\frac{dZ_0}{dt}=\min\left(C_{s0},\frac{\left(p_0^e+p_0^i-p_\infty^e-p_\infty^i\right)L_b\left(L_{\eta\infty}+L_{\eta 0}\right)}{2Z_0\left(\eta_{20}^i+\eta_{2\infty}^i\right)}\right) \tag{5.33}$$

for the evolution of dZ_0/dt during the whole homogenisation process.

As the transfer from kinetic to thermal energy is mainly done by the work of the expanding plasmoid at the beginning of the homogenisation, and since it is small compared to the inner energy of both the plasmoid and the background plasma later on, it is possible to omit $W_{0/\infty}^{e/i}$ in (5.24-27) in typical conditions without considerable loss of accuracy, if (5.33) is used instead of (5.28).

The plasmoid barycentre ρ_M as defined in [4] can roughly be reproduced by integration of

$$\frac{d\rho_M}{dt}=(\nabla\rho\cdot\vec{u}_D)\frac{\sqrt{2\rho_M^2-(\rho_M(t=0))^2}}{2\rho_M}\frac{\operatorname{sgn}s_D+1}{2},\quad s_D=\int_0^t u_D dt', \tag{5.34}$$

with the minor radius flux surface label ρ, ignoring the initial plasmoid extension and a possible dilatation of the plasmoid cloud for $u_D < 0$ right after the release of the plasmoid from a pellet injected towards the HFS. If ρ_M is interpreted as the average position in terms of r for all plasmoid particles that have not been diffused and covered the full distance s_D at a time t (see figure 22), it can be analytically expressed as

$$\vec{P}(s)=\vec{P}(0)+\int_0^s \hat{e}_\zeta\times\frac{\nabla\rho\left(\vec{P}(s')\right)}{\left|\nabla\rho\left(\vec{P}(s')\right)\right|}ds',$$

$$\vec{P}_{cen}=\lim_{s\to\infty}\left(\frac{1}{s}\int_0^s\vec{P}(s')ds'\right),\quad \alpha(s)=\arccos\left(\frac{\vec{P}(0)-\vec{P}_{cen}}{\left|\vec{P}(0)-\vec{P}_{cen}\right|}\cdot\frac{\vec{P}(s)-\vec{P}_{cen}}{\left|\vec{P}(s)-\vec{P}_{cen}\right|}\right),$$

$$\sim \sqrt{\frac{1+\kappa^2}{2}}\,\frac{\rho_M(t=0)}{qR_0}, \tag{5.35}$$

$$\rho_M(t)=\frac{1}{2Z_0(t)}\int_{-Z_0(t)}^{Z_0(t)}\rho\left(\vec{P}\left(zZ_{proj}\right)+\vec{s}_D(t)\right)dz.$$

$\vec{P}(0)$ is the position vector of the barycentre for the plasmoid cloud when it is released from the pellet, $\hat{e}_\zeta$ is a unit vector pointing into the toroidal direction, and κ stands for the ellipticity of the flux surface, where the plasmoid is initially situated. The time derivative of ρ_M depends on s_D and Z_0

$$\frac{d\rho_M}{dt}=\frac{d\rho_M}{ds_D}\frac{ds_D}{dt}+\frac{d\rho_M}{dZ_0}\frac{dZ_0}{dt}$$

$$=\frac{1}{2Z_0}\left[\vec{u}_D\cdot\int_{-Z_0}^{Z_0}\nabla\rho\left(\vec{P}\left(zZ_{proj}\right)+\vec{s}_D\right)dz+\frac{dZ_0}{dt}\left(\sum_{s=\pm Z_0 Z_{proj}}\rho\left(\vec{P}(s)+\vec{s}_D\right)-2\rho_M\right)\right]. \tag{5.36}$$

It should be noted that the scheme for the calculation of the plasmoid barycentre as described by equations (5.34-36) only applies to axisymmetric plasma configurations with a dominant toroidal magnetic field component as e.g. in tokamaks. For the determination of the position of the plasmoid in other plasma and field geometries as e.g. in stellarators and RFPs, a more elaborated scheme needs to be used. A brief summary of peculiarities in the calculation method that is applied by the HPI2 code for the prediction of pellet ablation and deposition in non-tokamak magnetic field configurations is presented together with some exemplary simulation cases in Subsection 7.2.4.

5.2.1. Power transfer from fast ions to the plasmoid.

In the case of pellet injections into a target plasma with a noticeable population of high-energetic ions (e.g. if strong auxiliary heating by neutral beams is applied), not only the ablation process may be affected by the direct interaction with the fast ion flow but also the homogenisation process. The energy that is deposited in the plasmoid region by the non-thermalised nuclei can enhance the plasmoid pressure and cause an increase in the drift velocity. One therefore needs to take an additional energy source due to the fast ions into consideration in the energy balance equations by introduction of an additional term Q^e_{f0} in (5.24), which will be derived hereafter:

Let us consider multiple monoenergetic beams with different pitch angles, E_{fn}, q_{fn}, n = 1,...,N, for the representation of arbitrary fast ion distribution functions. If the velocity of fast ions is much larger than the velocity of the plasmoid cloud electrons ($v_{fn} > v_0^e = \sqrt{2T_0^e/m^e}$), the slowing down of fast ions is given by [45]:

$$\frac{1}{v_{fn}}\frac{dE_{fn}}{dt}=-\frac{Z_f^2 q_i^4 \ln\Lambda}{8\pi\varepsilon_0^2}\left(\frac{m_f^i n_0^i Z_0^i}{m_0^i}+\frac{m_f^i n_0^e}{m^e}\right)\frac{1}{E_{fn}}, \tag{5.37}$$

with $v_{fn}=\sqrt{2E_{fn}^e/m_f^i}$ for the velocity of the fast ions, imf for their mass, Z f for their charge number and Z_i^0 for the charge number of the plasmoid ions. The first and second terms on the right-hand

side of equation (5.37) represent the contributions to the heating of the plasmoid cloud ions and electrons resp.. As the heating term for electrons exceeds that for ions by several orders of magnitude ($\sim m^i_0/ Z^i_0 m^e$), the latter can be neglected. For fast ions with a velocity v_{fn} in a range $0.5v^e_0 > v_{fn} > 3v^i_0$, $v^i_0 = \sqrt{2T^i_0/m^i_0}$, one has [45]

$$\frac{1}{v_{fn}}\frac{dE_{fn}}{dt} = -\frac{Z_f^2 q_i^4 \ln\Lambda}{8\pi\varepsilon_0^2}\left(\frac{m_f^i}{E_{fn}}\frac{n_0^i Z_0^i}{m_0^i} + \frac{4n_0^e}{3\sqrt{\pi}}\sqrt{\frac{m_f^i}{m^e}}\frac{\sqrt{E_{fn}}}{\left(T_0^e\right)^{3/2}}\right). \tag{5.38}$$

Also in this case, one can reasonably assume that the fast ion energy exceeds by far the critical energy of the plasmoid cloud, $E_{C0} \sim 14T^e_0$, for the main portion of the fast ion distribution function. Consequently, the contribution of fast ions to the plasmoid heating appears only as a heat source term in the energy balance equation for the plasmoid electrons. Neglecting the ion heating term in equations (5.37-38), one obtains

$$v_{fn} > \xi v_0^e : \frac{1}{v_{fn}}\frac{dE_{fn}}{dt} = \frac{dE_{fn}}{dl} \cong -\frac{n_0^e Z_f^2 q_i^4 \ln\Lambda}{8\pi\varepsilon_0^2}\frac{m_f^i}{m^e}\frac{1}{E_{fn}} := -\frac{\beta_1}{E_{fn}}, \tag{5.39}$$

$$v_{fn} < \xi v_0^e : \frac{1}{v_{fn}}\frac{dE_{fn}}{dt} = \frac{dE_{fn}}{dl} \cong -\frac{Z_f^2 q_i^4 \ln\Lambda}{8\pi\varepsilon_0^2}\left(\frac{4n_0^e}{3\sqrt{\pi}}\sqrt{\frac{m_f^i}{m^e}}\frac{\sqrt{E_{fn}}}{\left(T_0^e\right)^{3/2}}\right) := -\beta_2\sqrt{E_{fn}}, \tag{5.40}$$

where $\xi = 1.5$ (For simplicity, no smooth transition between equations (5.39-40) is assumed close to $v_{fn} = \xi v_0^e$. With $\xi = 1.5$ the transition takes place at a velocity v_{fn} for which the energy exchange between the fast ions and the cloud becomes most efficient [45] in the limit of m^e/m^i_0 vanishing.). The cut-off energy of the plasmoid is given by

$$\begin{aligned} v_{fn} > \xi v_0^e &: \int_0^{E_{C1}} E dE = \int \beta_1 dl \rightarrow E_{C1} = \sqrt{2\int \beta_1 dl}, \\ v_{fn} < \xi v_0^e &: \int_0^{E_{C2}} \frac{dE}{\sqrt{E}} = \int \beta_2 dl \rightarrow E_{C2} = \frac{1}{4}\left(\int \beta_2 dl\right)^2. \end{aligned} \tag{5.41}$$

Following the scheme in [7] for the consideration of geometric corrections due to the sizeable Larmor radius of the fast ions (see also Subsubsection 2.2.2 for a description of geometry-related quantities used below), the line integral in (5.41) can be expressed as

$$\int dl \rightarrow \tilde{X}_{fn} Z_0, \tilde{X}_{e/i} = \frac{2}{\left(1+\tilde{\omega}x_{e/i}\right)^2}\int_0^{1+\tilde{\omega}x_{e/i}} \frac{\alpha'}{\pi}\frac{L}{\sqrt{1-\tilde{\omega}^2}} z dz. \tag{5.42}$$

The fast ion energy deposited in the plasmoid ΔE_{fn} is then given by

$$\begin{aligned} &v_{fn} > \xi v_0^e, E_{fn} > E_{C1} : \Delta E_{fn} = E_{fn} - \sqrt{E_{fn}^2 - 2\tilde{X}_{fn} Z_0 \beta_1}, \\ &v_{fn} > \xi v_0^e, E_{fn} < E_{C1} : \Delta E_{fn} = E_{fn}, \\ &v_{fn} < \xi v_0^e, E_{fn} > E_{C2} : \Delta E_{fn} = E_{fn} - \left(\sqrt{E_{fn}} - \frac{1}{2}\tilde{X}_{fn} Z_0 \beta_2\right)^2, \\ &v_{fn} < \xi v_0^e, E_{fn} < E_{C2} : \Delta E_{fn} = E_{fn}. \end{aligned} \tag{5.43}$$

with the cut-off energies

$$E_{C1n} = \sqrt{2\tilde{X}_{fn} Z_0 \beta_1}\,,\; E_{C2n} = \frac{1}{4}\left(\tilde{X}_{fn} Z_0 \beta_2\right)^2. \tag{5.44}$$

Finally, the fast ion heat source term can be formulated as a sum over all components of the fast ion distribution function,

$$Q^e_{f0} = \sum_n \tilde{\Pi}_{fn} L_a L_b n^i_{fn} v_{fn} \Delta E_{fn}. \tag{5.45}$$

The energy balance equation for electrons then reads:

$$\frac{dE^e_0}{dt} = Q^e_{\infty 0} + Q^e_{f0} + Q^{ie}_0 + \frac{1}{N_0}\frac{dN_0}{dt} E^e_0 + W^e_0 - p^e_0 L_a L_b \frac{dZ_0}{dt}. \tag{5.46}$$

If the plasmoid homogenisation time is smaller than the fast ion thermalisation time in the background plasma in quasi-steady state conditions, fast ion energy sources are much smaller than Q^e_{f0} and can be neglected in an energy balance equation for fast ions, which could then be simply defined as

$$\frac{dE_f}{dt} = -Q^e_{f0} - p^i_f L_a L_b \frac{dZ_0}{dt}. \tag{5.47}$$

For simplicity, it can be assumed that $E_{fn}(t) \sim E_{fn}(t=0) \times E_f(t)\; E_f(t=0)$. If the fast ion energy reservoir does not get refilled within the time scale of the plasmoid homogenisation, the heating of fast ions is most relevant for the plasmoid pressure evolution and thus the drift acceleration in the initial expansion phase when the plasmoid density and the fast ion energy are at their maximum level.

6. MODEL REFORMULATION FOR NUMERICAL IMPLEMENTATION

With exception of external functions for the determination of derivatives of the plasmoid barycentre with respect to the drift displacement s_D and the plasmoid length Z_0, $d\rho_M\, ds_D$, and $d\rho_M\, dZ_0$, the complete model describing the plasmoid cloud dynamics, including the drift equation derived in Section 4, can now be summarised as a concise system of 29 (partially stiff) differential equations of the form $d\vec{y} = \vec{f}(\vec{y}, d\vec{y}/dt, t)\, dt$ that can be solved by standard numerical routines:

$$\begin{aligned}
\vec{y} = \Big[& s_D, \rho_M, N_0, N_\infty, Z_0, \sigma_s, L^{e/i}_{\parallel/\perp 0/\infty}, L_{\eta 0/\infty}, L_{n_0}, \\
& L_a, L_b, L_\phi, E^e_0, E^i_0, E^e_\infty, E^i_\infty, E_f, L_{J\phi}, \mathrm{T}, m^i_\infty, u_D \Big]^T, \\
\vec{f}(\vec{y}, d\vec{y}/dt, t) = \Bigg[& u_D, \quad \frac{d\rho_M}{ds_D}\frac{ds_D}{dt} + \frac{d\rho_M}{dZ_0}\frac{dZ_0}{dt}, \\
-2 \cdot \frac{n_0 - n_\infty}{L_{n_0}} D_0 Z_0 (L_a + L_b), & \quad 2 \cdot \frac{n_0 - n_\infty}{L_{n_0}} D_0 Z_0 L_a + \frac{1}{2} n_\infty(\rho) \left(\frac{dV}{d\rho}\right)_{\rho_M} \cdot \left|\frac{d\rho_M}{dt}\right|, \\
& \min\left(C_{s0}, \frac{\left(p^e_0 + p^i_0 - p^e_\infty - p^i_\infty\right) L_b \left(L_{\eta\infty} + L_{\eta 0}\right)}{2 Z_0 \left(\eta^i_{20} + \eta^i_{2\infty}\right)} \right), \\
& \left(-\frac{\sigma_s}{Z_0} + \sqrt{\frac{1}{Z_0^2} + \frac{1}{L_s^2}} \right) \cdot \frac{dZ_0}{dt}, \Bigg]
\end{aligned} \tag{6.1}$$

$$
\begin{aligned}
&\frac{\pi\kappa^{e/i}_{\parallel/\perp\,0/\infty}}{2n_{0/\infty}L^{e/i}_{\parallel/\perp\,0/\infty}},\quad \frac{\pi\eta^{i}_{2\,0/\infty}}{2n_{0/\infty}m^{i}_{0/\infty}L_{\eta\,0/\infty}},\quad \frac{\pi D_0}{2L_{n_0}},\\
&L_{a\,\mathrm{ini}}\frac{d\sigma_s}{dt}+\left|\frac{d\rho_M}{dt}\right|,\quad -L_{a\,\mathrm{ini}}\frac{d\sigma_s}{dt}\frac{L_b}{L_a},\quad \left|\frac{d\rho_M}{dt}\right|\left(\frac{2\pi^2R_0}{L_b}\frac{\rho_M}{L_a}-\frac{L_\phi}{L_a}\right),\\
&Q^e_{\infty 0}+Q^e_{f0}+Q^{ie}_0+\frac{1}{N_0}\frac{dN_0}{dt}E^e_0-p^e_0L_aL_b\frac{dZ_0}{dt},\quad Q^i_{\infty 0}-Q^{ie}_0+\frac{1}{N_0}\frac{dN_0}{dt}E^i_0-p^i_0L_aL_b\frac{dZ_0}{dt},\\
&-Q^e_{\infty 0}+Q^{ie}_{\infty}-\frac{1}{N_0}\frac{dN_0}{dt}E^e_0+p^e_{\infty}L_aL_b\frac{dZ_0}{dt}+\frac{1}{2}\frac{n_\infty(\rho_M)k_BT^e_\infty(\rho_M)}{\gamma-1}\left|\frac{d\rho_M}{dt}\right|\left(\frac{dV}{d\rho}\right)_{\rho_M},\\
&-Q^i_{\infty 0}-Q^{ie}_{\infty}-\frac{1}{N_0}\frac{dN_0}{dt}E^i_0+p^i_{\infty}L_aL_b\frac{dZ_0}{dt}+\frac{1}{2}\frac{n_\infty(\rho_M)k_BT^i_\infty(\rho_M)}{\gamma-1}\left|\frac{d\rho_M}{dt}\right|\left(\frac{dV}{d\rho}\right)_{\rho_M},\\
&-Q^e_{f0}-p^i_fL_aL_b\frac{dZ_0}{dt}\\
&2\frac{4\pi}{\mu_0}\frac{1}{\sigma_{\parallel\infty}L_{J\phi}}\frac{1}{1+e^{-\lambda_1\left(L_b/2-L_{J\phi}\right)}},\quad -\frac{1}{\tau^e_\infty+\hat\tau_L}\mathrm{T}\frac{1}{1+e^{-\lambda_2\left(t-\tau_{con}\right)}},\\
&\frac{dN_0}{dt}\frac{1}{N_\infty}\left(m^i_\infty-m^i_0\right),\\
&\frac{2N_0\left(p^i_0+p^e_0+n_0m^i_0(dZ_0/dt)^2/2\xi-p^i_\infty-p^e_\infty\right)}{n_0RM_{0,Lcon2}}\cdot\cos\left(\frac{Z_0}{R_0q}\right)\cdot\left(\mathrm{sgn}\left(\frac{\pi R_0q}{2}-Z_0\right)+1\right)\\
&-\frac{u_D}{M_{0,Lcon2}}\left(\frac{2(1-P_{con}-P_{con2})B^2_\parallel L_aL_b}{\mu_0v_A}+\frac{P_{con}\sigma_{\parallel\infty}B^2_\parallel L_aL^2_bL_{J\phi}}{(L_{conH}-Z_0)}(1-\mathrm{T})\right)\Bigg]^T.
\end{aligned}
\tag{6.2}
$$

All drift damping terms and the additional drift acceleration caused by dZ_0/dt are taken into account in the equation for du_D/dt . To facilitate the computation of the Heaviside function and the integral in the Pégourié term of the drift equation, the quantity

$$
\mathrm{T}\approx\Theta\left(t-\tau_{con}\right)\cdot e^{-\int_{\tau_{con}}^{t}dt'/\tau^e_\infty(t')+\hat\tau_L},
\tag{6.3}
$$

has been introduced. l1 and l 2 are constants that have to be defined such that a sharp but numerically treatable transition from dLJf dt ¹ 0 to zero derivatives at t | Lb (t)< 2LJf (t) resp. from dT dt = 0 to non-zero values at t >t con is obtained. In practice, the figures l1 =1000 and 5l 2 = 3×10 should give satisfying results in usual plasmoid homogenisation conditions. With the proposed order of quantities in the vectors (6.1) resp. (6.2), all required time derivatives in (6.2) are defined before they are used in other terms. That way, all input values can be taken from the current iteration step in an ordinary differential equation solver, thus helping to improve the numerical convergence of the algorithm.

7. THE HYDROGEN PELLET INJECTION CODE HPI2

7.1. OVERVIEW AND FEATURES

A hydrogen pellet injection code called HPI2 for the calculation of the pellet particle source, the change in plasma density and temperature after pellet injection, taking into account a pellet ablation model as summarised in Section 2 and an E×B drift model similar to the description given in (6.1-2), has been developed. Following the pellet on its injection path, the ablation and homogenisation processes are calculated for a representative subset of plasmoids to determine the local pellet ablation rate and drift displacement. In an iterative manner, the locally ablated and drifted pellet particles are deposited in the background plasma, and the plasma density and temperature profiles are updated accordingly. That way, the influence of previously deposited particles on the particle deposition behaviour, i.e. the pellet pre-cooling effect, which is particularly important in the case of massive, deeply penetrating pellet injections at low speed from the HFS, can be allowed for.

The pellet code can be run as stand-alone application for the analysis of pellet ablation profiles (without consideration of the E×B drift, as typically measured in the experiment by Ha line radiation) and pellet deposition profiles (net local increase in density after pellet injection, including the E×B drift effect), and the corresponding immediate change in plasma conditions. In combination with a plasma transport code, it can be applied in fully predictive simulations of pellet-fuelled plasmas, as for example in dedicated studies focussing on the evaluation of pellet fuelling schemes, efficiencies, and dependencies, and the change in particle transport behaviour right after pellet injection. HPI2 is an integral part of the CRONOS transport code suite [46], and it is fully coupled to the set of JET integrated transport codes JINTRAC [47]. It is unique in the sense that it combines a number of features that are only selectively available in other comparable pellet source codes:

- High versatility: applicability to any pellet injection and target plasma configurations, for various hydrogen isotopic pellet material compositions.
- Treatment of the exact 2D magnetic flux surface geometry in the calculation of the pellet injection path.
- Inflected pellet trajectories induced by the pellet rocket acceleration effect are accounted for.
- Full Maxwellian description for incident electrons in the ablation process.
- Adequate treatment of the impact of the electrostatic sheath on incident particles, the shielding of the pellet material by the partly ionised plasmoid and the neutral cloud, as well as the interplay between those regions during pellet ablation.
- Consideration of fast ion fluxes, in particular the ablation enhancement caused by finite ion Larmor radius effects.
- Consideration of fast electron fluxes, in particular the ablation enhancement caused by nonstationary processes (direct heating of the pellet).
- Application of a plasmoid homogenisation model based on first-principles considerations for the plasmoid evolution and the drift displacement.

- Implementation of an additional drift acceleration term caused by the parallel plasmoid expansion as proposed by P B Parks et al..
- Implementation of the drift damping due to Alfvén wave propagation, as well as of parallel resistive currents outside and inside the plasmoid (i.e. the Pégourié resp. Rozhansky effects).
- Careful assessment of the influence of rational q flux surfaces on particle deposition.
- Consideration of the momentum transfer from the plasmoid to the background plasma in the same flux surface shell with constant non-zero electric potential as proposed by I Yu Senichenkov.
- Treatment of the 3D evolution of the plasmoid along the magnetic field lines in the real 3D magnetic flux surface geometry for the determination of the plasmoid barycentre and the average plasmoid particle drift displacement. Arbitrary magnetic field configurations, e.g. non-axisymmetric geometries as in the case of stellarators or fields with a small toroidal component as they occur in RFPs can also be dealt with.
- Optional implicit treatment of the pellet pre-cooling effect.
- Code flexibility: platform independence, batch mode compatibility, simple interfaces for the coupling with plasma transport codes, availability of data pre- and post-processing and visualisation tools.

7.2. EXEMPLARY SIMULATION RESULTS

In the following, exemplary HPI2 simulation results for the validation of the plasmoid homogenisation model, the derivation of a scaling law for the E×B drift, and an analysis of the pellet rocket acceleration effect are presented.

7.2.1. Validation of the drift model. First comprehensive efforts to validate the plasmoid homogenisation model used in HPI2 were presented in [48]. Measurement data from pellet injections in various tokamaks with different plasma conditions and pellet injection directions have been collected. The measured pellet drift was obtained by evaluation of the barycentres of the ablation and deposition profiles and compared with the output from HPI2 simulations. Some results are shown in table 3. In principle, most of the predicted (pellet-averaged) drift displacements lie within the error range of the measurement. The observed trends for the particle drift in the experiment appear to be reproducible. However, the error is often in the same order of magnitude as the measured drift displacement itself. Therefore, the validation of the homogenisation model should be continued with new high-resolution measurement data.

At JET, promising experiments with improved diagnostic systems, e.g. for Thomson scattering, have recently been carried out. For some representative pellet injection cases presented in [49], HPI2 has been run to find out if the increase in density measured by a new high resolution LIDAR diagnostics system fits with the predicted deposition profile. Thanks to an increase in the LIDAR measurement frequency from 5 to 20Hz, post-pellet density and temperature profiles could be

measured with considerably reduced average time delay with respect to the pellet ablation time (25 ms instead of 125 ms) and thus reduced perturbation due to diffusive effects as described in the statistical analysis presented in Section 3. Results are shown in figure 23 for pellet injections from the LFS into an Lmode plasma resp. from the VHFS into a hybrid mode plasma with a particularly small time delay for the LIDAR post-pellet profile measurement of < 10ms. The pellets consist of ~8×10^{20} deuterium atoms, their injection velocity is v_p =190m/s resp. 155m/s . The electron density and temperature on the magnetic axis are n_0 ~2×10^{19} m^{-3}, T_0 ~ 2keV and n_0 ~6×10^{19} m^{-3}, T_0 ~ 5keV resp.. The measured pellet particle deposition profile could well be reproduced in these two cases. The average drift displacement of a pellet particle determined by HPI2 is 10 cm resp. 13 cm in terms of minor radius flux surface coordinates ρ for the L-mode resp. hybrid mode pellet injection case. Due to the lower plasma pressure, the ablation rate and the plasmoid pressure are reduced in L-mode, leading to a reduced drift in the first example despite the fact that in contrast to injections from the VHFS, the pellet injection trajectory and the direction of the drift displacement are well aligned with the normal of the magnetic flux surfaces for injections from the LFS at JET, which causes a deeper pellet penetration and a higher net drift in terms of ρ. In these HPI2 simulations, the pellet pre-cooling effect was not taken into account, as it has turned out to be overestimated in many situations, which might be explained by differences between the mean position of temperature and density equilibration between a plasmoid and the background plasma in the homogenisation phase by reason of shorter time scales for the heat transfer from the plasma to the plasmoid compared to the plasmoid expansion process. In the current HPI2 version, the plasma temperature is assumed to decrease at the position where the pellet particles are deposited in the background plasma in the construction of updated background plasma profiles.

7.2.2. Scaling law for the pellet-averaged particle drift.

Least squares fits were carried out for the determination of the main parameter dependencies on the pellet-averaged particle drift displacement based on ~800 HPI2 simulations for statistically representative sets of injection and plasma target conditions in the vicinity of typical tokamak configurations (~ ±40% of standard parameter settings). [48] An equation has been derived for the rough estimation of the absolute average drift displacement in terms of ρ:

$$\Delta_{\mathrm{Drift}} = C_1 \left(\frac{v_p}{100}\right)^{C_2} r_p^{C_3}\, n_{e0}^{C_4}\, T_{e0}^{C_5} \left(\left|\alpha\right| - C_6\right| + C_8\Big)^{C_7} (1-\Lambda)^{C_9}\, a_0^{C_{10}}\, R_0^{C_{11}}\, B_0^{C_{12}}\, \kappa^{C_{13}}\,, \qquad (7.1)$$

with vp defined in m/s, rp in mm, the axial electron density n_{e0} and temperature T_{e0} in 10^{19} m^{-3} and keV resp., the pellet injection angle with respect to the horizontal outward direction a given in the range $[-\pi, \pi]$, the impact parameter of the pellet trajectory Λ (i.e. the distance between the positions of the magnetic axis and the tangent point of the pellet trajectory line with the flux surfaces) described in terms of normalised ρ coordinates, the tokamak minor and major radii a_0 and R_0 in m, and thetoroidal field strength B_0 in T. κ is the plasma elongation close to the separatrix. Since the rational q

flux surface effect on the drift behaviour has a complex local structure, it cannot be satisfactorily integrated into a simple scaling law. Therefore, its influence was statistically cancelled in the simulations by strong arbitrary variations of the q-profile for each run ($q(\rho = a_0) \in [3,9]$). Only pellets that do not traverse the tangency point of the trajectory with the flux surfaces were considered to make sure that the results are not biased by overfuelling effects, and since the scaling law (7.1) is more conclusive with only n_{e0} and T_{e0} accounting for the background plasma conditions, if the local pressure is a monotonic function of the pellet penetration. Due to this restriction, (7.1) is not applicable, if the latter condition is not fulfilled. The values for the constants $C_{1\text{-}13}$ obtained by the LS fit are listed in table 4 for two different statistical input parameter distributions ($C_{1\text{-}13}$ sets Δ_1, Δ_2), together with the root-mean-square and relative errors. Results focussing on a reduced set of parameters with smaller confidence intervals for specific pellet injection lines in a specific tokamak are also given on the example of the JET LFS, HFS, and VHFS trajectories [50].

The calculated strengths of the parameter dependencies in (7.1) are in agreement with the assumptions that the drift displacement increases with the plasmoid pressure, the ablation rate, and thus the plasma pressure, and that the drift damping is mainly determined by the Pégourié effect, however, correlations between parameters, which are mainly caused by the shape of the parameter subspace of realisable pellet injection cases, must be factored in. Since more central regions with higher plasma pressure can be accessed with increasing v_p, $C_2 > 0$. C_3 is also positive in the general case, because deeper penetration is reached with bigger pellets, and the ablation rate is increased, since the effective pellet surface exposed to ablating particles is proportional to the square of the pellet radius. In the case of specific pellet trajectory lines, the E×B drift expressed in ρ can be further enhanced for faster or more voluminous pellets, if they are injected vertically, as the drift direction becomes better aligned with the flux surface gradients when the pellet penetration is sufficient to reach the horizontal plane. On the other hand, C_3 can even take on negative values for HFS injections due to pellet pre-cooling, which is more efficient, if more pellet particles are available to cool down the plasma. $C_4 > 0$ and $C_5 > 0$ account for higher ablation rates in high pressure plasmas. In figure 24, the drift dependence on v_p, r_p, n_e, and T_e for JET LFS and HFS injections is illustrated. Caution needs to be exercised in the interpretation of the $C_{2\text{-}5}$ scalings: Since big pellets at high speed can only be fully ablated in target plasmas with high energy content, v_p, r_p could be correlated with n_e, T_e, and weight could be transferred between $C_{2\text{-}3}$ and $C_{4\text{-}5}$.

$C_{6\text{-}8}$ are defined such that the absolute drift displacement in ρ has local maxima at $\alpha = \pm\pi, 0$. The influence of the impact parameter appears to be insignificant, however, only variations in L within a very small interval close to 1 were allowed in the simulations to avoid strong (positive) correlations with v_p and r_p. (7.1) should therefore not be applied to injections with pellet launchers aimed at the plasma periphery. The strong E×B drift dependency on a_0 can be explained by the average external plasmoid self-reconnection length L_ϕ, which increases with the minor radius of the flux surfaces. The Pégourié drift damping is then weakened and delayed. The same is true for the major radius, since $L_\phi \infty R0$. The Rozhansky effect is also delayed in bigger tokamaks due to the R_0

dependency of its characteristic time. However, $C_{11} < C_{10}$, because not only the drift damping but also the drift acceleration is reduced in machines with large horizontal extension: the drift driving term is indirectly proportional to the local major radius. As the drift deceleration caused by Alfvén wave dissipation and the Pégourié effect is proportional to B_0 and B^2_0 resp., $C_{12} < 0$. Finally, $C_{13} < 0$, because the pellet remains in regions with lower n_e, T_e for a longer time, if it is vertically injected into a target plasma with high elongation. Applying (7.1) with the set of constants Δ_1 to the case of the injection of a pellet with $V_p = 250$m/s, $r_p = 1.2$mm into a target plasma of ASDEX Upgrade as an example of a tokamak machine that has not been considered in the derivation of the scaling law ($n_{e0} = 4\times10^{19}$ m^{-3}, $T_{e0} = 2.2$keV, $a_0 = 0.5$m, $R_0 = 1.65$m, $B_0 = 2.5$T, $k = 1.6$ [27]), a displacement $\Delta_{Drift} \approx 10$cm is obtained for outboard launch ($\alpha = \pi$, $\Lambda = 0$) and $\Delta_{Drift} \approx 8$cm for inboard launch ($\alpha = -\pi/4$, $\Lambda = 0$), which seems to be in reasonable agreement with estimates inferred from measurement data [27]. The scaling formula gives similar values for the drift displacement for a pellet injection case in DIII-D (Vp = 150 m/s, rp = 2.7 mm, $n_{e0} = 5\times10^{19}$ m^{-3}, $T_{e0} = 3.0$keV, $a_0 = 0.61$m, $R_0 = 1.67$m, $B_0 = 2.2$T, $\kappa = 1.8$; LFS: $\alpha = \pi$, $\Lambda = 0$, HFS: $\alpha = -\pi/4$, $\Lambda = 0.1$ [3]): $\Delta_{Drift} \approx 14$cm for LFS injection, $\Delta_{Drift} \approx 12$cm for HFS injection, the relative increase compared to the ASDEX Upgrade case owing mainly to the larger size of the pellet. Examples of application of (7.1) to ITER are given in Section 8.

7.2.3. The influence of the pellet rocket acceleration effect.

The importance of the pellet rocket acceleration on the particle deposition behaviour has been analysed with HPI2 [51]. Even though similar trends are predicted for a variation in the injection configuration according to the formulae (2.14-15), a ~3–4 times higher rocket acceleration a_p is obtained by the theoretical model compared to the semi-empirical one, which is calibrated against experimental data. The results of the latter are assumed to be more trustworthy, as the former contains some parameters, as e.g. the relation a between the minimum velocity of incident electrons during ablation that can reach the pellet surface and their original thermal speed, whose values are pre-defined and may deviate from the actual ones. In the derivation of (2.14), the assumption $\alpha = 3$ was made following the examples in [28].

As shown in figure 25 for the HFS case, the rocket effect is most influential at the end of the pellet trajectory for the simple reasons that the pellet drift displacement increases with the square of the time after injection for constant ap , that the pressure is lower at the plasma edge, and since the pellet inertia decreases rapidly at the end of the ablation path. Even though the plasma temperature is the strongest acceleration enhancing parameter, the pellet lifetime is the most important determinant for the total rocket drift displacement. For this reason, the pellet rocket effect seems to be more relevant in lower pressure target plasmas as illustrated in figure 25 on the right-hand side. In ITER, it seems to be completely negligible, as the pellets are supposed to be fully ablated immediately at the plasma edge, as shown in the next subsection. Even in present day tokamaks, its role appears to be limited: In figure 26, a rough interpretative transport simulation for a JET discharge using HPI2 to calculate the pellet source with and without consideration of the rocket effect is summarised. The

predicted difference in density is limited to a few percent. Comparing the pellet injection directions, the fuelling efficiency is increased for HFS pellets, and just slightly decreased, if the plasma is fuelled from the LFS, as the smaller penetration caused by the rocket effect is partly compensated by smaller E×B drifts of the plasmoids close to the plasma boundary. Even though the pellet rocket effect appears to be comparably small, it should be systematically taken into account in pellet code validation procedures to avoid an overestimation of the E×B drift, which has a similar effect on the pellet deposition, and which can reach the same order of magnitude in ohmic low pressure experiments. In addition, the pellet rocket acceleration may need to be considered in attempts to describe an asymmetry of the efficiency of pellet triggered ELMs with respect to the pellet injection angle [52].

7.2.4. Comparison of deposition profiles for pellet injection in comparable stellarator / RFP / tokamak conditions.

A comparison has been made for the particle deposition behaviour as predicted with HPI2 for pellet injections in stellarator, RFP and tokamak target plasmas assuming similar conditions for the background plasma and pellet injection configurations. That way, variations in the simulated plasmoid drift displacement can mainly be attributed to the differences of the magnetic field configuration.

To allow for the treatment of stellarator and RFP magnetic field configurations that are nonaxisymmetric or that are dominated by the poloidal magnetic field component resp., an advanced calculation scheme with the following differences in the simulation assumptions compared to those for conventional simulations of pellet ablation and deposition in tokamaks needs to be considered (see [8,36] for further details with respect to stellarators):

- Usage of the general drift equation on basis of (4.10) instead of (4.8) (including a drift damping term $\propto u_D$ accounting for Alfvénic and Pégourié currents and considering the momentum transfer from the plasmoid to the background plasma).· Due to strong possible variations in the magnetic field and its gradient along the field lines, the quantities $|\vec{B}|$, $|\vec{B}|^2$,$\nabla |\vec{B}|$ at the plasmoid centre position are replaced by $\langle|\vec{B}|\rangle$, $\langle|\vec{B}|^2\rangle$,$\langle\vec{\nabla} |B|\rangle$ (with $\langle ... \rangle$ for the average over the plasmoid length) wherever appropriate in both ablation and homogenisation routines.
- Since q can reach very low values in an RFP configuration, one needs to consider the possibility that external plasmoid current reconnections can occur in the poloidal direction at a much earlier time compared to that required for the establishment of a toroidal reconnection. For that reason, the calculation of P_{con} and L_{con} as given in (4.42-43) must be adapted accordingly for RFP plasmas. In HPI2, this is done numerically via field-line tracing techniques.
- For tokamaks, equations (5.34-36) are used to determine the movement of the plasmoid barycentre, but the possibility for a small vertical drift displacement in addition to the main horizontal one is foreseen. The direction of the drift displacement is assumed to be the same in (R, Z) coordinates for all plasmoid particles.
- For RFPs, the plasmoid elongation is expected to remain very small compared to the magnetic

reconnection length due to very strong damping caused by the above-mentioned Pégourié currents flowing in the poloidal direction; therefore, the rotation of the electric field inside the plasmoid due to Rozhansky currents (cf. Subsection 4.2) is not taken into account; similar to the tokamak case, the plasmoid barycentre is assumed to drift in accordance with equations (5.34-36), allowing for both vertical and horizontal drift displacements in (R, Z) coordinates that are the same for all plasmoid particles.

- In the case of stellarators, the Rozhansky currents can dominate the drift damping process; therefore, the rotation of $E_\perp$ inside the plasmoid caused by the Rozhansky effect has to be considered. The direction of the drift displacement then needs to be assumed to be the same in (ρ, θ) coordinates for $\vec{a}$ll plasmoid particles, the radial and poloidal components being directly calculated by (4.10) by twofold integration of the $\partial u_D \partial t$ components. The principles depicted in (5.34-36) for the calculation of the plasmoid barycentre are kept but the calculation scheme is adapted to accommodate for a local drift displacem$\vec{e}$nt that varies in terms of (R, Z) coordinates. $d\rho_M/dt$ is then determined numerically in HPI2, although analytic approximations in equivalence to (5.34-36) could be established.

The above-mentioned differences have been taken into account in all simulation results that are presented in this subsubsection.

Hydrogen pellets with a mass of 6.25×10^{20} atoms ($r_p \sim 1.42$mm) are assumed to be injected into a hydrogen background plasma with a speed of $v_p = 3000$m/s for low field side (LFS) and $v_p = 500$m/s for high field side (HFS) injections. The ratio between the mass of the pellet and that of the background plasma is in all cases ~ 1:2. The pellet injection velocities were selected such that a pellet penetration of about two thirds of the minor radius a_0 is achieved in most cases. The plasma cross section is circular. For the stellarator, a simplified magnetic field configuration is applied with the same toroidal and poloidal pitch numbers m = 10 and n = 2 as for LHD. Both LFS and HFS injections are carried out on the horizontal mid-plane, with injection from the outer side of the machine in the first case and from the inner one in the second. Presuming that helical coils are positioned on top and bottom of the plasma column at $\Phi = 0$, the toroidal angle for LFS injection in the stellarator was selected as $\Phi = 0$, while for HFS injection, $\Phi = \pi/m$, with m for the toroidal periodicity. For all three machines, the same background plasma profile as illustrated in figure 27 is assumed. As shown in figure 28, the safety factor profile is very different in the three machines. Main parameters such as the major radius R_0 and the toroidal field strength B_0 have been selected to achieve realistic configurations corresponding to typical existing machines while assuring similar and comparable conditions for the simulations; they are summarised in table 5. The influence of fast particles on particle ablation and homogenisation is not considered.

A comparison of ablation and deposition profiles for LFS and HFS injection in the three configurations is shown in figure 29.

For the case of pellet injection in a tokamak, a drift displacement that is typical for this machine type is observed. There is a significant drift in the order of 10 to 20cm. Local maxima in the deposition profiles are caused by an enhanced drift deceleration close to the rational surfaces $q = 2$ and $q = 3$,

and, for the case of LFS injection, also close to q = 4. This is an indication that the Pégourié damping effect is more relevant in the tokamak compared to the Rozhansky effect, which only takes place at large plasmoid extension in the late phase of homogenisation when the plasmoid pressure has become very low and the drift velocity has already decreased by one or two orders of magnitude. If one compares the injections from the LFS and the HFS, a rather strong effect of pellet pre-cooling by previously ablated material can be found in the latter case, caused by the orientation of the plasmoid drift, due to which the plasma is cooled down in front of the pellet. This effect is enhanced by the lower pellet velocity. At reduced vp, the pellet stays in a region for a longer time where the background plasma pressure is already low before the injection and where the relative decrease in plasma temperature due to the cooling of deposited pellet material reaches a maximum. Therefore, the pellet ablation rate is significantly lower for the HFS injection case. Unlike in experimental observations, the drift displacement seems to be similar for both HFS and LFS injections in the tokamak configuration. Of course, these simulations are idealistic with respect to the assumption for the HFS injection direction. In real experiments, pellets have to be injected from the inboard side with some inclination with respect to the horizontal mid-plane for technical reasons. The net drift displacement measured in flux surface coordinates then naturally must be lower. However, there are other reasons why the drift is comparably strong in the case of HFS injection as well which are related to the plasmoid conditions at the time of detachment from the pellet. Expressions of the average drift displacement per pellet particle are given in table 6 for all simulation cases.

Even though the drift displacement seems to be more important in the stellarator case in figure 29, where the pellet ablation and deposition profiles are plotted as a function of normalised minor radius, it is almost the same as in the tokamak simulations in non-normalised coordinates, because a_0 is smaller. At first sight, one may expect a larger drift in stellarators due to the small curvature radius of the magnetic field lines which scale with a_0 rather than with R_0 as it is typical for tokamaks. The ∇B and curvature drift should then be larger and lead to an enhanced drift acceleration of the plasmoid clouds. This is indeed the case, however, the Rozhansky effect is also more effective in a stellarator because of the reduced magnetic reconnection length. The average drift acceleration in the plasmoid homogenisation phase may therefore be comparable with that in a tokamak. As shown for the stellarator injection case from the HFS, magnetic field configurations and pellet injection locations can be conceived for a stellarator that would permit a net inward drift of the ablated material. Apparently, this result is not in agreement with experimental observations in LHD, where an outward drift has been measured for any injection location, cf. [53]. It was found though that the existence of favourable injection configurations with an inward drift depends on details of the magnetic field structure, in particular on magnetic well / hill effects. If these are taken into consideration in HPI2, the main characteristics in LHD can be reproduced [36]. The shape of the deposition profiles in the simulations of pellet injection in a stellarator configuration does not show any sign of enhanced drift reduction close to rational surfaces, although it should be noted that the deposition profiles generally look smoother for stellarators compared to tokamaks with HPI2 due

to numeric differences in the way they are constructed. Indeed, a significant damping is achieved in the vicinity of low order rational q surfaces also in the stellarator cases (q = 1 and q = 2 in this example). The general variation of the drift displacements in correlation with the rational q surface structure appears to be a bit smaller though compared to simulations for the tokamak configuration. This could be partly explained by a different q profile which contains fewer integer rational surfaces, but mainly by a significant loss of the relative importance of the Pégourié damping with respect to the drift reduction attributed to the Rozhansky effect. In the case of LFS injection, the drift increases more quickly for plasmoids deposited further inside in the plasma in the stellarator configuration compared to the tokamak one. This behaviour may also be related to an increased importance of the Rozhansky effect, which is most effective close to the edge, giving lower drift values there, whereas the drift acceleration with comparably small internal short-circuit currents in the core region becomes even higher compared to that in the tokamak cases due to the afore-mentioned higher ∇B and curvature drift in the stellarator (although it should be mentioned that there may also be a radial dependence for the strength of the net drift acceleration that is correlated to that for the Rozhansky effect because of the correlation between the curvature radius of the magnetic field lines and the magnetic reconnection length). In the simulations of pellet injection from the HFS, the comparison between the tokamak and the stellarator is complicated by the increased influence of the pre-cooling effect.

Predictions for pellet injection in an RFP machine are much more pessimistic than those for stellarators and tokamaks. Close to the position where q = 0, the formation of external currents occurs very quickly, as it is achieved in the poloidal direction after just one poloidal turn. A bit further away from that location, the Pégourié damping becomes very weak though, as the plasmoid is just missed after one poloidal turn, the external reconnection can then only be accomplished after at least one toroidal turn that involves a very large number of poloidal rotations. Therefore, the drift displacement increases significantly with the distance to the q = 0 position. The Pégourié effect is also weaker for plasmoids that are exactly deposited on the flux surface where q vanishes, because reconnections can only take place between charges of the same sign in this case. For the case of HFS injection, the drift is negligibly small in this configuration, because the pellet is fully ablated in a region with very low q and strong poloidal Pégourié currents. For LFS injection (where vp was assumed to be 6x larger), the innermost plasmoids can already reach a drift displacement that is comparable to that in the stellarator or tokamak configuration. Because of the structure of the magnetic field, the drift in RFP is expected to be always directed to the plasma edge. As was mentioned before, the direction of the drift displacement at every local plasmoid position projected onto the poloidal plane is assumed to be constant in (R, Z) coordinates in HPI2 for RFP configurations. It may be conjectured though that it is more appropriate to apply the same scheme as for stellarators, i.e. to keep the angle of the drift direction with respect to ∇r constant at every position of the plasmoid. That way, a significant increase of the outward drift might be predicted in RFP simulations for plasmoids deposited in the core region. In RFP experiments, large displacements of the ablated pellet particles are not observed

[54], however, the plasma temperature is much lower in RFP discharges that have been realised so far compared to that assumed in the simulations for the plasma core.

7.3. FURTHER APPLICATIONS OF THE HPI2 CODE

In addition to an analysis of the pellet fuelling and particle deposition behaviour in ITER that is presented in Section 8, numerous further pellet-related modelling tasks have been successfully carried out by application of the HPI2 code. These are briefly summarised and an outlook to new modelling projects involving HPI2 that are foreseen to be carried out in the near future is given in the following.

Studies of pellet-induced ELMs at JET with the C wall [55,56] and the newly installed ITER like wall (ILW) with Be and W coating [52] have recently been performed. With the ILW, the ELM trigger efficiency seems to be noticeably degraded. The possible trigger mechanism of ELMs by pellet injection has been investigated by means of integrated core-edge simulations [57] with the TOPICS-IB [58] and JINTRAC code suites, highlighting the influence of the plasmoid drift on the pressure repartition in the edge transport barrier. Recent fuelling pellet experiments at JET have also been investigated [59]. By means of integrated modelling attempts, further clear evidence for the existence of the plasmoid drift at JET could be given even for individual pellets [60]. HPI2 has also been successfully employed for the interpretation of the pellet ablation and deposition behaviour in dedicated experiments at other tokamaks such as MAST [61], JT-60 [57] and Tore Supra [62]. Most recently, additional clear evidence could be given at Tore Supra for the existence of the plasmoid drift reduction by Pégourié currents [35]. Thanks to an extension of HPI2 developed by A Matsuyama, the code can now also be applied to the analysis of pellets injected into plasmas with arbitrary nonaxisymmetric field configurations as demonstrated in Subsubsection 7.2.4. Successful predictions of the pellet ablation and deposition profiles have already been made for the LHD stellarator [8,63,36].

Further pellet related research involving HPI2 that is envisaged for the future includes the development of a multi-machine high-precision ablation and deposition measurement database to allow an improved validation of the pellet code and thus enhance its predictability for ITER and first reactor-grade fusion engines such as DEMO, predictions for the pellet deposition behaviour in the W7-X stellarator that will soon be put into operation, deep fuelling studies for ITER, and a comparison of the fuelling efficiency in reactor-grade tokamak, stellarator and reversed field pinch prototypes. Finally, a new complementary code called PLASMO-2D for the description of the plasmoid shape evolution in the poloidal plane that is based on a model described in [64] will be used to establish refined plasmoid drift scans in dependence of local plasma environment parameters. Results and combined runs with HPI2 for an improved prediction of pellet particle deposition are planned to be presented in a follow-up paper.

8. PELLET FUELLING AND PARTICLE DEPOSITION IN ITER

The plasma fuelling in ITER will mainly rely on pellet injection. Therefore, intense efforts are

undertaken to evaluate the pellet ablation behaviour and the importance of the E×B drift in this new tokamak device based on the present level of understanding of pellet physics. [65] In line with these investigations, predictive simulations with HPI2 have been carried out for deuterium pellets corresponding to the proposed ITER standard size for fuelling purposes (cylindrical shape with side lengths of 5 mm) that are injected into an ITER baseline scenario target plasma in the burning phase with a fusion Q value close to 10 [66] along the two initially designated ITER HFS and LFS pellet tracks [67] at 300–500m/s and 3000–5000 m/s resp.. Results for the pellet ablation and deposition profiles, as well as a comparison for the predicted deposition profile for the HFS injection case with v_p = 300m/s with that obtained by other pellet codes considering the E×B drift effect [3,68] are shown in figures 30, 31.

Even though the uncertainty for the quantitative prediction of the absolute drift displacement is significant, as it is necessary to do an extrapolation to plasma conditions, for which no pellet model validation data is available at present, there are clear indications that the E×B drift is crucial to obtain sufficient pellet particle penetration in ITER. Because of the high level in plasma pressure, the pellet ablation region is concentrated to the very edge, with a penetration length of just ~10 cm measured in r for the currently foreseen maximum available pellet speed of v_p = 300-500 m/s. Only by exploitation of an inwards-directed E×B drift in HFS injections, the pellet particles can reach interior plasma regions, with an expected deposition profile barycentre in the range $\rho \in a_0 \times$ [0.8, 0.9]. According to HPI2, the average drift displacement is in the order of a few decimetres; similar values can be obtained by use of the scaling law (7.1), even though the constants $C_{1\text{-}13}$ are not fitted to typical ITER configurations: with the set of constants Δ_2 from table 4 and V_p = 300m/s, r_p = 2.8mm, $n_{e0} = 10^{20}$ m^{-3}, T_{e0} = 25 keV, a_0 = 2.0m, R_0 = 6.2m, B_0 = 5.3T, κ = 1.75, $\alpha = \pi/4$, Λ = 0.2 (HFS injection), an average drift displacement of $\Delta_{Drift} \approx$ 26cm in ρ flux coordinates is predicted. In the case of LFS-launched pellets, the drift effect is detrimental to the fuelling efficiency, as it tends to expel the pellet material from the plasma after ablation. Even if vp could be increased by a factor of 10, most of the pellet particles would either be deposited beyond $\rho = 0.9 \times a0$ or immediately leave the plasma. One can conclude that one has to rely on the E×B drift to fuel the plasma efficiently with pellets in the ITER baseline scenario. This conclusion could be confirmed in transport simulations with the pellet sources calculated by HPI2 [69]. Since the pellet material is deposited at the plasma periphery, integrated transport simulations have also been carried out with JINTRAC [47] including the scrapeoff layer to obtain a higher degree of confidence for the predicted fuelling efficiency [70]. Parameter scans for the expected range of edge barrier and particle transport conditions have also been performed [71]. The integration of pellet fuelling into the ITER scenario development for the investigation of its consequences on confinement, fuelling control and transient events such as L-H transitions and ELMs in the ITER standard scenarios has recently been started [72,73], and the modelling activity is planned to be pursued and intensified in the near future.

9. SUMMARY

A complete model for pellet ablation and deposition has been formulated, emphasising the E×B drift dynamics of the plasmoid clouds, for which experimental evidence was obtained in JET discharges. A particle drift equation has been set up, considering drift damping effects caused by Alfvén wave dissipation and short-circuit currents, whose relative importance has been evaluated. Without external plasmoid short-circuit currents taken into account, the calculated particle drift displacement is substantially increased with respect to experimental observations, as the other damping effects seem to be either too weak or too much delayed in time in tokamak configurations. The existence of these currents can be falsified by analysis of the pellet deposition profile with respect to possible dependencies on rational q surfaces. In stellarator machines, the internal short-circuit currents seem to dominate the plasmoid drift behaviour, whereas external currents with poloidal short-circuit formation appear to be relevant in RFPs.

The pellet model has been implemented in the HPI2 pellet code. First code verification results yield good agreement with experimental measurements. Depending on details of the magnetic field structure, pellet injection configurations with a favourable core-oriented plasmoid drift direction as in the case of HFS injections in tokamaks can be expected for specific stellarator concepts. In RFP machines, the drift is expected to be an order of magnitude smaller and always directed outwards. According to calculations for the ITER baseline scenario, one has to rely on the E×B drift to fuel the plasma efficiently with pellets.

ACKNOWLEDGEMENTS

This work was performed within the framework of the European Fusion Development Agreement under the contract of association between EURATOM and the Austrian Academy of Sciences. The content of this publication is in the responsibility of the authors and does not necessarily represent the views of the European Commission and its services.

Appendix A. Derivation of the drift driving term Departing from the fluid continuity equation for ions,

$$\frac{\partial n_i}{\partial t} = -\nabla \cdot \left[n_i \left(\vec{u}_{E\times B} + \vec{u}_{*i} + \vec{u}_{pi} + u_i^{\parallel} \hat{e}_{\parallel} \right) \right], \tag{A.1}$$

with the electric drift $\vec{u}_{E\times B}$, the diamagnetic drift $\vec{u}_{*i}$, and the polarisation drift upir describing thetransversal movement of the particles, and subtracting the electron equivalent for (A.1), one obtains with the approximations for quasi-neutrality and $\vec{u}_{pe} \sim 0$

$$\nabla \cdot \left[\frac{\vec{B} \times \nabla (p_i + p_e)}{q_i B_{\parallel}^2} + \frac{n_i m_i}{q_i B_{\parallel}^2} \left(\frac{\partial}{\partial t} + \vec{u}_i^{\perp} \cdot \nabla \right) \nabla_{\perp} \Phi + n_i \left(\vec{u}_i^{\parallel} - \vec{u}_e^{\parallel} \right) \hat{e}_{\parallel} \right] = 0 . \tag{A.2}$$

The divergence of the normalised diamagnetic drift momentum is proportional to the scalar product of the particle drift velocity in an inhomogeneous magnetic field ($\vec{v}_{Tj}$ …thermal velocity, Ωj… gyrofrequency, $\vec{r}_c$ …curvature vector, R…major radius),

$$\vec{u}_{\nabla Bj}=\frac{v_{Tj}^2}{\Omega_j}\left(\hat{e}_{\parallel}\times\frac{\nabla\left|\vec{B}\right|}{B_{\parallel}}\right)+\frac{v_{Tj}^2}{\Omega_j}\left(\hat{e}_{\parallel}\times\frac{-\vec{r}_c}{\left|\vec{r}_c\right|^2}\right),\quad \left|\vec{u}_{\nabla Bj}\right|=\frac{2T_j[\mathrm{J}]}{\mathrm{q_i}B_{\parallel}}\frac{1}{R}\,, \tag{A3}$$

with the pressure gradient ∇p_j:

$$\begin{aligned}\nabla\cdot\left(n_j\vec{u}_{*j}\right)&=\frac{\nabla\cdot\left(\hat{e}_{\parallel}\times\nabla p_j\right)}{q_jB_{\parallel}}-\frac{\nabla\left|\vec{B}\right|}{q_jB_{\parallel}^2}\left(\hat{e}_{\parallel}\times\nabla p_j\right)=\frac{\nabla p_j}{q_jB_{\parallel}}\left[\left(\nabla\times\hat{e}_{\parallel}\right)+\left(\hat{e}_{\parallel}\times\frac{\nabla\left|\vec{B}\right|}{B_{\parallel}}\right)\right]\\&=\frac{1}{k_BT_j}\frac{v_{Tj}^2}{\Omega_j}\left[\left(\hat{e}_{\parallel}\times\frac{-\vec{r}_c}{\left|\vec{r}_c\right|^2}\right)+\left(\hat{e}_{\parallel}\times\frac{\nabla\left|\vec{B}\right|}{B_{\parallel}}\right)\right]\cdot\nabla p_j=\frac{1}{T_j[\mathrm{J}]}\vec{u}_{\nabla Bj}\cdot\nabla p_j\,.\end{aligned} \tag{A4}$$

Thus, (A.2) can be rewritten as

$$\frac{2\nabla\left(p_i+p_e\right)\cdot\left(\vec{r}_c/\left|\vec{r}_c\right|\times\hat{e}_{\parallel}\right)}{B_{\parallel}R}+\nabla\cdot\left[\frac{n_im_i}{B_{\parallel}^2}\left(\frac{\partial}{\partial t}+\vec{u}_i^{\perp}\cdot\nabla\right)\nabla_{\perp}\Phi+\vec{j}^{\parallel}\right]=0\,. \tag{A5}$$

For a cylindrical plasmoid with roughly constant cross-sectional pressure and $Z_0 > R_p$ (Z_0… half cylinder height, R_p… cylinder radius), Laplace's equation can be applied to get an estimate for Φ both inside and outside the plasmoid as suggested in [29]. In cylindrical coordinates (r, θ , z) , with r for the distance from the plasmoid axis and the poloidal angle θ, the solution reads

$$\Phi=\begin{cases}r<R_p:C(t)r\sin\theta\\ r>R_p:C(t)R_p^2\dfrac{\sin\theta}{r}\end{cases}. \tag{A6}$$

By derivation of (A.6), the time-dependent term C(t) can be identified with the electric field inside the plasmoid:

$$\nabla\Phi\left(t,r<R_p\right)=\frac{\partial\Phi}{\partial r}\hat{e}_r+\frac{1}{r}\frac{\partial\Phi}{\partial\theta}\hat{e}_{\theta}=C(t)\left(\sin^2\theta+\cos^2\theta\right)\hat{e}_y=-\vec{E}\,. \tag{A7}$$

Integrating over a part of the plasmoid boundary in the poloidal plane with a radial depth of 2ε where the pressure gradient is non-zero, and an infinitesimal poloidal angular size of dθ, (A.5) becomes

$$\begin{aligned}&\left(\frac{m_i}{B_{\parallel}^2}\left(\frac{\partial}{\partial t}+\vec{u}_i^{\perp}\cdot\nabla\right)\left(n_i\vec{E}(t,r)\right)\right)_r\Bigg|_{r=R_p-\varepsilon}^{R_p+\varepsilon}+\int_{R_p-\varepsilon}^{R_p+\varepsilon}\frac{\partial\vec{j}^{\parallel}}{\partial z}\\&=\int_{R_p-\varepsilon}^{R_p+\varepsilon}\frac{2\left|\nabla\left(p_i+p_e\right)\cdot\hat{e}_y\right|}{B_{\parallel}R}dr=\frac{2\left(p_i+p_e-p_{i\infty}-p_{e\infty}\right)\sin\theta}{B_{\parallel}R}.\end{aligned} \tag{A8}$$

Under the assumption

$$\left[\vec{u}_i^{\perp}\right]\lesssim\left[\frac{R_p}{E}\frac{\partial E}{\partial t}\right],\quad \left|\vec{u}_i^{\perp}\right|\lesssim10^5\ \mathrm{m/s}\,, \tag{A9}$$

which is usually fulfilled in experimental conditions, some simple estimates can be derived from (A.8):

$$\left[\vec{u}_{pi}\right]<\left[\frac{T}{qBR}\right]<\left[\vec{u}_{*i}\right]=\left[\frac{T}{qBR_p}\right],\quad \left[\vec{u}_{pi}\right]=\left[\vec{u}_{E\times B}\right]\left[\frac{m_i}{qBE}\frac{\partial E}{\partial t}\right]<\left[\vec{u}_{E\times B}\right]\left[\frac{1}{B}\right]. \tag{A10}$$

It is therefore possible to omit $\vec{u}_{pi}$ with respect to the other drifts. The pressure gradient can already be neglected at the radial boundary positions of the integration volume in (A.8). It follows, that only the electric drift uE´Br has to be considered in $\vec{u}_i^{\perp}$ in the convective drift term. With (A.6) and

$$\left(\vec{u}_{E\times B}\cdot\nabla\right)\left(n_i\vec{E}(t)\right)\sim\frac{n_i}{B_\parallel}\left(\left(\hat{e}_\parallel\times\nabla_\perp\Phi\right)\cdot\nabla\right)\nabla_\perp\Phi=\frac{n_i}{B_\parallel}\begin{pmatrix}-\partial_y\Phi\partial_{xx}\Phi+\partial_x\Phi\partial_{yx}\Phi\\-\partial_y\Phi\partial_{xy}\Phi+\partial_x\Phi\partial_{yy}\Phi\end{pmatrix}, \tag{A11}$$

it is easy to verify that the convective contribution is zero for $r = R_p - \varepsilon$. For $r = R_p + \varepsilon$, it is

$$\begin{aligned}\left(\vec{u}_{E\times B}\cdot\nabla\right)\left(n_i\vec{E}(t)\right)\Big|^{r=R_p+\varepsilon}&\sim C(t)^2R_p^4\,\frac{n_i}{B_\parallel}\frac{1}{r^5}\begin{pmatrix}-4\cos^2\theta\sin\theta\\2\left(\cos^3\theta+\cos\theta\sin^2\theta\right)\end{pmatrix},\\ \left|\left(\vec{u}_{E\times B}\cdot\nabla\right)\left(n_i\vec{E}(t)\right)\right|^{r=R_p+\varepsilon}&<C(t)^2\,\frac{5\,n_i}{B_\parallel R_p}.\end{aligned} \tag{A12}$$

Compared to the time derivative of the electric field, it is of similar magnitude:

$$\left[\frac{\left|\left(\vec{u}_{E\times B}\cdot\nabla\right)\left(n_i\vec{E}(t)\right)\right|}{\left|\partial\left(n_i\vec{E}(t)\right)/\partial t\right|}\right]^{r=R_p+\varepsilon}\lesssim\left[\vec{u}_{E\times B}\right]\left[\vec{u}_i^{\perp}\right]^{-1}\lesssim 1. \tag{A13}$$

The same is true for the time derivative of the electric field at $r = R_p + \varepsilon$. However, the density of the plasmoid is usually some orders of magnitude higher than that of the background plasma. Consequently, only the time derivative inside the plasmoid needs to be kept in the first term in (A.8). Disregarding the parallel current for the moment, we have

$$-\frac{m_i n_i}{B_\parallel}\frac{\partial\vec{E}}{\partial t}\cdot\hat{e}_r=\frac{2\left(p_i+p_e-p_{i\infty}-p_{e\infty}\right)}{R}\sin\theta\,, \tag{A14}$$

which is, the electric field rewritten in terms of the electric drift of the plasmoid particles, and neglecting the background pressure, the basic equation for the plasmoid drift acceleration:

$$m_i\frac{du_D}{dt}=\frac{2k_B\left(T_i+T_e\right)}{R}. \tag{A15}$$

APPENDIX B.

DERIVATION AND SOLUTION OF THE PARALLEL ALFVÉN CURRENT WAVE EQUATION

Using local Cartesian coordinates x, y, z (x describing the radial direction and z the direction of the magnetic field), assuming a reasonably sized magnetic shear length Ls, so that Ls dependencies like in the derivative parallel to the magnetic field,

$$\nabla_\parallel=\frac{\partial}{\partial z}+\frac{B_y}{\left|\vec{B}\right|}\frac{\partial}{\partial y}=\frac{\partial}{\partial z}+\frac{x}{L_s}\frac{\partial}{\partial y}, \tag{B.1}$$

can be neglected, and considering a source s(x,y,z,t) of electric charges that are accumulated by the curvature drift per unit volume and time, it follows from Ampère's law and the current continuity equation for ideal MHD conditions ($E_{||} = 0$, $\varepsilon \sim c^2/v^2_A$):

$$\begin{aligned} \nabla_{||} \cdot \vec{j}_{||} - s + \nabla_{\perp} \cdot \left(\varepsilon_0 \frac{c^2}{v_A^2} \frac{\partial E_{\perp}}{\partial t} \right) = 0, \\ \Delta_{||} \cdot \vec{j}_{||} - \varepsilon_0 \frac{c^2}{v_A^2} \Delta_{\perp} \nabla_{||} \frac{\partial \Phi}{\partial t} = \nabla_{||} s. \end{aligned} \tag{B.2}$$

The electric potential can be expressed by the parallel current; with the relations

$$E_{||} = -\nabla_{||} \Phi - \frac{\partial A_{||}}{\partial t} = 0, \tag{B.3}$$

$$\mu_0 \vec{j}_{||} = \left(\nabla \times \nabla \times \vec{A} \right)_{||} = \nabla_{||} \left(\nabla \cdot \vec{A} \right) - \Delta_{\perp} A_{||} - \Delta_{||} A_{||}, \tag{B.4}$$

the latter being simplified by non-consideration of magnetosonic effects, implying (introducing a poloidal scalar potential function χ)

$$\begin{aligned} B_{||} = 0 \rightarrow \vec{A}_{\perp} = \nabla_{\perp} \chi, \\ \nabla_{||} \left(\nabla \cdot \vec{A} \right) = \nabla_{||} \left(\nabla \cdot \left(\vec{A}_{||} + \nabla_{\perp} \chi \right) \right) = \Delta_{||} A_{||} + \underbrace{\nabla_{||} \Delta_{\perp} \chi}_{0}, \end{aligned} \tag{B.5}$$

which gives, replacing the parallel magnetic vector potential by the electric potential through the relation (B.3),

$$\mu_0 \vec{j}_{||} = -\Delta_{\perp} A_{||} = \Delta_{\perp} \left(\int_0^t \nabla_{||} \Phi \, dt' \right) = \Delta_{\perp} \nabla_{||} \left(\int_0^t \Phi \, dt' \right), \tag{B.6}$$

the wave equation is obtained by insertion of (B.6) into (B.2) by twofold time derivation,

$$\Delta_{||} \vec{j}_{||} - \frac{1}{v_A^2} \frac{\partial^2 \vec{j}_{||}}{\partial t^2} = \nabla_{||} s, \tag{B.7}$$

which has for charge sources with slow time evolution the special solution $\vec{j}_{||} \sim \int_0^z s \, dz'$, yielding

$$\vec{j}_{||} \sim \int_0^z s \, dz' + F(z - v_A t) + G(z + v_A t) \tag{B.8}$$

for the general solution. The wave functions F, G are determined by the initial conditions at the time t = 0, when the charge source term is applied, but the charge concentration and parallel dissipation current are still at zero level. From $\vec{j}_{||} = 0$ and momentum conservation, it follows

$$\vec{j}_{||} \sim \int_0^z s \, dz' - \frac{1}{2} \int_0^{z - v_A t} s \, dz' - \frac{1}{2} \int_0^{z + v_A t} s \, dz', \tag{B.9}$$

describing the propagation of two wave fronts at Alfvén speed in both parallel directions, leaving behind a constant parallel current comparable to that located at the plasmoid-plasma interface in the same parallel direction.

APPENDIX C.

GLOSSARY

All symbols, indices, and abbreviations used in this paper are summarised in the subsections below.

C.1. SYMBOLS.

A list of all symbols is given in table 7, including a description and corresponding units. Depending on the context, some symbols may have different meanings.

C.2. INDICES.

Indices used for the specification of various quantities as listed in Subsection C.1 can be looked up in table 8.

C.3. ABBREVIATIONS.

DEMO DEMOnstration Power Plant
ELM Edge Localised Mode
FTU Frascati Tokamak Upgrade
HFS High field side (of the magnetic field configuration)
HPI2 Hydrogen pellet injection code
ILW ITER-like wall
ITER International Thermonuclear Experimental Reactor
JET JET European Torus
JINTRAC JET INtegrated TRansport Analysis Code
JT-60 Japanese Torus
LFS Low field side (of the magnetic field configuration)
LIDAR Light Detection and Ranging (Thomson scattering measurement system)
MAST Mega Ampère Spherical Tokamak
MHD magnetohydrodynamic(s)
NGS Neutral gas shielding
NGPS Neutral gas and plasma shielding
RFP Reversed field pinch machine
VHFS Vertical high field side (for vertical inboard pellet injection)

REFERENCES

[1]. Pégourié B. 2007 Plasma Physics and Controlled Fusion **49** R87–R160
[2]. Milora S.L, Houlberg W.A, Lengyel L.L and Mertens V. 1995 Nuclear Fusion **35** 657–754

[3]. Parks P.B. and Baylor L.R. 2005 Physical Review Letters **94** 125002 (4pp)
[4]. Pégourié B, Waller V, Nehme H, Garzotti L and Géraud A 2007 Nuclear Fusion **47** 44–56
[5]. Rozhansky V, Senichenkov I, Veselova I and Schneider R 2004 Plasma Physics and Controlled Fusion **46** 575–591
[6]. Belonohy E, Kardaun O J W F, Fehér T, Gál K, Kálvin S, Kocsis G, Lackner K, Lang P.T, Neuhauser J and the ASDEX Upgrade Team 2008 Nuclear Fusion **48** 065009 (9pp)
[7]. Pégourié B, Waller V, Dumont R.J, Eriksson L-G, Garzotti L, Géraud A and Imbeaux F 2005 Plasma Physics and Controlled Fusion **47** 17–35
[8]. Matsuyama A, Pégourié B, Sakamoto R, Mishra J S, Motojima G and Yamada H 2012 Plasma Physics and Controlled Fusion **54** 035007 (15pp)
[9]. Garzotti L, Pégourié B, Géraud A, Frigione D and Bazlor L.R 1997 Nuclear Fusion **37** 1167-75
[10]. Pégourié B, Picchiottino J M, Drawin H W, Géraud A and Chatelier M 1993 Nuclear Fusion **33** 591-600
[11]. Parks P B and Turnbull R J 1978 Physics of Fluids **21** 1735–41
[12]. Leo W R 1994 Techniques for Nuclear and Particle Physics Experiments (Berlin/Heidelberg: Springer Verlag)
[13]. Houlberg W A, Attenberger S E, Baylor L R, Gadeberg M, Jernigan T C, Kupschus P, Milora S.L, Schmidt G.L, Swain D.W. and Watkins M.L. 1992 Nuclear Fusion **32** 1951–65
[14]. Baylor L R et al. 1997 Nuclear Fusion **37** 445–50
[15]. Lengyel L.L, Büchl K, Pautasso G, Ledl L, Ushakov A.A, Kalvin S, Veres G. 1999 Nuclear Fusion **39** 791
[16]. Gál K, Belonohy É, Kocsis G, Lang P.T, Veres G. and the ASDEX Upgrade Team 2008 Nuclear Fusion **48** 085005 (10pp)
[17]. Parks P.B, Sessions W.D and Baylor L.R 2000 Physics of Plasmas **7** 1968–1975
[18]. Ishizaki R, Parks P.B, Nakajima N and Okamoto M 2004 Physics of Plasmas **11** 4064–4080
[19]. Samulyak R., Lu T and Parks P 2007 Nuclear Fusion **47** 103–118
[20]. Lalousis P J, Lengyel L L and Schneider R 2008 Plasma Physics and Controlled Fusion **50** 085001
[21]. Nehme H 2009 Calcul de la source de matière effective associée à l'alimentation par injection de glaçon. Application à ITER., PhD thesis (Marseille: University of Marseille)
[22]. Waller V 2003 Modélisation de la source de matière associée à l'injection d'un glaçon dans un tokamak, PhD thesis (Marseille: Université de Provence)
[23]. Emmert G A, Wieland R M, Mense A T and Davidson J N 1980 Phys. Fluids 23 803-12
[24]. Lengyel L L, Rozhanskij V A and Veselova I Yu 1996 Nuclear Fusion 36 1679–90
[25]. Lengyel L L, 1978 Phys. Fluids 21 1945–56
[26]. Emmert G A, Wieland R M, Mense A T and Davidson J N 1980 Physics of Fluids 23 803-12
[27]. Müller H W, Dux R, Kaufmann M, Lang P T, Lorenz A, Maraschek M, Mertens V, Neuhauser

J and the ASDEX Upgrade Team 2002 Nuclear Fusion **42** 301–9
[28]. Senichenkov I, Rozhansky V and Gusakov P 2007 Proc. 34th EPS Conf. on Plasma Physics (Warsaw, Poland) vol **31**F (European Physical Society) P-4.094
[29]. Parks P.B, Sessions W.D and Baylor L.R 2000 Phys. Plasmas **7** 1968–75
[30]. Szepesi T, Kálvin S, Kocsis G, Lang P T, Senichenkov I and ASDEX Upgrade Team 2009 Journal of Nuclear Materials **390–391** 507–10
[31]. Köchl F, Frigione D, Garzotti L, Kamelander G, Parail V, Pégourié B and JET EFDA contributors 2007 Proc. 34th EPS Conf. on Plasma Physics (Warsaw, Poland) vol 31F (European Physical Society) P-1.143
[32]. Lang P T, Büchl K, Kaufmann M, Lang R S, Mertens V, Müller H W and Neuhauser J 1997 Physical Review Letters **79** 1487–90
[33]. Lang P.T. et al. 2002 Nuclear Fusion **42** 388–402
[34]. Pégourié B and Picchiottino J.M. 1996 Physics of Plasmas **3** 4594–605
[35]. Sakamoto R, Pégourié B, Clairet F, Géraud A, Gil C, Haquin S and Koechl F 2012 Cross-field dynamics of the homogenization of the pellet deposited material in Tore Supra submitted to Nucl. Fusion
[36]. Matsuyama A, Koechl F, Pégourié B, Sakamoto R, Motojima G and Yamada H 2012 Nuclear Fusion **52** 123017 (17pp)
[37]. Senichenkov I Yu, Veselova I Yu, Rozhansky V.A and Schneider R 2005 Journal of Nuclear Materials **337–339** 446–50
[38]. Spitzer L Jr 1956 Physics of Fully Ionized Gases (New York: Interscience) Chap. 5
[39]. Parks P B 2008 internal communication
[40]. Senichenkov I Yu 2007 internal communication
[41]. Pégourié B, Köchl F, Nehme H, Commaux N, Géraud A and Garzotti L 2007 Proc. 34th EPS Conf. on Plasma Physics (Warsaw, Poland) vol 31F (European Physical Society) P-4.092
[42]. Commaux N, Pégourié B, Baylor L, Köchl F, Parks P, Jernigan T, Géraud A and Nehme H 2010 Nuclear Fusion **50** 025011 (8pp)
[43]. Huba J D 2009 NRL Plasma Formulary (Washington: Naval Research Laboratory)
[44]. Rozhansky V A and Veselova I Yu 1994 Nuclear Fusion **34** 665–74
[45]. Miyamoto K 1989 Plasma Physics for Nuclear Fusion (Cambridge: Massachusetts Institute for Technology)
[46]. Artaud J F et al. 2010 Nuclear Fusion **50** 043001 (25pp)
[47]. Wiesen S et al. 2008 JINTRAC-JET modelling suite JET ITC-Report (20pp)
[48]. Köchl F, Frigione D, Garzotti L, Kamelander G, Nehme H, Pégourié B and JET EFDA contributors 2008 Proc. 35th EPS Conf. on Plasma Physics (Hersonissos, Crete, Greece) vol 32D (European Physical Society) P-4.099
[49]. Frigione D, Boboc A, Gál K, Garzotti L, Giovannozzi E, Köchl F, Kocsis G, Lang P, Pégourié B, Valovič M and EFDA-JET contributors 2009 Proc. 36th EPS Conf. on Plasma Physics

(Sofia, Bulgaria) vol 33E (European Physical Society) P-5.160
[50]. Lang P T, Alper B, Buttery R, Gál K, Hobirk J, Neuhauser J, Stamp M and JET-EFDA contributors 2007 Nuclear Fusion **47** 754–61
[51]. Kamelander G, Frigione D, Garzotti L, Köchl F, Nehme H and Pégourié B 2008 Proc. 35th EPS Conf. on Plasma Physics (Hersonissos, Crete, Greece) vol 32D (European Physical Society) P-4.104
[52]. Lang P T et al. 2012 ELM pacing and trigger investigations at JET with the new ITER Like Wall submitted to Nuclear Fusion
[53]. Yamada H et al. 2001 Plasma Physics and Controlled Fusion **43** A55–71
[54]. Lorenzini R, Garzotti L, Pégourié B, Innocente P and Martini S 2002 Plasma Physics and Controlled Fusion **44** 233–52
[55]. Lang P T et al. 2011 Nuclear Fusion **51** 033010 (16pp)
[56]. Wenninger R P, Eich T H, Huysmans G T A, Lang P T, Devaux S, Jachmich S, Köchl F and JET EFDA Contributors Plasma Phys. Control. Fusion 53 (2011) 105002 (24pp)
[57]. Hayashi N, Parail V, Koechl F, Aiba N, Takizuka T, Wiesen S, Lang P T, Oyama N and Ozeki T 2011 Nuclear Fusion **51** 103030 (8pp)
[58]. Hayashi N, Takizuka T, Aiba N, Oyama N, Ozeki T, Wiesen S and Parail V 2009 Nuclear Fusion **49** 095015 (8pp)
[59]. Frigione D et al. 2010 Proc. 23rd IAEA Fusion Energy Conference (Daejon, Republic of Korea) EXC/P4-05
[60]. Koechl F et al. 2010 Proc. 37th EPS Conf. on Plasma Physics (Dublin, Ireland) vol 34A (European Physical Society) O4.123
[61]. Garzotti L et al. 2010 Nuclear Fusion **50** 105002 (7pp)
[62]. Klaywittaphat P, Onjun T, Picha R, Poolyarat N, Pégourié B, Imbeaux F, Artaud J F and Géraud A 2011 Proc. 38th EPS Conf. on Plasma Physics (Strasbourg, France) vol 35G (European Physical Society) P4.135
[63]. Matsuyama A, Koechl F, Pégourié B, Sakamoto R, Motojima G and Yamada H 2012 Plasma Fusion Results **7** 1303006 (5pp)
[64]. Ghendrih Ph et al. 2003 Nuclear Fusion **43** 1013–22
[65]. Pégourié B, Köchl F, Nehme H and Polevoi A 2009 Plasma Phys. Control. Fusion 51 124023 (10pp)
[66]. ITER Physics Basis Editors et al. 1999 Nuclear Fusion **39** 2137–638
[67]. Maruyama S, Yang Y, Sugihara M, Pitts R, Baylor L, Li B, Li W, Combs S and Meitner S 2009 Fuelling and disruption mitigation in ITER Proc. 23rd Symposium on Fusion Engineering (San Diego, USA)
[68]. Polevoi A R and Shimada M 2001 Plasma Physics and Controlled Fusion **43** 1525–33
[69]. Parail V et al. 2009 Nuclear Fusion **49** 075030 (8pp)
[70]. Wiesen S, Belo P, Koechl F, Parail V, Corrigan G, Garzotti L, Lönnroth J, Kotov V, the EUITM

ITER Scenario Modelling group and JET-EFDA Contributors 2013 Integrated ITER scenario modelling and density evolution prospects to be submitted to Nucl. Fusion

[71]. Garzotti L et al. 2012 Nuclear Fusion **52** 013002 (12pp)

[72]. Kim H.S, Parail V, Garzotti L, Koechl F, Loarte A and Na Y.S. 2012 Proc. 39th EPS Conf. on Plasma Physics / 16th International Congress on Plasma Physics (Stockholm, Sweden) vol 36F (European Physical Society) P2.044

[73]. Parail V et al. 2013 Self-consistent simulation of plasma scenarios for ITER using a combinationof 1.5D transport codes and free boundary equilibrium codes submitted to Nuclear Fusion

	Line-integrated density increase grad. ($m^{-2}s^{-1}$)	Time-average line-int. density in equilibrium state ($m^{-2}s^{-1}$)	Avg. particle content relaxation time (s)
LFS	$5.8 \cdot 10^{19}$	$(8.96 \pm 0.53) \cdot 10^{19}$	0.65 ± 0.12
VHFS	$6.5 \cdot 10^{19}$	$(9.71 \pm 0.72) \cdot 10^{19}$	0.75 ± 0.29
HFS	6.1×10^{19}	$(9.73 \pm 0.38) \cdot 10^{19}$	0.91 ± 0.27

Table 1: Quantities related to the relative fuelling efficiency in dependence of the pellet injection direction in the JET pellet experiment Pulse No: 58337.

Plasmoid radius (cm)	τ_L / τ_e , numeric estimate	τ_L / τ_e , analytic estimate
10	~ 3500	34705
5	~ 875	8677
2.5	~ 220	2170
1.253	~ 60	54
0.5	~ 10	88

Table 2: Estimates for the relation of the current rise retardation time with and without the inductive current response taken into account, calculated numerically (4.48-50) and analytically (4.47); an electron collision time $\tau_e \sim 30\mu s$ was assumed.

Tokamak scenario	Measured drift estimate (cm)	Calculated drift (cm)
FTU LFS	~3 ± 2	4.2 ± 9.3% ± 0.6%
Tore Supra LFS	0–12	12.9 ± 5.7% ± 3.1%
Tore Supra HFS	0–8 8	.9 ± 5.7% ± 3.1%
DIII-D HFS (Pulse No: 99477)	~20	10.2 ± 5.5% ± 4.0%
JET LFS (Pulse No: 49223)	~10 ± 6	11.0 ± 3.7% ± 4.1%

Table 3: Comparison of the measured average drift displacement, determined by evaluation of the barycentres of the ablation and deposition profiles, using the same kind of measurement data and calculation methods as in [31], with simulation results for typical tokamak scenarios in terms of minor radius flux surface coordinates. The error for the simulation results scales with the measurement error and is very sensitive to the correct determination of the net pellet mass rp and injection velocity vp . Relative simulation error estimates are given for a supposed measurement error of $\Delta r_p = 0.2mm$ and $\Delta v_p = 50m/s$ resp.

	C_1	C_2	C_3	C_4	C_5	C_6	C_7	C_8	C_9	C_{10}	C_{11}	C_{12}	C_{13}	σ (m)	$\sigma_{rel.}$ (%)
Δ_1	0.116	0.120	0.368	0.041	0.015	1.665	0.439	0.217	-0.038	0.493	0.193	-0.346	-0.204	0.031	28.0
Δ_2	0.064	0.192	0.105	0.025	0.077	1.500	0.899	0.955	0.031	0.671	0.377	-0.493	-0.026	0.032	29.2
Δ_{LFS}	0.109	0.159	-0.069	0.129	0.135	0	0	0	0	0	0	0	0	0.016	9.1
Δ_{HFS}	0.079	0.054	-0.337	0.271	0.340	0	0	0	0	0	0	0	0	0.010	6.3
Δ_{VHFS}	0.064	0.147	0.289	0.159	0.118	0	0	0	0	0	0	0	0	0.012	8.6

Table 4: Scaling law constants $C_{1\text{-}13}$, standard deviation s and relative error σ_{rel}. for the calculation of the absolute pellet-averaged drift displacement in terms of r for arbitrary tokamak geometries ($a_0 < 1.4m$, $R_0 < 4m$) with (Δ_1) and without additional statistical weight (Δ_2) put on accessible pellet injection lines and target plasma configurations at European tokamaks such as FTU, Tore Supra, and JET, as well as for specific pellet injection configurations at JET (Δ_{LFS}, Δ_{HFS}, Δ_{VHFS}).

	Stellarator	RFP	Tokamak
R_0 [m]	4.1	2.35	2.6
a_0 [m]	0.68	0.9	0.85
B_0 [T]	3.0	2.3 x	2.3 3.5
Volume [m^3]	37.4	37.4	37.1
Surface [m^2]	110.1	83.5	87.2
W_{th} [MJ]	0.7	0.7	0.7

Table 5: Main parameters for the stellarator, RFP, and tokamak configurations for which the pellet deposition profiles are compared.

	Stellarator LFS	Stellarator HFS	RFP LFS	RFP HFS	Tokamak LFS	Tokamak HFS
Mean drift displacement [cm / %]	11.8 17.3%	-10.9 -16.0%	3.9 4.3%	0.3 0.3%	9.9 11.6%	-9.8 -11.6%

Table 6:Average drift displacement per pellet particle, measured as barycentre displacement between the pellet ablation and deposition profiles in terms of minor radius flux surface coordinates and in terms of % of a_0.

Symbol	Description	Unit
a	acceleration	[m/s^2]
a_0	plasma minor radius	[m]
$\vec{A}$	magnetic vector potential	[Tm]
A	effective cross-sectional area atomic mass number	[m^2]
$\vec{B}$	magnetic field	[T]
B_0	toroidal magnetic field strength at $R = R_0$	[T]
c	speed of light	2.998·10^8 m/s
C	arbitrary constant	
$C(t)$	arbitrary time-dependent function	
C_s	sound speed	[m/s]
$\varepsilon(\alpha)$	scaling factor for P_{con} for $\alpha \neq 0, \pi$	F/m
η	resistivity	[Ωm]
	poloidal plasmoid angle compared to the angle of maximum positive charge accumulation	[rad]
θ	Braginskii coefficients for viscosity poloidal angle	[rad]
	pitch angle	[rad]
$\Theta(\cdots)$	Heaviside function	
κ	collisional thermal conduction flux surface ellipticity	[m^{-1}s^{-1}]
K	effective thermal conductivity	[m^{-1}s^{-1}]
$\lambda = \ln \Lambda$	Coulomb logarithm	
λ_i	average dissociation and ionisation energy per atom	[J]
λ_p	sublimation energy of a pellet molecule	[J]
Λ	impact parameter of the pellet trajectory in terms of normalised ρ coordinates	
μ	inverse of the safety factor	
μ_0	vacuum permeability	4π·10^{-7} Wb/Am
ν	collision frequency	[Hz]
ξ	fixed parameter	
$\Xi(\cdots)$	auxiliary function	
$\widetilde{\Pi}$	geometric amplification factor for the poloidal plasmoid cross-section, yielding the interaction cross-section considering a finite Larmor radius of incident particles	
D_0	particle diffusivity inside the plasmoid	[m^2/s]
$\hat{e}$	unit vector	
$\vec{E}$	electric field	[V/m]
E	energy content	[J]
E_c	critical energy	[J]
$f(\cdots)$	arbitrary (distribution) function	
f_i	fraction of ionised particles	
$f^{MB}(\cdots)$	Maxwell-Boltzmann distribution	
$F(x-vt)$	arbitrary wave function, forward wave propagation	
$G(\vec{r},t)$	energy density at the position $\vec{r}$ at a time t	[J/m^3]
$G(x+vt)$	arbitrary wave function, backward wave propagation	
ρ	minor plasma radius flux surface coordinate	[m]
ρ_M	plasmoid barycentre in terms of ρ	[m]
σ	conductivity standard deviation	[S/m]
$\sigma(\cdots)$	stopping cross-secton	[m^2]
σ_s	characteristic quantity for the plasmoid distortion caused by the magnetic shear	
τ	collision time characteristic (exponential decay) time	[s] [s]
τ_{Alfv}	characteristic time for parallel Alfvénic current saturation	[s]
τ_{con}	time needed for the first external reconnection of oppositely charged plasmoid regions	[s]
τ_e	electron collision time	[s]
τ_L	characteristic inductive retardation time for Pégourié current formation	[s]
Φ	electric (sheath) potential	[V]
χ	diffusivity	[m^2/s]
	poloidal scalar potential for the magnetic vector potential	[Tm^2]
$X(\cdots)$	auxiliary function	
$\widetilde{\omega}$	projection of the normalised particle velocity onto the poloidal plane ($= \sin\theta$)	
Ω	gyro-frequency	[Hz]
∇	gradient	
∂	partial derivative	

Table 7: Description of symbols used in this paper.

Index	Description
A	arithmetic mean
A / *Alfv*	Alfvénic
cen	(bary)centre
con	reconnection
D	drift
DL	double layer
e	electron
eff	effective
f	fast particle
H	harmonic mean
i	ion / ionised / index number
ie	electron-ion interaction
inf	infimum
ini	initial
int	internal
L	indutance-related quantity
mag	magnetic
max	maximum
M	mass barycentre
n	pellet neutral cloud / index number for fast particle energy distribution discretisation
NGS	neutral gas shielding
p	pellet / plasmoid
ped	top of the edge transport barrier (pedestal)
pol	poloidal
proj	projected
PS	pre-sheath
rad	radial
rel	relative / release
res	resolution
Rozh	Rozhansky
s	sound
SL	single layer
Sp	Spitzer
sup	supremum
T	thermal
0	plasmoid / magnetic axis
∞	background plasma
$\parallel$	parallel to the magnetic field
$\perp$	perpendicular to the magnetic field
ζ	toroidal (direction)
Φ	external reconnection

i	integer value	
I	electric current arbitrary interval	[A]
I_{pl}	total plasma current	[A]
$\vec{j}$	current density	[A/m^2]
j_{zS}	assumption for Pégourié current density distribution without inductive response	[A/m^2]
k_B	Boltzmann constant	$1.602 \cdot 10^{-19}$ J/eV
L	cylinder length / plasmoid length self-inductance	[m] [H]
$L_{\parallel/\perp}$	parallel / perpendicular gradient length for thermal conductivities	[m]
L_a	radial plasmoid length	[m]
L_b	poloidal plasmoid length	[m]
L_{con}	average length of Pégourié current channels	[m]
L_{con2}	average length of channels of external reconnection of plasmoid charges of the same sign	[m]
$L_{J\phi}$	radial width of the external parallel current conduit	[m]
L_{n0}	gradient length for (collisional) diffusivities	[m]
L_s	magnetic shear length	[m]
L_η	gradient length for viscosities	[m]
L_ϕ	average plasmoid cloud self-connection length (rough estimate)	[m]
m	particle mass toroidal period	[kg]
M	entire mass	[kg]
M_0	plasmoid mass	[kg]
$M_{0,L_{con2}}$	mass of the plasmoid and external charged regions affected by the drift movement	[kg]
M_{eff}	effective mass in motion (parallel to the magnetic field)	[kg]
n	density poloidal period	[m^{-3}]
N	total number of particles	
p	pressure	[Pa]
$\vec{P}(z)$	position vector of the plasmoid at a distance z to the plasmoid barycentre	[m]
P_{con}	fraction of externally reconnected plasmoid charges of opposite sign	
R_n	pellet neutral cloud radius	[m]
r_p	pellet radius	[m]
R_p	plasmoid radius	[m]
s	length of an integration path source of electric charges	[m] [C/m^{3}s]
S	line-integrated path-averaged density	[m^{-2}]
$\vec{s}_D$	drift displacement	[m]
$\mathrm{sgn}(\cdots)$	Signum function	
t	time	[s]
t_{rel}	time of plasmoid detachment from the pellet	[s]
u	velocity	[m/s]
u_D	drift velocity	[m/s]
$\vec{u}_{E\times B}$	electric drift	[m/s]
$\vec{u}_{*i}$	diamagnetic drift	[m/s]
$\vec{u}_{pi}$	polarisation drift	[m/s]
v	particle velocity	[m/s]
$V(\rho)$	volume inside a flux surface labelled by ρ	[m^3]
v_A	Alfvén speed	[m/s]
V_s	average velocity at the interface between the plasmoid and the plasma	[m/s]
v_T	thermal velocity	[m/s]
W	volume-integrated internal and shear viscosity energy loss	[W]
W_{th}	plasma thermal energy content	[J]
x	ratio between the Larmor radius of a particle and the plasmoid radius radial distance (Cartesian coordinates)	 [m]
$\widetilde{X}$	geometric amplification factor, compared to parallel plasmoid extension, for the length of the trajectory of an incident particle inside the plasmoid cloud due to its finite Larmor radius	
y	poloidal distance (Cartesian coordinates)	[m]
z	vertical distance parallel to the magnetic field	[m]
Z	vertical position on the poloidal plane longitudinal (plasmoid) extension atomic charge number	[m] [m]
Z_0	plasmoid half-length in the parallel direction	[m]

P_{con2}	fraction of externally reconnected plasmoid charges of the same sign		α	pellet injection angle in the poloidal plane (LFS: $\alpha = \pi$)	[rad]
q	elementary charge	$1.602 \cdot 10^{-19}$ C	α'	angular fraction of the path of a particle inside the plasmoid domain	[rad]
	heat flux	[W/m^2]	β	correction factor as given in [18a]	
	safety factor		β_1, β_2	auxiliary terms	
$\delta q(\cdots)$	total relative charge deposition along a magnetic field line in a plasmoid		γ	correction factor as given in [18a]	
Q	energy source / sink / transfer rate	[W]		ratio of specific heats at constant pressure and volume	
	fusion Q		$\Gamma(\cdots)$	auxiliary function	
r	minor plasma radius coordinate	[m]	Δ	Laplacian	
	radial coordinate in cylinder geometry	[m]		difference operator	
r_0	position in terms of r of a flux surface with a rational safety factor m/n	[m]		small distance	[m]
$\vec{r}_c$	curvature radius	[m]	Δ_{Drift}	absolute pellet-averaged drift displacement in terms of ρ	[m]
r_c	plasmoid location in r coordinates	[m]	ε	asymmetry parameter	
R	cylinder radius	[m]		infinitesimally small quantity	
	major radius coordinate	[m]	ε_0	vacuum permittivity	$8.854 \cdot 10^{-12}$
	resistance	[Ω]			
R_0	major plasma radius	[m]			

Table 8: Description of indices used in this paper.

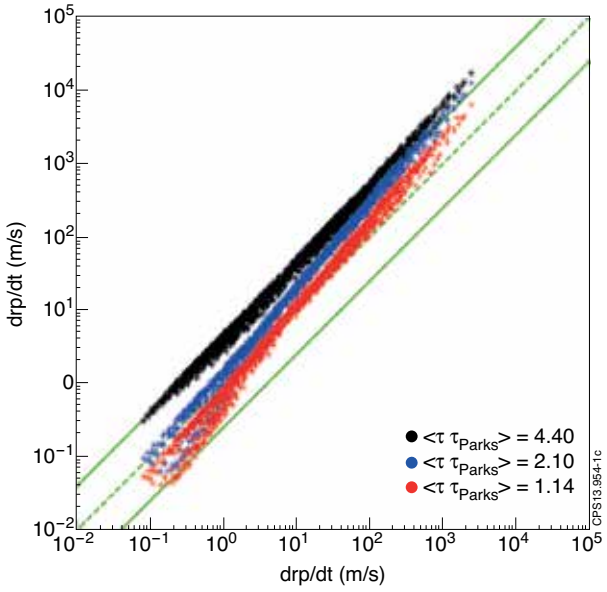

Figure 1: r_p/dt as calculated in accordance with the NGS model considering a Maxwellian distribution (black stars), the NGPS model without consideration of the electrostatic sheath (blue stars), and the complete NGPS model (red stars), as a function of the pellet radius regression speed determined by the NGS model for a mono-energetic beam.

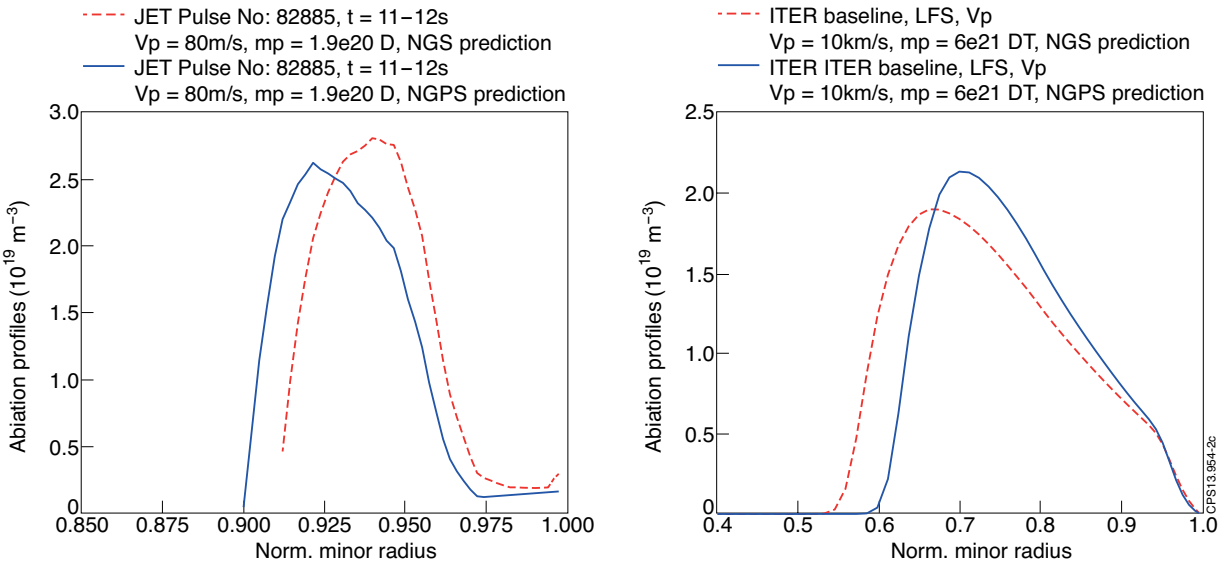

Figure 2: Pellet particle ablation profiles calculated with the HPI2 code (see Section 7 for the code description) in accordance with the NGS (red) and the NGPS models (blue) for the cases of a pellet injection from the vertical high field side (VHFS) into a JET plasma (left, Pulse No: 82885, I_{pl} = 2 MA, B_0 = 2.1 T, $T_{e,ped}$ ~ 600 eV, $n_{e,ped}$ ~ $4.5 \cdot 10^{19}$ m^{-3}, t = 11-12 s, r_p = 0.9 mm, injection velocity v_p = 80 m/s, poloidal pellet injection angle α = -73.5°), as well as from the LFS (pellet trajectory on the outer mid-plane) into an ITER baseline scenario plasma (right, I_{pl} = 15 MA, B_0 = 5.3 T, $T_{e,ped}$ ~ 4 keV, $n_{e,ped}$ ~ $9 \cdot 10^{19}$ m^{-3}, flat-top phase, r_p = 2.86 mm, v_p = 10 km/s).

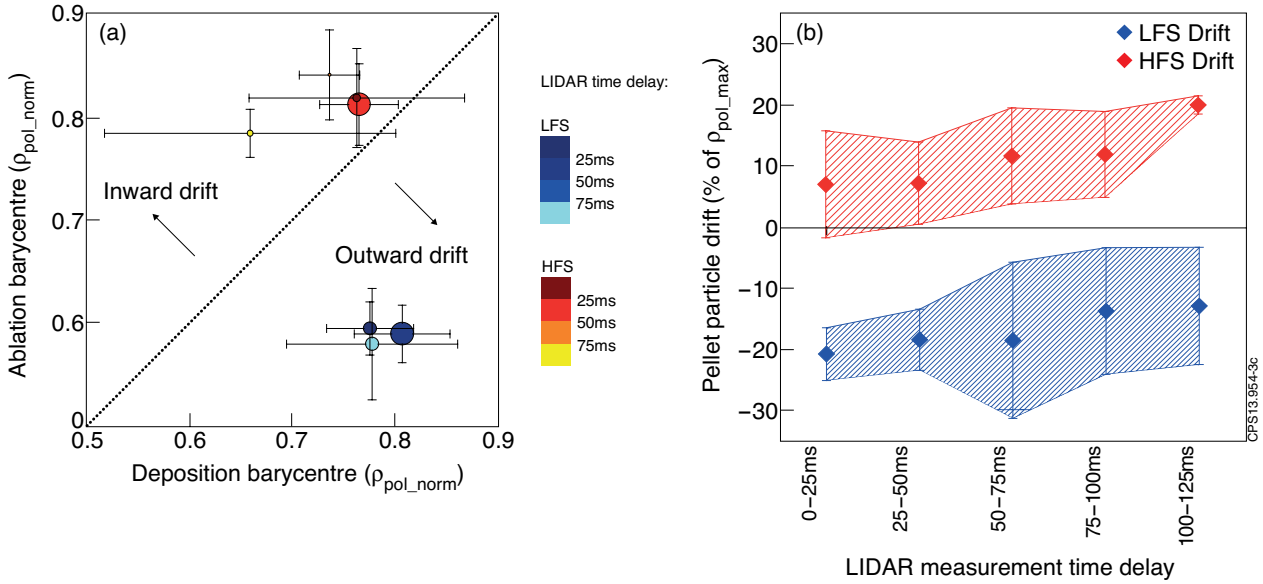

Figure 3: (a) Average barycentres for the pellet ablation and deposition profiles in the JET pellet database, plotted in dependence of the pellet injection direction and the relative timing of the LIDAR. The size of the circles corresponds to the amount of analysed data. (b) Averaged measured pellet particle drift in JET pellet experiments for LFS and HFS injections and its dependence on the LIDAR measurement delay due to intermediate particle transport (diffusion etc.).

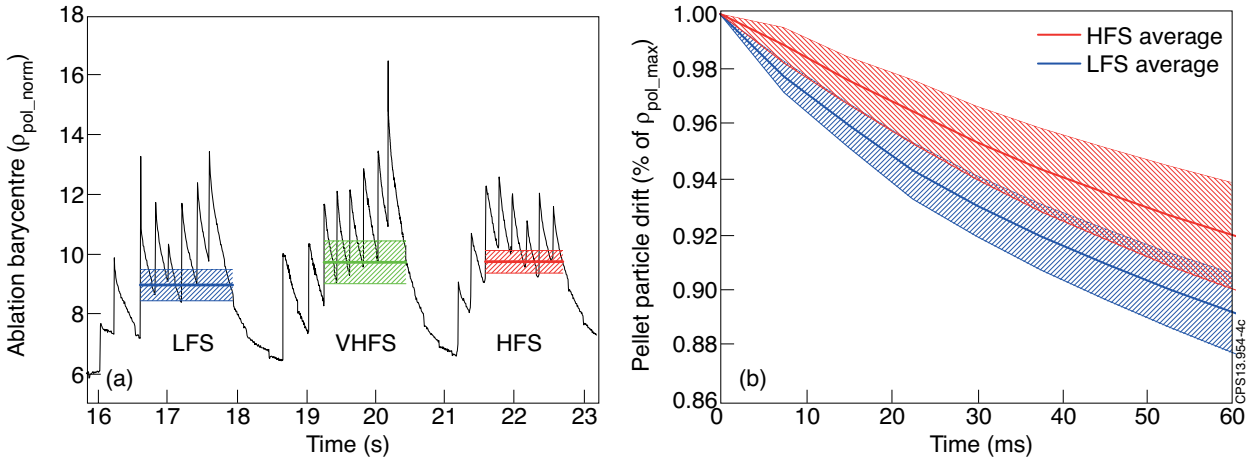

Figure 4: (a) Time evolution of a line-integrated density signal in the JET experiment Pulse No: 58337, and the density equilibrium level for each pellet injection series (blue: LFS, green: vertical HFS, red: HFS), calculated with the averaged local density minima in the equilibrated phase. (b) Averaged normalised line-integrated density decline right after a pellet injection for the LFS and HFS series in the JET experiment Pulse No: 58337. The particles seem to be better retained in the HFS case.

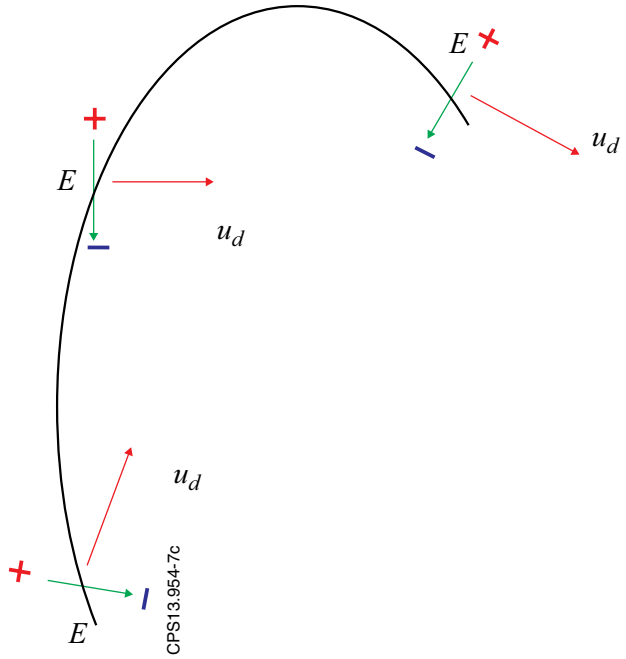

Figure 5: Schematic projection of a plasmoid onto the poloidal plane, illustrating a change in the direction of the drift velocity due to poloidal rotation of the electric field inside the plasmoid. At both ends, the deviation of u_d from the horizontal line is the most pronounced.

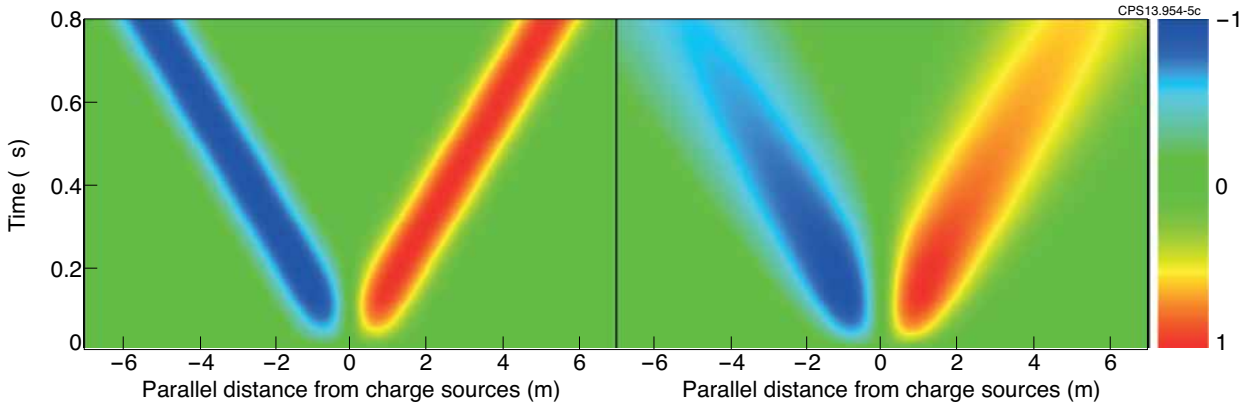

Figure 6: Longitudinal evolution of the time derivative of the parallel current (a.u.), calculated by equation (4.11), for typical hot plasma conditions; left: $\eta_{eff} = 2 \cdot 10^{-5} \Omega m$, right: $\eta_{eff} = 2 \cdot 10^{-3} \Omega m$.

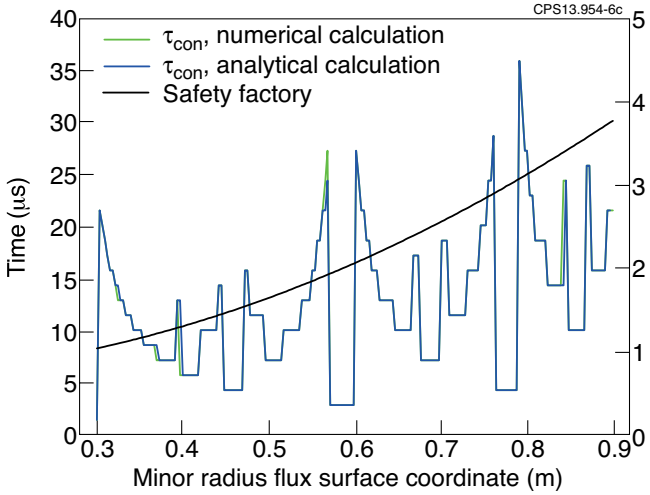

Figure 7: Time of first connection t_{con} as a function of the minor radius flux surface coordinate, calculated numerically (green) and according to (4.39) (blue), with a comparison to the q profile (black); the following parameters were used: $m_{max} = 50$, $R_p^{rad} = R_p^{pol} \sim 1cm$, $a_0 = 1m$, R_0 - 3m, $B_0 = 3T$, $n_\infty = 5 \cdot 10^{19}\ m^{-3}$, $\Delta^{pol} = 5mm$

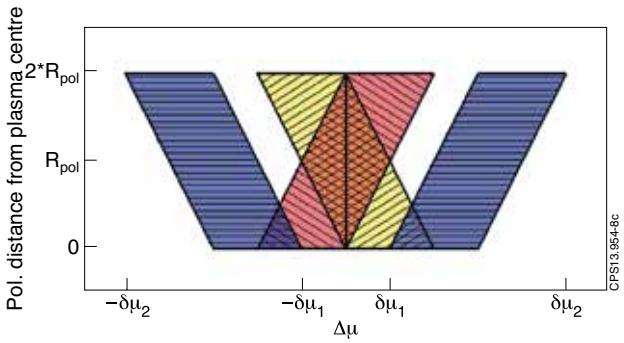

Figure 8: Indication of areas of external reconnection (blue, horizontally hatched) and selfreconnection (yellow, diagonally hatched with positive inclination: reconnection in the forward direction; red, diagonally hatched with negative inclination: reconnection in the backward direction) for the upper charged plasmoid region, in Δμ coordinates for the radial extension.

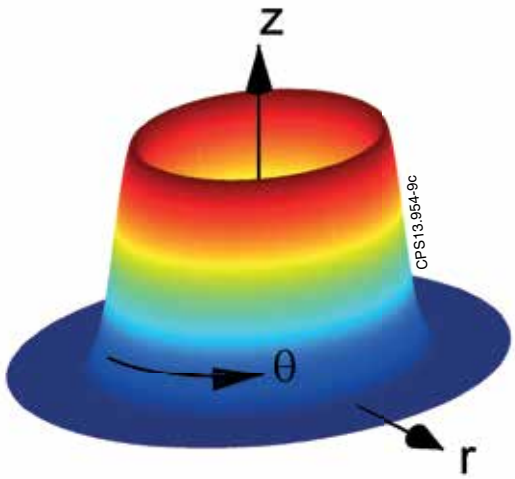

Figure 9: Cylindrical coordinate system used in numeric simulations of the field and current evolution in accordance with (4.48-49), including an illustration of a plasmoid surface current density distribution representative for j_{zS} assumptions made in this analysis.

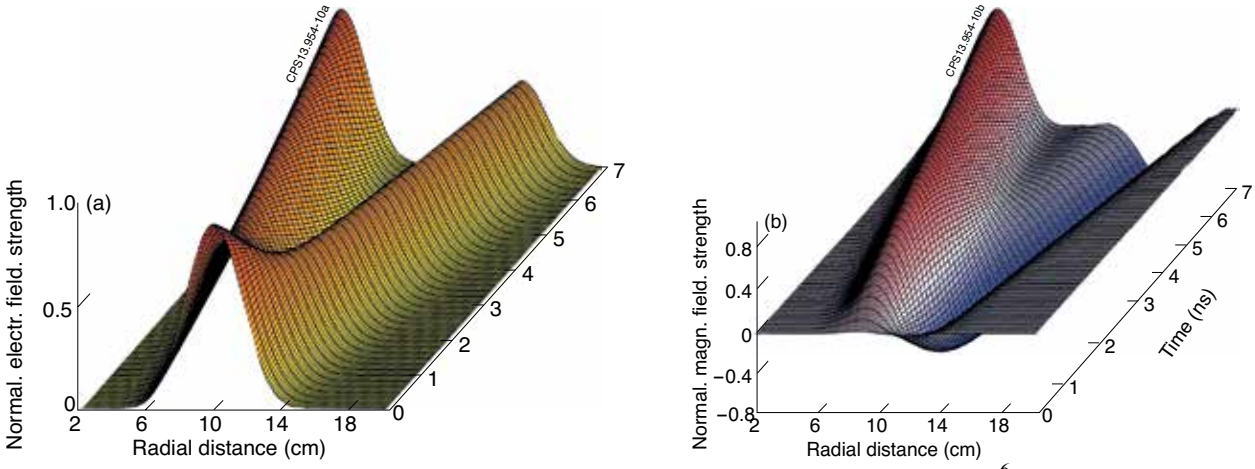

Figure 10: Evolution of an electromagnetic field perturbation according to (4.48) ($v_A \sim 7 \cdot 10^6$m/s), (a): E_z , (b): B_θ.

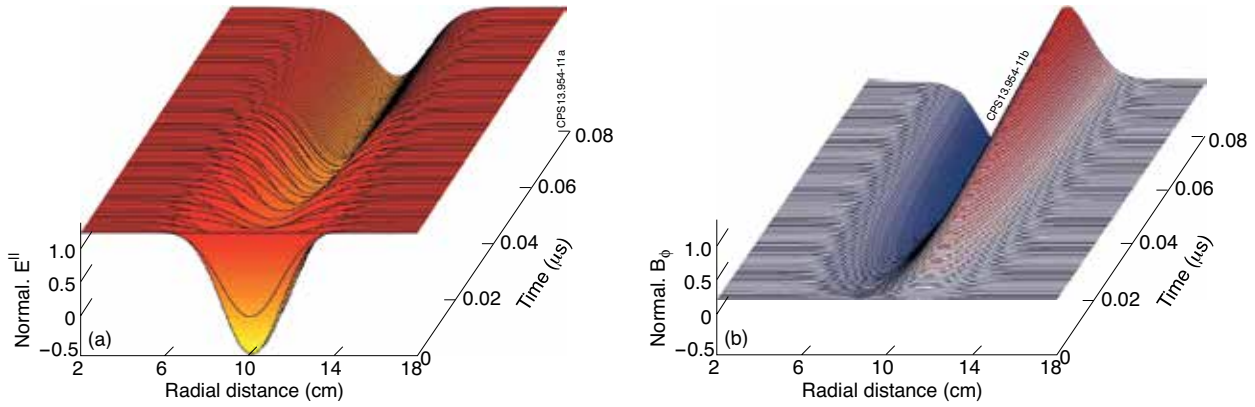

Figure 11: Evolution of the plasma reaction to a Gaussian Pégourié current distribution j_{zS} according to (4.48-49), (a): E_z , (b): B_θ .

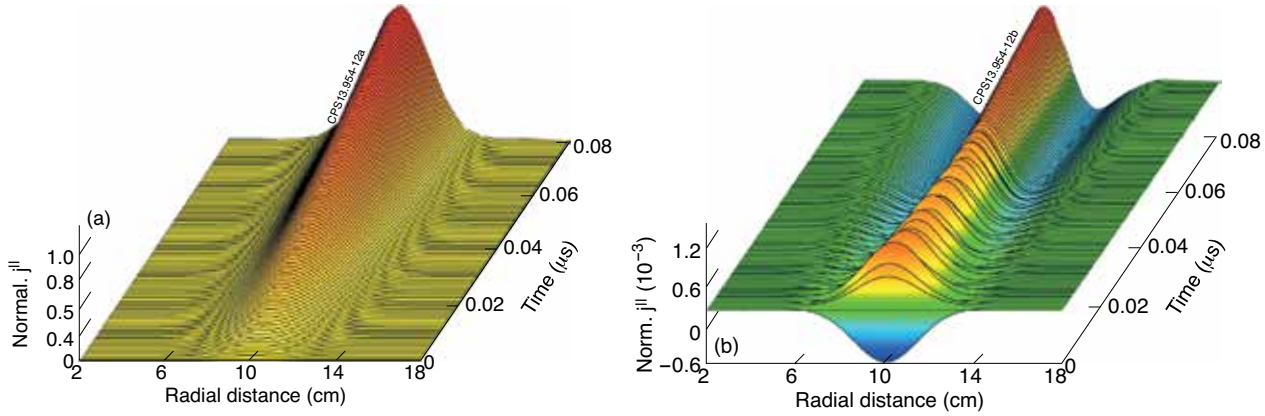

Figure 12: Evolution of the Pégourié current (a) without and (b) with consideration of the inductive counter-current formation as given in (4.48-49), normalised to the maximum of j_{zS} .

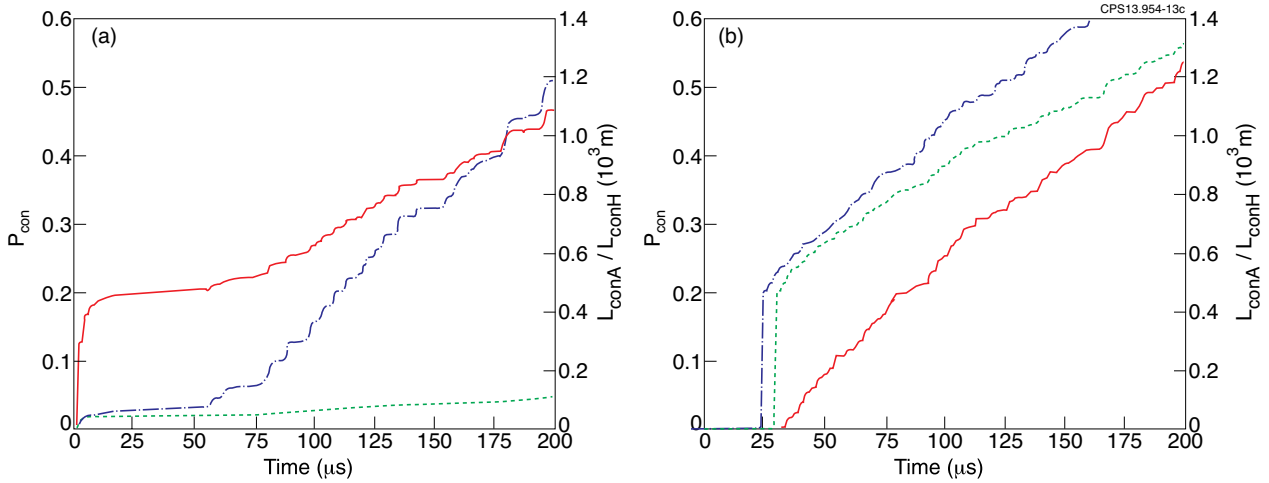

Figure 13: Time evolution of P_{con} (red, solid), L_{conH} (green, dashed) and L_{conA} (blue, dash-dotted), for plasmoids deposited (a) on the q = 2 surface and (b) close to the q = 2 surface, for the same parameter configuration as used for the calculation of t_{con} shown in figure 7. (4.55) (a) (b)

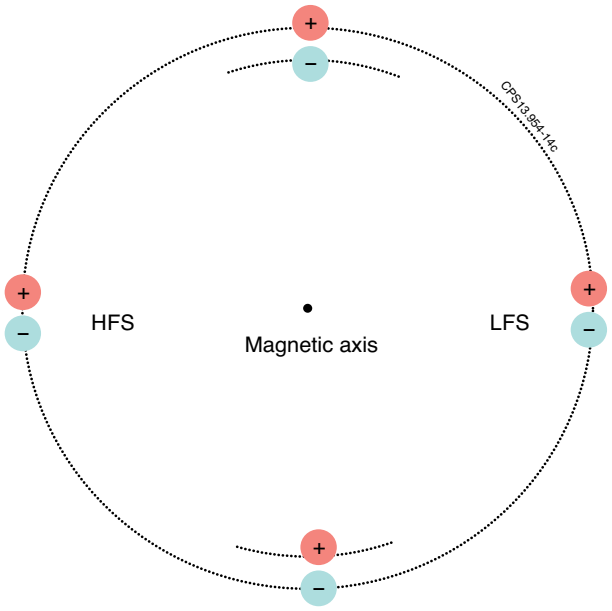

Figure 14: Positioning - in relation to the reference magnetic surface - of positively and negatively charged regions above and below the plasmoid, showing cases of plasmoid deposition on theequatorial plane or on the vertical plane passing through the magnetic axis.

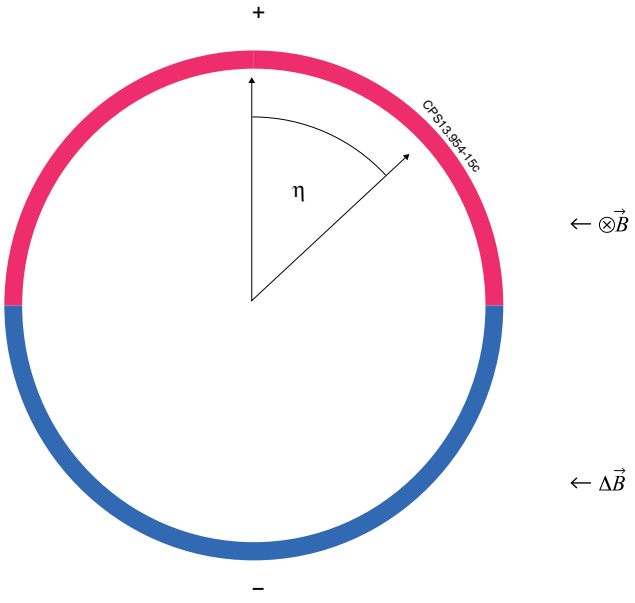

Figure 15: Charge distribution along the plasmoid surface as considered for the derivation of an α-dependent correction term for P_{con}.

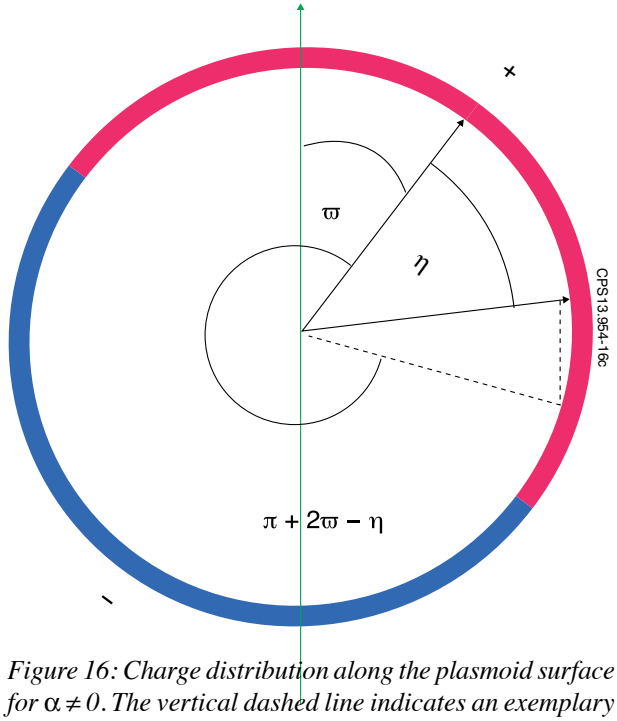

Figure 16: Charge distribution along the plasmoid surface for $\alpha \neq 0$. The vertical dashed line indicates an exemplary flux surface on which only charges of the same sign can get connected. The green arrow specifies the tangent to the flux surfaces.

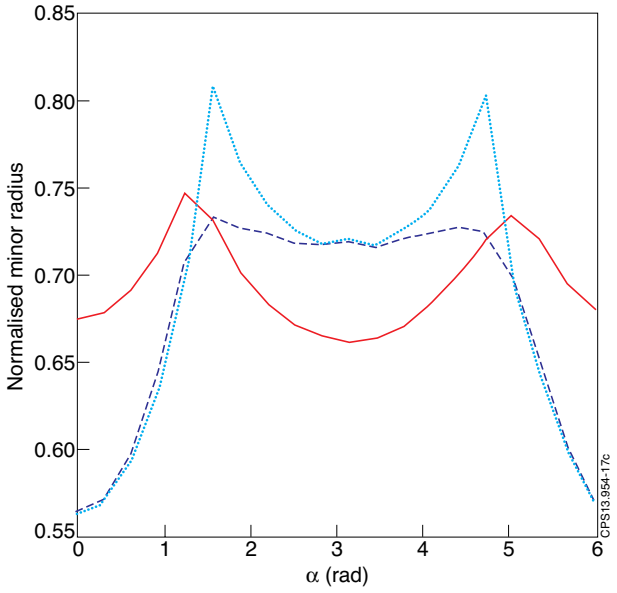

Figure 17: Barycentre of the ablation profile (red) and the deposition profiles with (cyan) and without (blue) consideration of ε(α) in the definition of P_{con} , P_{con2} in dependence of the pellet injection angle α for pellets with r_p =1.5 mm, v_p = 150 m/s and an L-mode test target plasma corresponding to the JET discharge #76411 at t = 24.53s, given in terms of normalised minor radius flux surface coordinates.

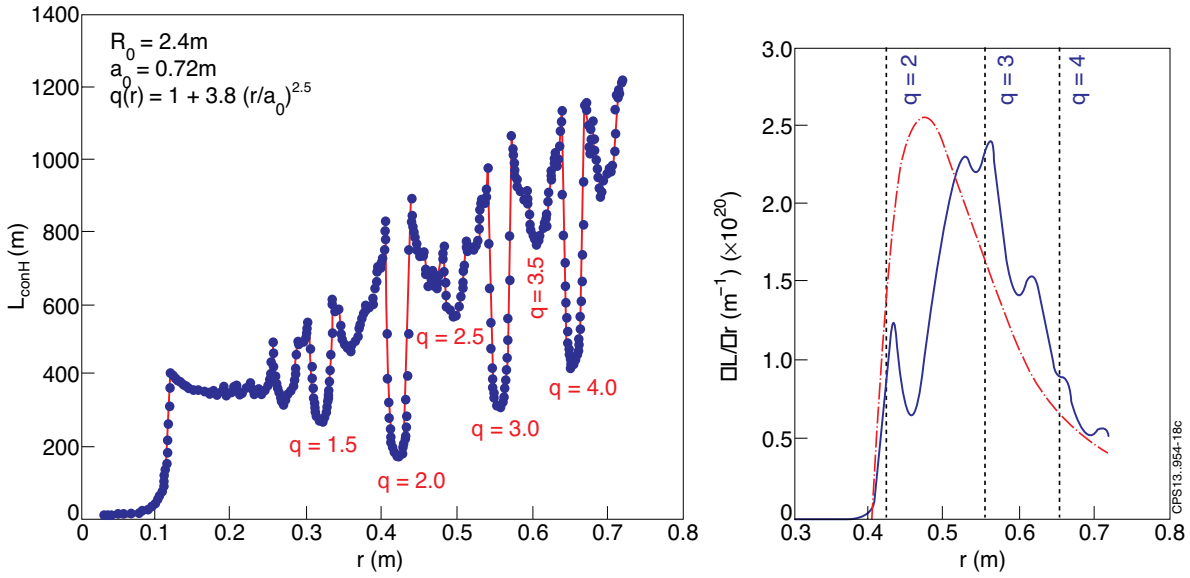

Figure 18: (a) Dependence of L_{conH} ($t = \infty$) on the minor radius flux surface coordinate for a typical q profile and tokamak geometry. (b) Pellet ablation (red) and deposition (blue) profile for an injection with a pellet radius $r_p = 0.55$mm and an injection speed $v_p = 400$ m/s from the low field side in a tokamak similar to Tore Supra, with the Pégourié drift damping effect taken into account.

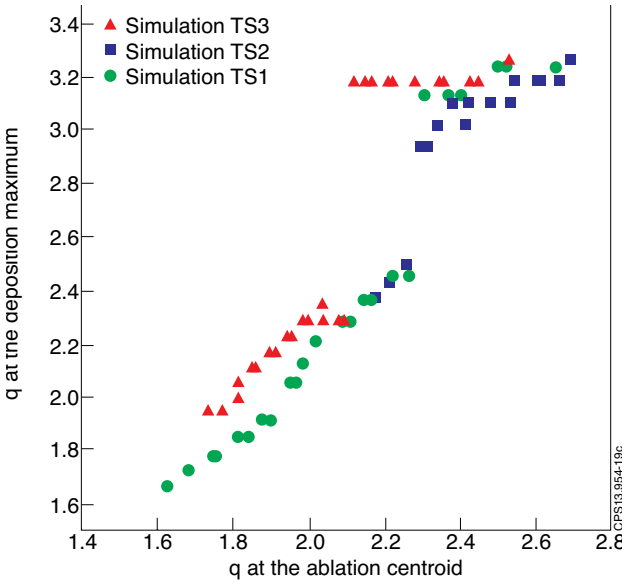

Figure 19: Maximum position of pellet deposition versus maximum-weighted centroid position of pellet ablation in terms of q; the simulation results for LFS pellet injections at varying injection conditions for three different Tore Supra target plasma assumptions (triangles: 1.3MA, squares: 1.0MA, circles: 0.6MA discharges) are compared to the experimental trend (blue shaded area). [42]

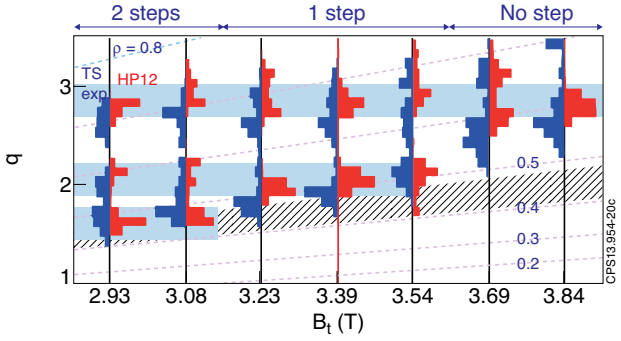

Figure 20: Histograms of the probability density of the temporary pellet particle deposition peak location in terms of q during pellet fuelling (injection from the LFS), as measured (blue) and calculated with HPI2 (red) for Tore Supra experiments at varying B_t ($= B_0$). The hatched area indicates the pellet ablation peak region ($P_{norm.} = 0.4$ - 0.5). The horizontal bands, which are located near the low-order rational q surfaces 1.5, 2.0 and 3.0, highlight positions of maximum probability density. [35]

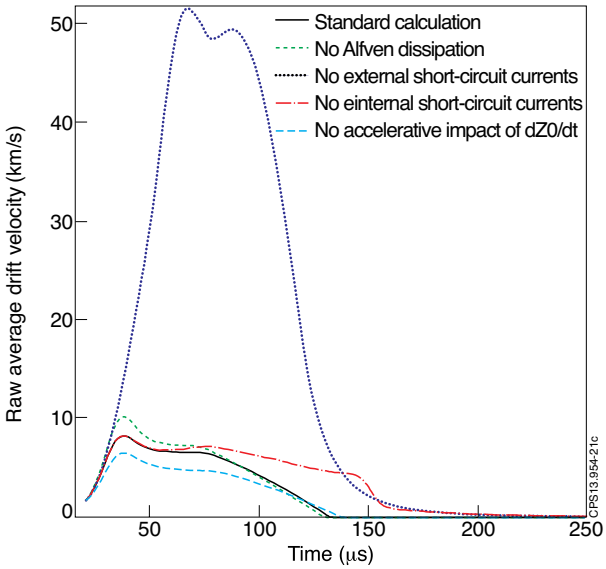

Figure 21: Average horizontal drift velocity for a plasmoid particle in an idealised high energy tokamak plasma environment, showing the effect of omitting various terms in the plasmoid drift equation.

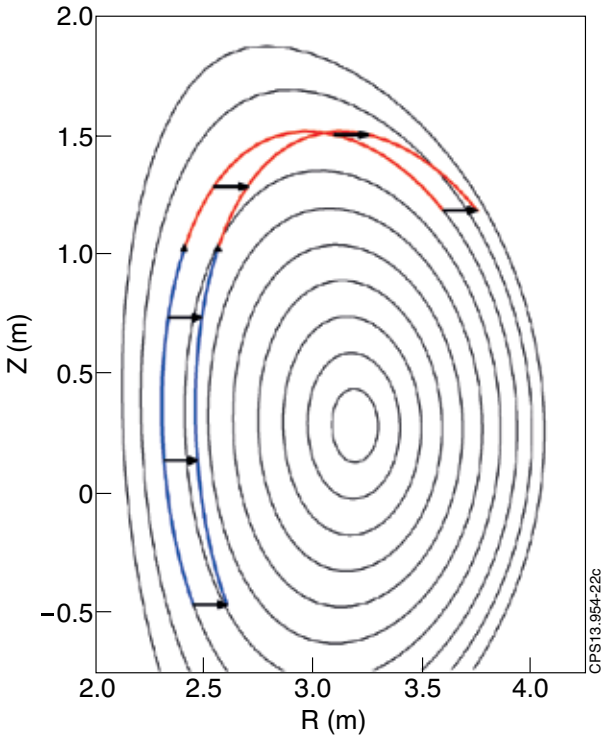

Figure 22: Upper (red) and lower half (blue) of a plasmoid deposited in the upper HFS of an arbitrary tokamak configuration projected onto the poloidal plane, with and without an $E \times B$ drift displacement of s_D =15cm.

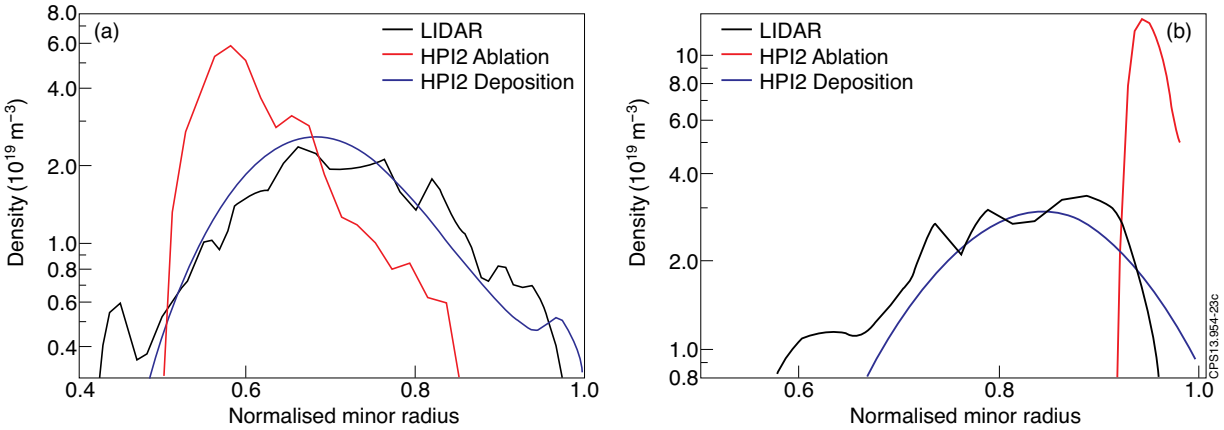

Figure 23: Ablation and deposition profiles calculated by HPI2, compared to the increase in density right after pellet injection measured by high resolution Thomson scattering diagnostics. (a): JET L-mode Pulse No: 76411, pellet injection from the LFS at t = 24.53s ; (b): JET hybrid mode Pulse No: 77864, pellet injection from the VHFS at t = 7.42s .

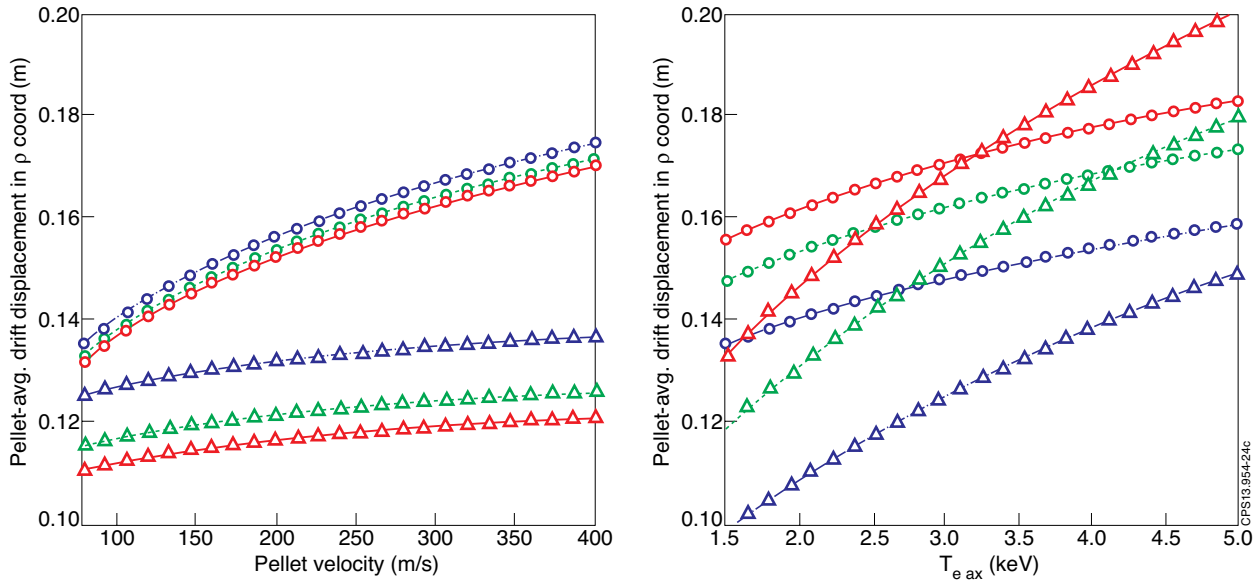

Figure 24: Pellet-averaged drift displacement in terms of ρ (a) in dependence of v_p ,for r_p = 1.8mm (blue, dash-dotted), r_p = 2.3mm (green, dashed) and r_p = 2.6 mm (red, solid), at $n_{e0} = 3\times10^{19}$ m^{-3}, T_{e0} = 3keV, (b) in dependence of T_{e0} , for $n_{e0} = 3\times10^{19}$ m^{-3} (blue, dash-dotted), $n_{e0} = 6\times10^{19}$ m^{-3} (green, dashed) and $n_{e0} = 9\times10^{19}$ m^{-3} (red, solid), at v_p = 150 m/s, r_p = 2mm, for pellet injections into a JET plasma via the LFS side (circles) and the HFS side (triangles) in accordance with (7.1) and the parameters given in table 4.

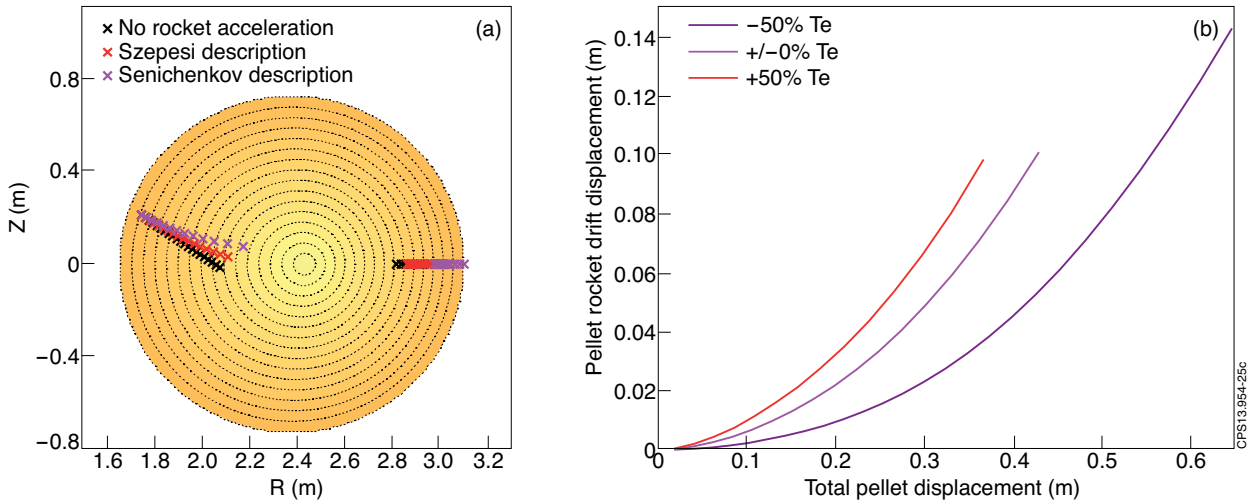

Figure 25: (a) Trajectories for HFS and LFS injections at v_p = 200m/s with pellets of the size rp =1.3mm in a Tore Supra target plasma with an axial electron density and temperature $n_0 = 4.5\times10^{19}m^{-3}$ and $T_0 \sim 4$ keVwith and without application of the pellet rocket effect (semi-empirical model: Szepesi description, theoretical model: Senichenkov description). (b) Pellet rocket drift displacement for the HFS injection case applying the semi-empirical rocket acceleration model with varying plasma temperature.

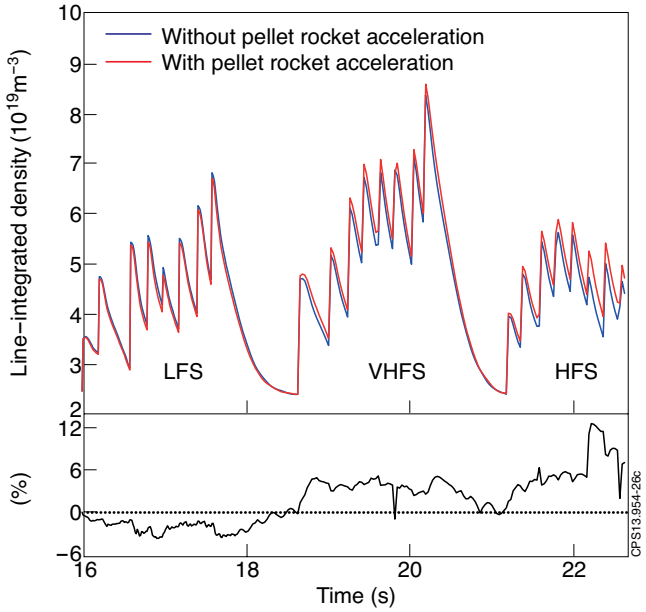

Figure 26: Transport simulation results with HPI2 for the line-integrated density evolution in JET shot #58337 with and without consideration of the pellet rocket acceleration effect (using the semiempirical model); below, the relative difference in density for the two simulation cases is given.

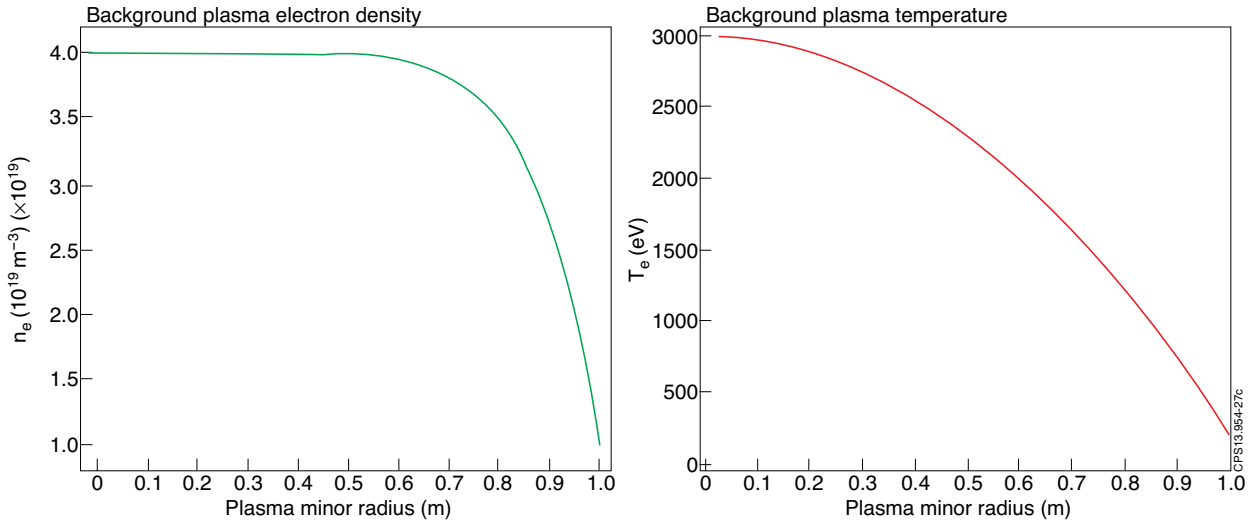

Figure 27: Background plasma density (left) and plasma temperature (right) assumed for the calculation of pellet deposition profiles for comparable conditions in a stellarator / RFP / tokamak.

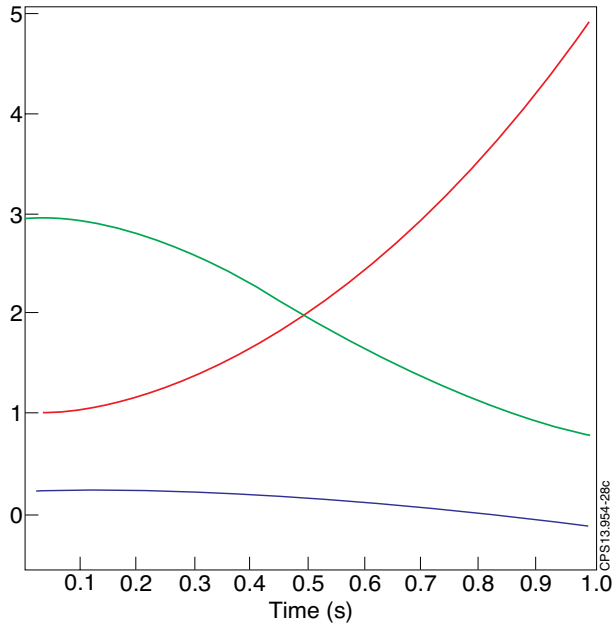

Figure 28: Safety factor for the stellarator (green), RFP (blue) and tokamak (red) configurations for which the pellet deposition profiles are compared.

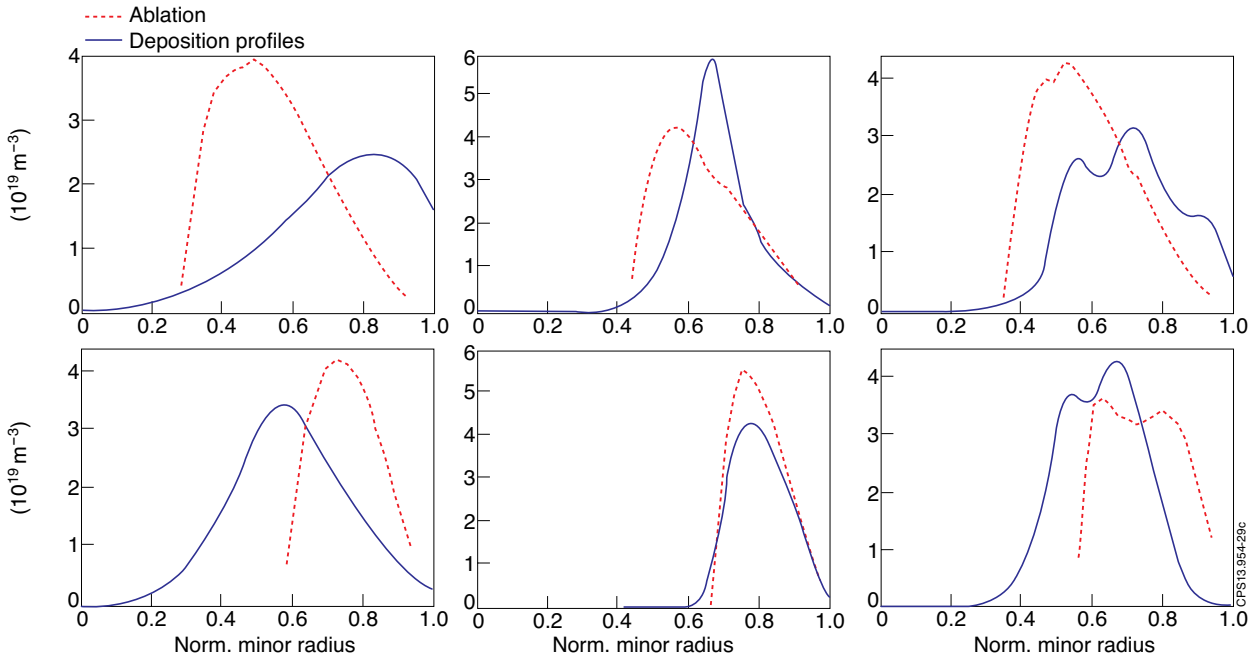

Figure 29: Ablation (red) and deposition (blue) profiles for pellets injected from the LFS (top) and the HFS (bottom), for the stellarator (left), RFP (middle) and tokamak (right) configurations.

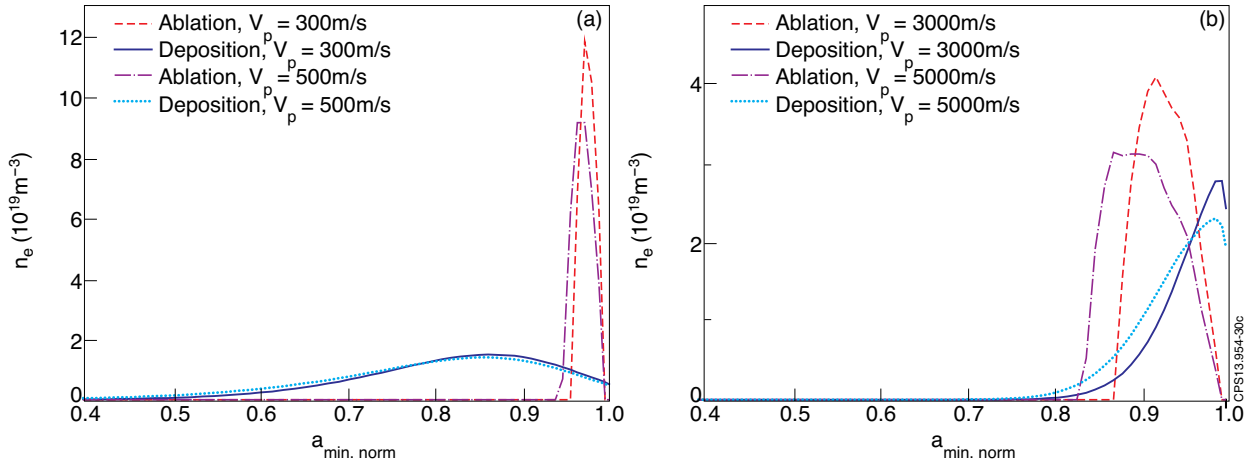

Figure 30: (a): HFS, (b): LFS injections of pellets consisting of ~ 6×10^{21} deuterium atoms into an ITER baseline scenario target plasma. The ablation and deposition profiles are shown for different v_p .

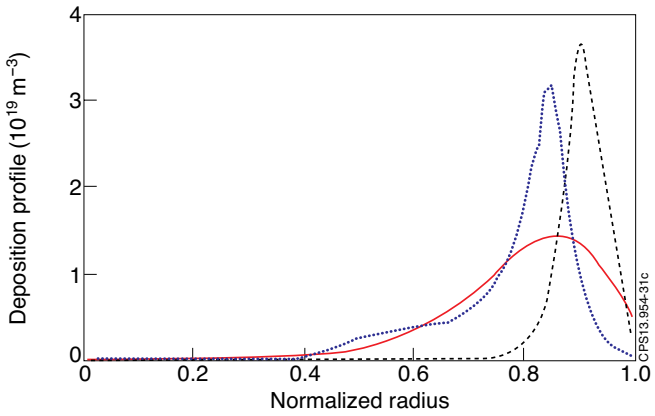

Figure 31: Pellet deposition profiles for a pellet consisting of ~ 6×10^{21} deuterium atoms, injected at v_p = 300m/s from the HFS into an ITER baseline scenario target plasma, calculated by HPI2 (red line) and the pellet codes defined in [3] (blue dotted line) and [68] (black dashed line). [65]